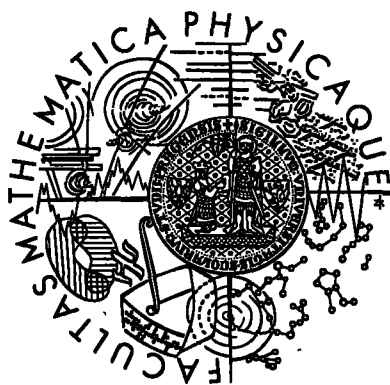


CHARLES UNIVERSITY IN PRAGUE
FACULTY OF MATHEMATICS AND PHYSICS

Dissertation



Miroslav Nožička

**Forward Silicon Tracker of the
H1 Experiment: Hardware and
Study of D^* Meson Detection**

INSTITUTE OF PARTICLE AND NUCLEAR PHYSICS

Supervisor: Doc. Ing. Josef Žáček, DrSc.
Study programme: Subnuclear Physics

Contents

Introduction	vii
1 Interaction of $e^\pm p$ at HERA	1
1.1 Deep Inelastic Scattering	1
1.2 Photoproduction	4
1.3 Factorisation and Evolution Equations	4
1.4 Heavy Quark Production Processes	6
1.4.1 Boson–Gluon Fusion	7
1.4.2 Fragmentation	8
1.5 D^* Production Cross Section	10
2 HERA and H1 Detector	13
2.1 HERA Accelerator	13
2.2 H1 Detector	14
2.2.1 Tracker	15
2.2.2 Calorimetry	19
2.2.3 Muon System	21
2.2.4 Luminosity Measurement	21
2.2.5 Trigger System and DAQ	22
3 Forward Silicon Tracker Layout, Hardware and Data Acquisition	25
3.1 Silicon Detector Principles	25
3.1.1 Semiconductors and their Properties	26
3.1.2 Semiconductor Detectors	27

3.2	FST Layout	28
3.2.1	Active Part	29
3.2.2	Front-End Electronics	33
3.2.3	Cooling	34
3.3	Electronics	34
3.3.1	Hybrid	34
3.3.2	Repeater and Subrepeater	35
3.3.3	Detector Supply	36
3.3.4	Clock Signals	36
3.4	Slow Control	37
3.5	DAQ	39
3.5.1	Event Building	40
4	FST Response	47
4.1	Reconstruction	47
4.1.1	Online Hit Reconstruction	47
4.1.2	Cluster Reconstruction	50
4.1.3	Tracking	51
4.1.4	Distribution of Track Parameters	56
4.2	Detector Response	59
4.2.1	Signal to Noise	60
4.2.2	Hit Resolution	62
4.3	Occupancy	64
4.3.1	Strip Occupancy	64
4.3.2	Module Occupancy	66
4.3.3	Pipeline Counter Occupancy	67
4.3.4	FST Internal Efficiency	70
4.4	Momentum Resolution	71
4.4.1	Theta Resolution	71
4.4.2	Transverse Momentum Resolution	72
5	D^* Reconstruction with the FST	75
5.1	D^* Meson Properties	76
5.2	D^* Monte Carlo	76
5.2.1	D^* Signal Determination	77
5.2.2	Estimation of the FST D^* Acceptance	77
5.2.3	Selections, Efficiencies and Purities Study	78
5.2.4	D^* Selection	89

5.3	Data Analysis	90
5.3.1	Luminosity	92
5.3.2	Event Selection	93
5.3.3	Trigger Conditions	95
5.3.4	<i>D*</i> Data Analysis	95
A	APC128 and Decoder Readout Chips	103
A.1	Decoder	103
A.2	APC128	104
A.3	Readout Sequence	106
B	Slow Control Modules	109
B.1	MacVEE Bus	109
B.2	Converter Card Module	109
B.3	BBL3 Signals	111
B.3.1	IP-Unidig	112
B.3.2	Mac Watchdog	112
B.4	Status Link	113
C	RIO2 8062 and FADC PMC Board for the FST	117
C.1	RIO2 Setting	117
C.1.1	Processor Setting	117
C.1.2	VME Slave Setting	118
C.1.3	VME Master Setting	118
C.2	Memory Map	119
C.2.1	Communication Area Format	120
C.2.2	Data Blocks	123
C.2.3	Hit Data	124
C.3	PMC	124
C.3.1	Memory Map	124

Introduction

In recent years the silicon strip detectors have become an important tool in high energy physics experiments. Their outstanding position resolution is used for precise particle track reconstruction and primary interaction vertex as well as secondary vertices determination. One of the primary fields of application is physics of heavy quarks where the secondary vertex of the decaying heavy flavour particle can be determined by means of the precise point measurement.

Modern collider experiments consist of several subdetectors for dedicated tasks e.g. tracking, calorimetry, or muon detectors. The detectors are usually arranged in cylindrical symmetry around the beam line covering the region around the interaction point almost hermetically. In this environment the silicon detectors are the innermost devices surrounded by tracking chambers. The standard method to use the silicon strip detector as complementary tracker is to improve the track measurements of the outer tracking chambers. For this purpose, hits (tracks) from the silicon strip detector have to be assigned (linked) to tracks measured by the surrounding detectors. As a consequence the accuracy of the primary and secondary vertices is improved considerably.

Presently the silicon strip detectors commonly provide two or three-dimensional position information which can be achieved by employing the detectors with silicon strips extending into different directions. This leads to a large number of the readout strips, typically of the order of 10^4 – 10^6 . On the other hand the detector system has to be very compact, since the amount of the non-active material close to the interaction point has to be minimised. Therefore, highly integrated readout systems are needed.

The subject of this thesis is the Forward Silicon Tracker (FST), a silicon strip detector that was installed in 2001 as a part of the upgrade program of the H1 detector installed at HERA in DESY. The layout of the detector, readout system, data acquisition and event reconstruction are described. The detector response has been studied for the data taken in 2004. The detection of the D^* mesons by means of the FST was examined for Monte Carlo simulation. An attempt to detect D^* in the data taken in 2004 was made.

The thesis is structured as follows:

The physical processes that are observed at HERA are briefly discussed in the first chapter focusing on the production of heavy quarks.

Chapter 2 introduces shortly the HERA collider and the H1 experiment after the upgrade in 2001.

The FST is described in detail in chapter 3. The layout of the FST and the front end electronics is presented. The system for controlling the detector (slow control) and the data acquisition with the aspects of event building are explained.

The hit finding and track reconstruction is outlined in chapter 4. Furthermore the detector response, occupancy and the reconstruction precision are shown there.

In chapter 5 an explorative study of the detection of D^* meson by means of the FST is made. The influence of the kinematic restriction on the purity and efficiency of the signal is studied in Monte Carlo simulation.

The final chapter gives a summary of the results and discusses possible future developments of the reconstruction.

Last but not least 3 appendixes serve as an expert description of the system.

Chapter 1

Interaction of $e^\pm p$ at HERA

The proton–electron scattering has been investigated in H1 Experiment at HERA accelerator at DESY–Hamburg since 1992. The electrons (resp. positrons) collide with protons at the CMS energy of about 320 GeV. From their interactions many secondary particles can emerge. Their production processes, which are mainly driven by the strong interaction, give the possibility to test the Quantum Chromodynamics (QCD) theory.

1.1 Deep Inelastic Scattering

The lepton–proton scattering depicted on fig. 1.1 can proceed via two processes depending on the intermediate particle:

Neutral current (NC) process which is mediated by γ or Z boson exchange. The type and charge of the lepton in the final state does not differ from the primary lepton.

Charge current (CC) process where W^\pm is exchanged and the charged primary lepton changes to the corresponding neutrino.

The CC cross section is negligible with respect to the NC cross section because of W^\pm mass. The CC process is not the subject of this thesis and it will not be further mentioned.

The following Lorentz invariant variables can be defined using four momenta of the initial proton P and the primary lepton k and scattered lepton

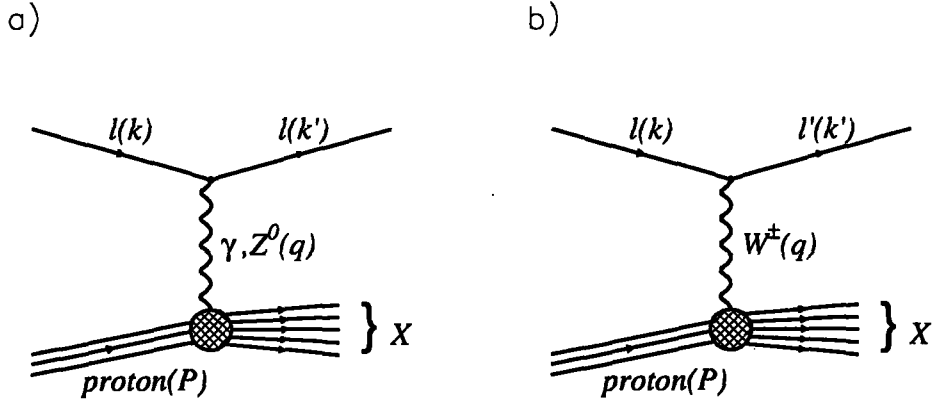


Figure 1.1: The Feynman diagram of the lepton proton interaction. The letter X denotes any final hadronic state, l, l' denote the leptons.

k' .

$$s = (k + P)^2 \doteq 4E_e E_P \quad (1.1)$$

$$Q^2 = -q^2 = -(k - k')^2 \doteq 4E_e E'_e \cos^2(\theta/2) \quad (1.2)$$

$$y = \frac{q \cdot P}{k \cdot P} \doteq 1 - \frac{E'_e}{E_e} \sin^2(\theta/2) \quad (1.3)$$

$$x = -\frac{q^2}{2q \cdot P} \quad (1.4)$$

$$W^2 = (q + P)^2 \doteq \frac{Q^2(1-x)}{x} + M_p^2 \quad (1.5)$$

where E_e (E'_e) means the energy of the initial (final) lepton, E_P is the energy of the incoming proton, M_P is the proton mass and θ is the polar angle of the scattered lepton. Variable \sqrt{s} is the total energy of colliding particles in the center of mass system (CMS), Q^2 is the negative square of the momentum transferred to the intermediate particle. The variable x denotes the fraction of the proton momentum which carries the interacting parton inside the proton. The inelasticity y expresses the relative loss of the lepton energy in the proton rest system. The variable W is the invariant mass of the hadronic system X . We talk about the “deep” inelastic scattering if

the masses of the initial particles are negligible with respect to Q^2 or qP . In this case the following relation holds

$$Q^2 = s \cdot x \cdot y \quad (1.6)$$

The quantities Q^2 , y , x can be calculated using either measured polar angle and the energy of the scattered leptons only or combining them with the measurement of the hadronic system.

Due to the large mass of the Z boson its contribution to the neutral current differential cross section is negligible and the cross section can be obtained using Quantum Electrodynamics,

$$\frac{d^2\sigma}{dx dQ^2} = \frac{4\pi\alpha}{xQ^4} [xy^2 F_1(x, Q^2) + (1-y)F_2(x, Q^2)]. \quad (1.7)$$

Here α denotes the electromagnetic coupling constant. The structure functions $F_1(x, Q^2)$ and $F_2(x, Q^2)$ parametrise the interaction of the exchanged photon with the primary proton. Introducing the longitudinal structure function

$$F_L = F_2 - 2xF_1, \quad (1.8)$$

the equation 1.7 may be rewritten as follows

$$\frac{d^2\sigma}{dx dQ^2} = \frac{2\pi\alpha}{xQ^4} [(1 + (1-y)^2) F_2(x, Q^2) - y^2 F_L(x, Q^2)]. \quad (1.9)$$

The F_L contribution is kinematically suppressed compared to F_2 . In the naive quark parton model the structure function F_2 can be expressed as

$$F_2(x, Q^2) = x \sum_i e_i^2 f_i(x), \quad (1.10)$$

where the sum runs over all quark and antiquark flavours i , e_i denotes the quark electric charge in units of elementary charge. The quark and antiquark distribution functions $f_i(x)$ denote probabilities that a quark (antiquark) i carries the momentum fraction x of the initial proton momentum.

1.2 Photoproduction

The interactions where the $Q^2 \approx 0$, i.e. the exchanged virtual photon is almost real, are called photoproduction processes. The electron is scattered under small angle and can be seen as a source of real photons. Photoproduction process dominates over DIS process since the cross section is proportional to $1/Q^4$.

The total photoproduction cross section $\sigma_{\gamma,p}$ can be derived from the differential electron–proton cross section. Neglecting the contribution of longitudinally polarised photon and introducing the flux of the transversally polarised photons

$$f_{\gamma/e}(y, Q^2) = \frac{\alpha}{2\pi y Q^2} \left[1 + (1-y)^2 - 2 \frac{m_e^2 y^2}{Q^2} \right], \quad (1.11)$$

the differential ep cross section can be rewritten in the form

$$\frac{d^2\sigma}{dydQ^2} = f_{\gamma/e}(y, Q^2) \sigma_{\gamma,p}(y, Q^2). \quad (1.12)$$

There are two processes contributing to the proton–photon cross section. Direct process where the pointlike photon interacts with the parton from the proton and resolved process where the photon splits into partons.

1.3 Factorisation and Evolution Equations

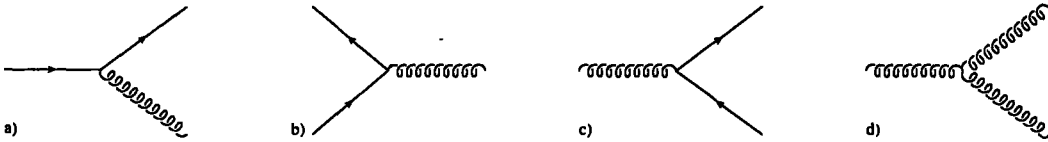


Figure 1.2: Quark and gluon radiation and splittings.

In the naive quark parton model the structure function F_2 does not depend on Q^2 . In Quantum Chromodynamics (QCD) quarks radiate gluons and gluons themselves can radiate further gluons or split into quark–antiquark pairs (see Fig. 1.2). The calculations of these radiations and splittings in

perturbative QCD (pQCD) encounter difficulties related to the divergent integrals.

The ultraviolet divergences arising from virtual loop corrections can be absorbed into the running of the strong coupling constant $\alpha_s(\mu_r^2)$ dependent on the renormalization scale $\mu_r \gg \Lambda_{QCD}$. In the lowest order $\alpha_s(\mu_r^2)$ is given

$$\alpha_s(\mu_r^2) = \frac{12\pi}{(33 - 2n_f) \log(Q^2/\Lambda_{QCD}^2)}, \quad \mu_r = Q^2, \quad (1.13)$$

where $\Lambda_{QCD} \approx 200$ MeV is an experimentally determined parameter and n_f denotes the number of the quark flavours considered in virtual loop corrections. For $\mu_r \gg \Lambda_{QCD}$ the coupling constant α_s is reasonably small and the interaction is asymptotically free, whereas at the scale $\mu_r = \Lambda_{QCD}$ the coupling constant diverges.

The infrared divergence related to the collinear gluon radiation is solved by introducing the cut-off scale μ_f , the factorisation scale, to absorb the divergences in parton density functions (PDF) $f_i(x, \mu_f^2)$. If μ_f is large enough, $\mu_f \gg \Lambda_{QCD}$, reliable QCD calculations are possible.

The introduction of factorisation and renormalization scales leads to a factorisation of the cross section. Schematically the total cross section for a production of the specific hadron h can be written as a convolution of PDFs, hard partonic cross-section $\hat{\sigma}_i$ and fragmentation function D^h ,

$$\sigma(ep \rightarrow hX) = \sum_i \sum_k f_i(x, \mu_f^2) \otimes \hat{\sigma}_{i\gamma \rightarrow kX}(\alpha_s(\mu_r^2), \mu_f) \otimes D_k^h. \quad (1.14)$$

Here the index i runs over all partons entering the hard subprocess and k runs over all partons emerging from hard subprocess. Once the PDFs and fragmentation functions are known at some starting scale μ_0 , they can be extended to a different scale by the QCD evolution equations. The evolution equations are derived considering possible gluon radiation and gluon splitting processes which can lead e.g. to a gluon ladder (see Fig. 1.3).

For the determination of PDFs there exist several approaches of summing the contributions from all ladder type diagrams. They are based on different assumptions concerning the ordering of fractional longitudinal momenta x_i , transverse momenta $k_{t,i}$ which are related to the virtualities k_i^2 and the radiation angles θ_i of radiated partons.

DGLAP In this approach [1] the gluon follows strong ordering in transverse momenta $k_{t,i}^2 \gg k_{t,i-1}^2 \gg k_{t,i-2}^2 \gg \dots$ while there is only soft ordering in

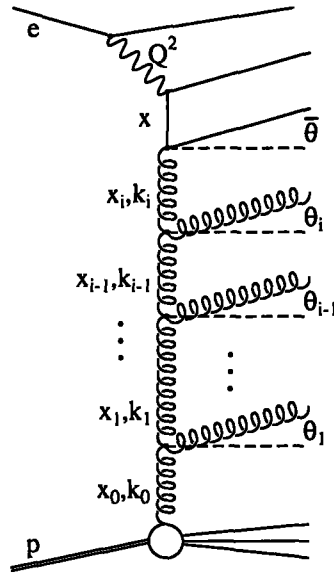


Figure 1.3: Gluon emission in the parton evolution scheme.

fractional momenta $x_i^2 < x_{i-1}^2 < x_{i-2}^2 < \dots$. The longitudinal momenta $x_i P$ are supposed to be larger than transverse momenta in this scheme which is valid for not too small x and large Q^2 .

BFKL The more appropriate regime for very low x and moderate Q^2 is BFKL [2]. In contrast to the DGLAP formalism the strong ordering in fractional momenta $x_i^2 \ll x_{i-1}^2 \ll x_{i-2}^2 \ll \dots$ of partons in ladder is used. The transfer momenta k_i^2 are not ordered.

CCFM The parton evolution according to CCFM [3] is an attempt to unify the treatment for both small and large x . The emission of gluons is only allowed in the angular ordered region of phase space. At small x the CCFM evolution is equivalent to BFKL and at large x to DGLAP evolution.

1.4 Heavy Quark Production Processes

The production of heavy quarks in ep -scattering is depicted in the figure 1.4. The direct processes are either boson-gluon fusion or coupling of the virtual

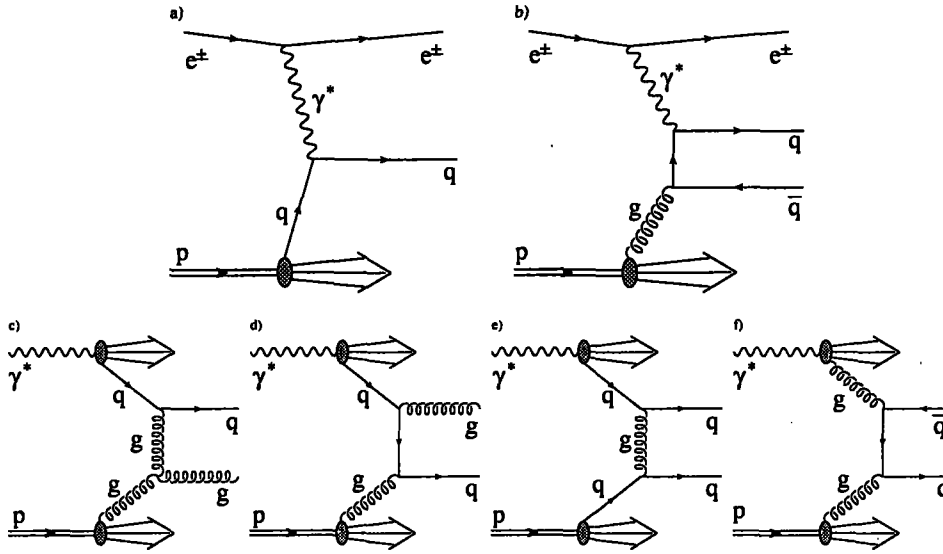


Figure 1.4: The Feynman diagram of the heavy quark production processes in $e^\pm p$ collision. a)–b) Direct photon processes. c)–f) Resolved photon processes.

photon to a sea quark coming from the proton. The heavy quarks (c, b, t) content in proton is very small with respect to the light quarks (u, d, s). In the resolved process the virtual photon fluctuates to the partons before entering the hard interaction so the structure of the virtual photon has to be taken into account.

1.4.1 Boson–Gluon Fusion

The dominant process of the heavy quark production in $e^\pm p$ interaction is the boson–gluon fusion which is depicted in Fig. 1.4 b). The emitted gluon splits into the pair of $Q\bar{Q}$ and the virtual photon interacts directly with one of the quarks. The photon–proton cross section can be expressed using factorised assumptions [4]

$$\sigma_{\gamma p}^{PGF} = \int dx_g g(x_g, \mu_f) \sigma_{\gamma g}(\hat{s}, m_q, \mu_f, \mu_R), \quad (1.15)$$

where $\sigma_{\gamma g}$ is photon–gluon cross section and g is the gluon density. These quantities depend on the proton momentum fraction x_g carried by the gluon,

on the center of mass energy \hat{s} of the heavy quark–antiquark pair, on the quark mass m_q and additionally on the renormalization and factorisation scales μ_f and μ_R .

Since the cross section depends on the gluon density in the proton its measurement provides a means of the direct determination of the gluon density. At high photon–proton center of mass energies W a large fraction of the cross section originates from resolved processes (see Fig. 1.4 c)–f)) where the structure of the virtual photon must be taken into account [4].

1.4.2 Fragmentation

The heavy quarks are revealed by identifying their fragmented hadrons. The production can be divided into production of the quarkonium bound state, e.g. J/Ψ meson, and open quark production, e.g. D^* meson. The transition from a coloured parton i to a colourless observable hadron h is described by a fragmentation function $D_i^h(z, \mu_f)$ which depends on the fraction

$$z = \frac{(E + p_l)_{hadron}}{(E + p_l)_{parton}}, \quad (1.16)$$

where p_l are the *hadron* resp. *parton* longitudinal momenta in the parton direction and E are the energies. The fragmentation function $D_i^h(z, \mu_f)$ dependence on the factorisation scale μ_f is in a sense arbitrary. It depends on advancement stage of the quark evolution absorbed into the perturbative cross section and how much of it is assigned to the fragmentation itself. Thus the fragmentation function can be expressed as a convolution of perturbative and non-perturbative parts $D_{p,i}$ and $D_{np,i}^h$

$$D_i^h(z, \mu_f) = D_{p,i}(\mu_f) \otimes D_{np,i}^h = \int_0^1 \int_0^1 dx dy D_{p,i}(\mu_f, x) D_{np,i}^h(y) \delta(xy - z). \quad (1.17)$$

The perturbative part takes into account further final state emissions. The non-perturbative $D_{np,i}^h$ describes the formation of hadron h . It is considered to be universal in terms of independence of the scale or the type of the parton production process.

Whereas light–quark fragmentation into mesons is characterised by the $z^{-1}(1 - z)^2$ behaviour a different shape is expected for the fragmentation of heavy quarks. This follows from the simple kinematical considerations which were first pointed out by Bjorken and Suzuki [5]. Attaching a light antiquark \bar{q} to heavy Quark Q decelerates the heavy quark only slightly. Thus Q and

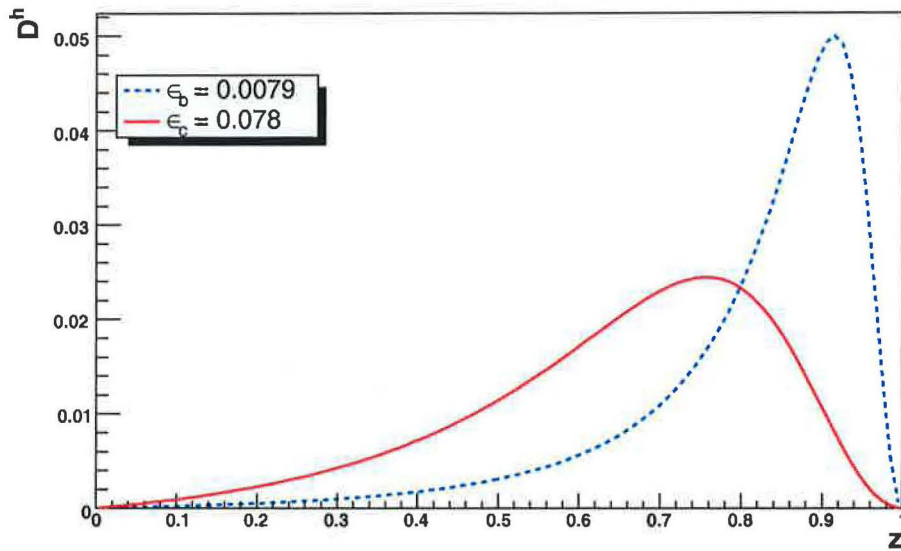


Figure 1.5: Peterson fragmentation functions D_c^h and D_b^h

the hadron should carry almost the same energy resulting in fragmentation function peak close to $z = 1$.

Various attempts has been made to describe the fragmentation function behaviour described above. The frequently used is the Peterson fragmentation [6]:

$$D_{np,i}(z) = D_Q^h(z) = \frac{N}{z[1 - 1/z - \epsilon_Q/(1 - z)]^2}, \quad (1.18)$$

where N is the normalisation factor. The parameter ϵ_Q is proportional to the fraction of light and heavy quark masses as m_q^2/m_Q^2 . Since m_q is not well defined, the parameter ϵ_Q can be treated as free and adjusted to fit the data. The model gives a fairly good prediction for the ratio $\epsilon_b/\epsilon_c \approx 0.1$. The dependence of the fragmentation functions for c and b quark is shown in Fig. 1.5.

1.5 D^* Production Cross Section

The processes which involve production of heavy quarks offer the possibility to test QCD within the perturbative scope as the heavy quark mass provides the essential hard scale in addition to the already involved one (e.g. Q^2). However the pQCD was developed for hard processes depending on one hard scale only. There exist two standard schemes which try to reduce the two-scale problem into an effective one-scale problem.

In the **massive** scheme only three active flavours (u, d, s) and the gluon are assumed to be in proton. The scheme is called massive because the charm quark is treated as massive. It is assumed that the charm mass is of the same order as the second hard scale.

In the **massless** scheme the charm quark is treated as massless like the light flavours. It appears as the fourth active flavour in the incoming proton parton density functions and it can initiate hard scattering. This approach is reliable only if the second hard scale involved is much large than the heavy quark mass.

The HVDQDIS program [11] can be used for NLO calculations of the charm cross section. It is based on the massive scheme with the renormalization and factorisation scales chosen to be equal $\mu_f = \mu_R = \sqrt{Q^2 + 4m_c^2}$, the charm mass $m_c = 1.5 \text{ GeV}$ and the proton distribution functions CTEQ5F3 [12] are used. The predictions of the charm quark production in ep interaction at HERA shows the decrease of the differential cross section $d\sigma/d\eta$ at the higher absolute pseudorapidity values of the charm quark (see Fig. 5. [11]). The D^* cross section calculation is determined using the Peterson fragmentation of the charm quark for different values of the parameter ϵ_c with the common used kinematic region for detection of D^* meson at HERA $2 \leq Q^2 \leq 100 \text{ GeV}^2$, $0.05 \leq y \leq 0.7$ (see Fig. 8. [11]).

The D^* cross section measured by the H1 and Zeus experiments [7, 10] agrees with the theoretical results of the HVQDIS program [11]. The inclusive cross section for $D^{*\pm}$ meson production measured by the H1 experiment in the visible kinematic range of $1 \leq Q^2 \leq 100 \text{ GeV}^2$, $0.05 \leq y \leq 0.7$, $p_t(D^{*+}) \geq 2.5 \text{ GeV}$ and $|\eta(D^{*+})| < 1.5$ is found to be

$$\sigma_{vis}(e^+p \rightarrow e^+D^{*\pm}X) = 8.50 \pm 0.42(\text{stat.})_{-0.76}^{+1.02}(\text{syst.}) \pm 0.65(\text{model}) \text{ nb.}$$

The rather high cross section was determined only by the detection of the D^* meson in the central region of the H1 experiment. On the other hand the

estimated value of the D^* production cross section at $1.5 < \eta < 2.5$ is about 0.4 nb (see Fig. 8. [11]).

Chapter 2

HERA and H1 Detector

In this chapter the H1 experiment at HERA accelerator is briefly outlined. The description of the experiment represents the status of the H1 subdetectors and the accelerator after the luminosity upgrade in 2001. More details can be found in [13], [14], [15].

2.1 HERA Accelerator

The HERA collider is a hadron–electron accelerator facility situated in DESY Hamburg. There are four interaction zones placed along the circumference of 6336 m. They house two fixed target experiments, HERMES at the lepton beam and HERA–B at the proton beam and two colliding experiments H1 and ZEUS.

The energies of the lepton (e^+ or e^-) and proton beams are 27.55 and 920 GeV, respectively. The beam injection into HERA is done in steps involving several preaccelerators (see Fig. 2.1). The transversal dimension of the lepton and proton beams in the vertical direction are $30\ \mu\text{m}$ and in the horizontal direction about $112\ \mu\text{m}$. The bunches lengths are 20 cm for the proton and 10 mm for the lepton beams. The accelerator has been designed to reach nominal luminosity of $4.7 \cdot 10^{31}\ \text{cm}^{-2} \cdot \text{s}^{-1}$ at the proton and lepton beam currents of 102 mA 50 mA respectively.

In order to increase the luminosity, superconducting focusing magnets GO, GG has been installed during HERA upgrade in 2001. Circular beam pipe within the H1 region had to be modified to elliptical shape in order to avoid the background induced by the synchrotron radiation. The synchrotron

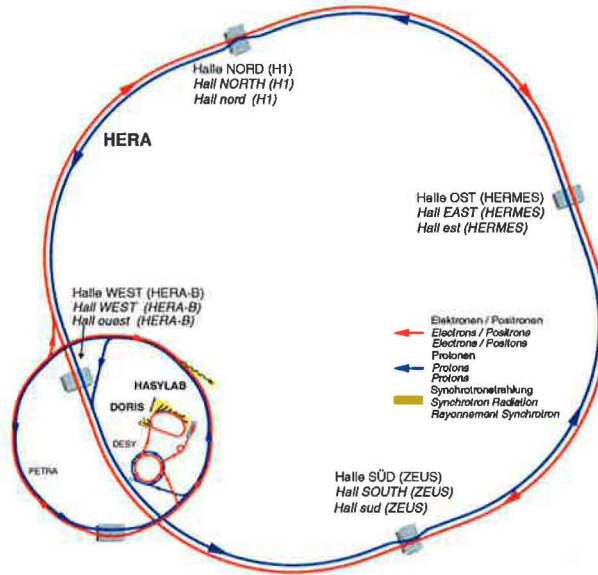


Figure 2.1: The HERA accelerator with the system of preaccelerators and with interaction zones.

radiation escapes in the larger axes of the ellipse.

2.2 H1 Detector

The H1 detector was built in 1992 and undergo several upgrades, the last one in 2000–2001. Since the energy of leptons is lower than the energy of protons the most of secondary particles move in the proton direction. The longitudinal cut of the H1 detection system in the plane parallel to the z -axis¹ is shown in Fig. 2.2.

The centre of reference system is situated in the nominal interaction vertex² with the positive z -axis in the direction of the proton beam. The H1 detector has three main parts: The central region which is situated around the nominal vertex. The backward region in the $-z$ direction and the forward region in the $+z$ direction. Each part consists of a number of subdetectors

¹This plane will be further referred as (r, z) plane.

²Interaction vertex after HERA 2000 upgrade is not at $(x, y) = (0, 0)$ of the H1 coordinate system.

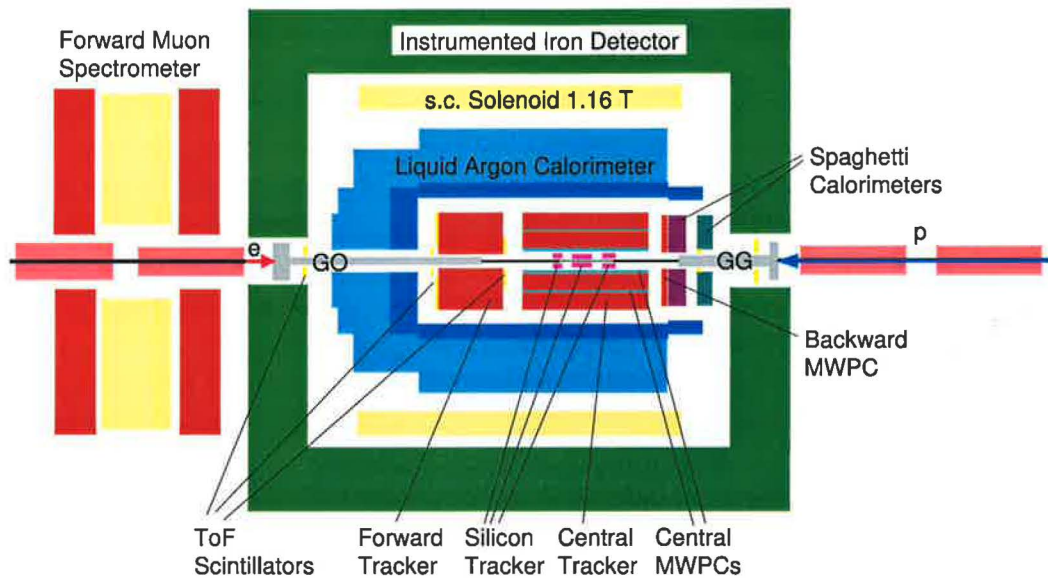


Figure 2.2: Schematic layout of the H1 detector.

which ensure the tracking, energy measurement and the detection of muons. The main detectors are complemented with a luminosity system which serves mainly for online and absolute luminosity measurement. Every event is validated by a system of triggers.

All detectors except the muon system are surrounded by the superconducting coil producing magnetic field of 1.16 T parallel with the collider tube.

2.2.1 Tracker

The H1 tracking system provides the track reconstruction and particle identification of each triggered event. It is also included in many H1 triggers [14]. The whole tracking system covers the polar angular region of $7^\circ < \theta < 173^\circ$. The angular and transverse momentum resolutions of charged particles are dependent on individual subdetectors and are on average $\Delta\theta \approx 1 \text{ mrad}$ and $\Delta p_t/p_t^2 \approx 3 \times 10^{-3} \text{ GeV}^{-1}$, respectively.

The tracking system is separated into the central and forward part. The trackers are mechanically distinct to ensure the optimisation of the tracking and triggering in their angular regions.

Central Tracker Detector

The Central Tracker Detector (CTD) consists of the Central Jet Chambers (CJC1, CJC2), Central Inner Proportional chamber (CIP), Central Outer z-chamber (COZ), Central Outer Proportional chamber (COP), Backward Proportional chamber (BPC) and Central Silicon Tracker (CST).

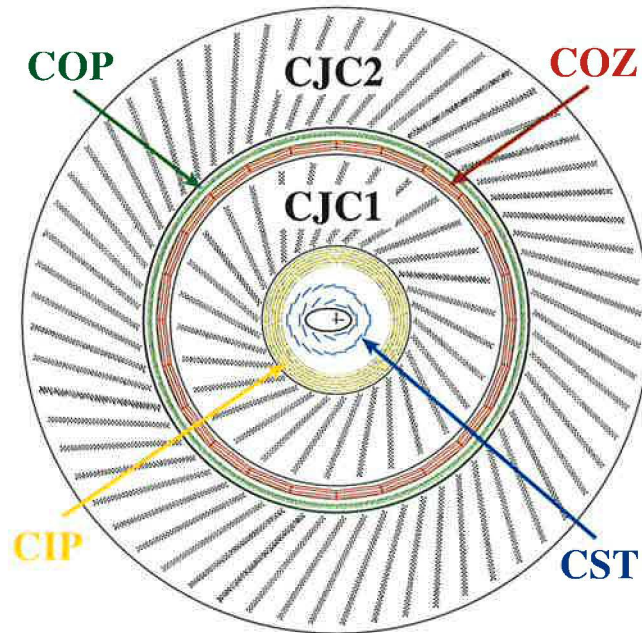


Figure 2.3: Transverse cut of the Central Tracking Detector.

CJC

The Central jet chamber is the main device of the H1 tracking system. It is separated in two concentric parts: the inner CJC1 which consists of 30 jet cells closer to the beam line and the outer CJC2 with 60 jet cells. Every jet cell contains anode wire plane with 24 respectively 32 sense wires parallel to the beam line and two adjacent cathode planes forming the drift field. The jet cells are tilted by about 30° (see Fig. 2.3) in order to ionisation electrons travel perpendicularly to the track direction.

Adjacent sense wires are separated by two potential wires to reduce the surface field and cross-talk. Additionally it allows to adjust the drift field and gas amplification independently. The potential wires connected to the ground are staggered of the nominal sense wire plane by $150 \mu\text{m}$. The sense

wires connected to the positive voltage are AC coupled to the amplifiers on both ends to ensure the measurement of the z -coordinate via the charge division.

Both chambers spread in the z -coordinate from -112.5 cm to 107.5 cm. The CJC1 and CJC2 volume are limited by inner radii of 21.8 cm and 54.5 cm, resp. and outer radii 42.6 cm and 82.3 cm, respectively. Nominal gas mixture of the chambers is 50% Argon, 50% Ethane and 0.8% Ethanol.

The CJC spatial resolution is $170 \mu\text{m}$. Since resolution in z -coordinate is very poor the measurement has to be complemented by other H1 tracking chambers. Additionally the CJC provides the particle identification by means of dE/dx measurement (for protons with the precision of 10%).

COZ

The COZ was built to complement the measurement of the tracks in the central region because of rather imprecise z -coordinate measurement of the CJC. It has a cylindrical shape with the active length of 2160 mm limited by the inner and outer radii of 920 mm and 970 mm respectively covering the polar angle range $25^\circ < \theta < 125^\circ$. It is divided into 24 identical rings each 9 cm wide and subdivided in the azimuthal angle (ϕ) into 24 drift cells. Each ring has 4 anode sense wires and 3 pairs of grounded potential wires strung perpendicular to the beam line on the ring circumference. Each cell is closed by the cathode with holes in to ensure the gas flow through the chamber. Additionally there is a capton foil with the copper field forming strips glued on remaining chamber walls. The sense wires are not staggered since mirror tracks could be removed by the software. The chamber resolution is about $300 \mu\text{m}$ in z -coordinate.

CST

The main purpose of the Central Silicon Tracker [16] is to accomplish the track measurement with few precise points to ensure very accurate vertex measurement. It consists of two layers of silicon sensor placed close to the beam line. CST shape copies the elliptical beam pipe geometry (see Fig. 2.3). The layers are built of 32 sensor ladders each consisting of 6 sensors. Three sensors bonded together form a half ladder. The readout electronics is placed at both ends of the ladder. Two neighbouring ladders form a family, share the supply voltages and are read out together sequentially.

The sensors of the CST are double sided silicon strip sensors with p -type strips parallel to the z axis and n -type strips perpendicular to the z axis implanted on the high resistivity n -type bulk. The strips are DC coupled to metal strip which is bonded to the APC128 chip with charge sensitive

wires connected to the positive voltage are AC coupled to the amplifiers on both ends to ensure the measurement of the z -coordinate via the charge division.

Both chambers spread in the z -coordinate from -112.5 cm to 107.5 cm. The CJC1 and CJC2 volume are limited by inner radii of 21.8 cm and 54.5 cm, resp. and outer radii 42.6 cm and 82.3 cm, respectively. Nominal gas mixture of the chambers is 50% Argon, 50% Ethane and 0.8% Ethanol.

The CJC spatial resolution is $170\ \mu\text{m}$. Since resolution in z -coordinate is very poor the measurement has to be complemented by other H1 tracking chambers. Additionally the CJC provides the particle identification by means of dE/dx measurement (for protons with the precision of 10%).

COZ

The COZ was built to complement the measurement of the tracks in the central region because of rather imprecise z -coordinate measurement of the CJC. It has a cylindrical shape with the active length of 2160 mm limited by the inner and outer radii of 920 mm and 970 mm respectively covering the polar angle range $25^\circ < \theta < 125^\circ$. It is divided into 24 identical rings each 9 cm wide and subdivided in the azimuthal angle (ϕ) into 24 drift cells. Each ring has 4 anode sense wires and 3 pairs of grounded potential wires strung perpendicular to the beam line on the ring circumference. Each cell is closed by the cathode with holes in to ensure the gas flow through the chamber. Additionally there is a capton foil with the copper field forming strips glued on remaining chamber walls. The sense wires are not staggered since mirror tracks could be removed by the software. The chamber resolution is about $300\ \mu\text{m}$ in z -coordinate.

CST

The main purpose of the Central Silicon Tracker [16] is to accomplish the track measurement with few precise points to ensure very accurate vertex measurement. It consists of two layers of silicon sensor placed close to the beam line. CST shape copies the elliptical beam pipe geometry (see Fig. 2.3). The layers are built of 32 sensor ladders each consisting of 6 sensors. Three sensors bonded together form a half ladder. The readout electronics is placed at both ends of the ladder. Two neighbouring ladders form a family, share the supply voltages and are read out together sequentially.

The sensors of the CST are double sided silicon strip sensors with p -type strips parallel to the z axis and n -type strips perpendicular to the z axis implanted on the high resistivity n -type bulk. The strips are DC coupled to metal strip which is bonded to the APC128 chip with charge sensitive

preamplifiers (The readout chip is described in details in appendix A.).

CIP and COP

The central proportional chamber are complementary tracking chambers but mainly used for the interaction vertex triggering.

The CIP chamber has been upgraded within HERA 2000 upgrade. It is a concentric multiwire proportional chamber situated between the CST and CJC1 (see Fig. 2.3) and ranges from $z = -1127$ mm to $z = +1043$ mm covering the polar angular region of $11^\circ < \theta < 169^\circ$. The CIP consists of 5 layers which have 480 anode wires of diameter $25 \mu\text{m}$ strung parallel to the beam line. Cathode planes situated 6 mm apart from the wires are made of capton coated with carbon. Capton pads directly connected to the readout electronics are placed on carbon layers. The pads are arranged in the special so called projective geometry (For details see [17]). The CIP is mainly used for trigger level 1 which selects the events originating from the interaction vertex.

The COP is the multiwire proportional chamber located between the COZ and the CJC2, with similar pad design as the CIP. It has only 2 layers and the pads are significantly larger. It is used for triggering and especially for the vertex reconstruction.

Backward Proportional Chamber

BPC is the proportional gas chamber placed in the backward region in front of the backward calorimeter (Spacal). It consists of 3 supermodules with the sense wires strung perpendicularly to the beam line. Supermodules are tilted to each other by 45° . This ensures preciser calorimeter cluster position measurement and partial particle identification, especially of γ and electrons.

Forward Tracker Detector

The Forward Tracker Detector (FTD) is designed to provide accurate measurement of charged particle tracks in the forward direction. The chambers are situated in z between 128 and 242 cm covering the polar angular region from 4° to 30° . They consist of 2 different kinds of planar chambers P and Q grouped into 3 supermodules (see Fig. 2.4).

The Q chamber is divided in 28 smaller cells with 8 anode sense wires, whereas the P chambers contains 32 cells each with 4 anode sense wires. The sensitive wires in both types of cells are strung perpendicularly to the z -axis. The cathode planes are graded copper strips on the PCB enclosing the cell. The chambers are rotated in ϕ to each other within one supermodule

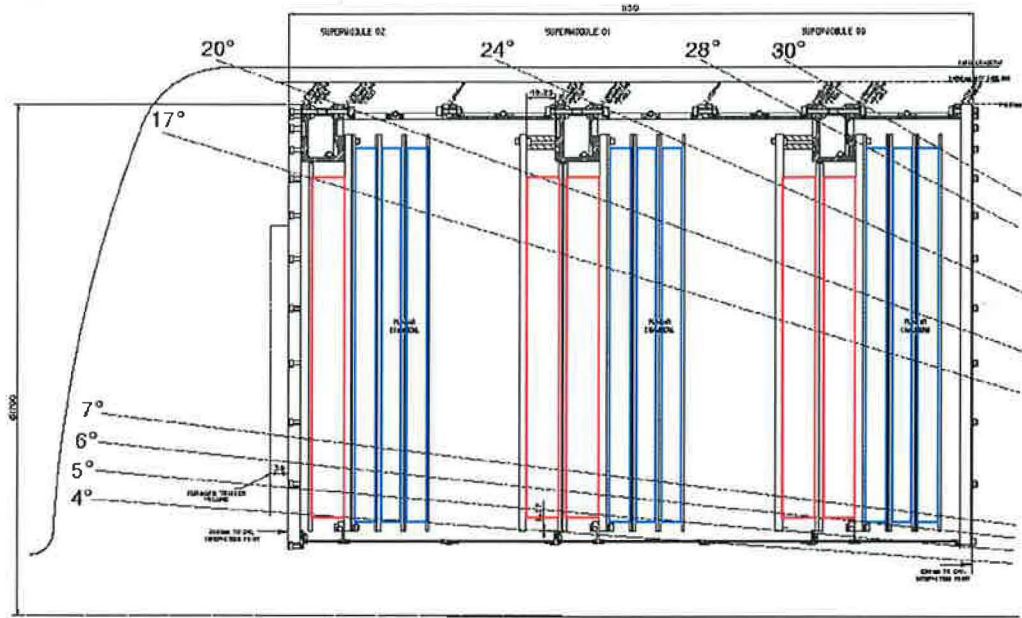


Figure 2.4: The Forward Tracker Detector (r, z) view.

to ensure better track reconstruction.

2.2.2 Calorimetry

The calorimetry measurement is based on Liquid Argon (LAr) Calorimeter [18] and Spaghetti Calorimeter (Spacal) [19]. Both parts together cover the pseudorapidity region of $|\eta| < 3.4$.

LAr Calorimeter

The LAr makes possible to measure energies in the forward and central region of the H1 detector, i.e. in the polar angle region $4^\circ < \theta < 154^\circ$ (see Fig. 2.5). It is a sampling calorimeter with the electromagnetic and hadronic section. It is build of 8 self supporting wheels each of them separated into 8 ϕ -sectors. Since the active medium is here liquid argon the whole calorimeter must be placed in a cryostat. The absorber plates made either from lead or stainless steel with independent readout cells are oriented horizontally in the central part and vertically in the forward part. The basic sampling pad shape cell of

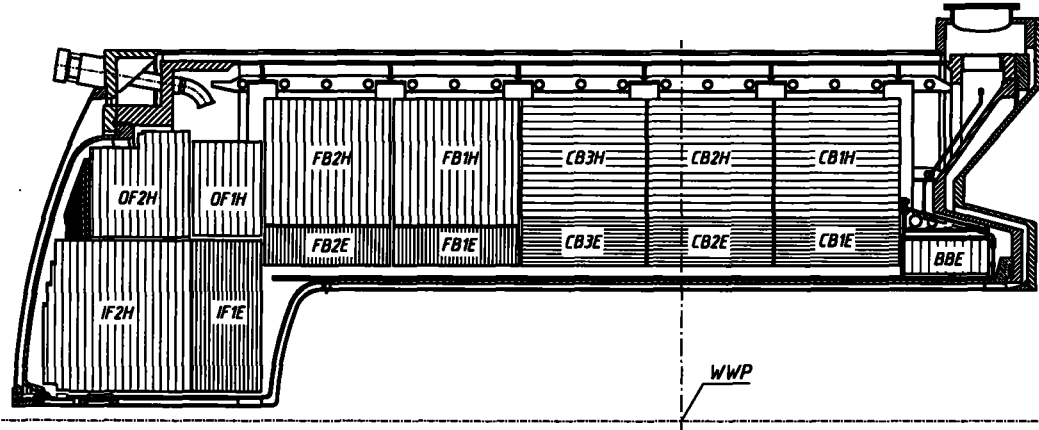


Figure 2.5: LAr Calorimeter.

the electromagnetic calorimeter consists of 2.4 mm Pb absorber and 2.35 mm gap filled with liquid argon. The copper pad is placed on G10-board mounted on the adjacent absorber plate. The hadronic sampling cell consists of the 19 mm stainless steel absorber and G10 board with the copper pads on both sides placed in the middle of the gap.

The longitudinal segmentation has been chosen to be 3–4 fold for the electromagnetic part over 20–30 radiation lengths and 4–6 fold for hadronic part over 5–8 interaction lengths. The granularity of the electromagnetic cells is about two times a Moliere radius as measured at the entrance of the calorimeter. The energy resolution for electrons reaches $\frac{10\%}{\sqrt{E}}$ and for hadrons $\frac{55\%}{\sqrt{E}}$.

Spacal

The Spaghetti calorimeter was designed for the precise e^\pm and γ energy measurement in the backward region of the H1 experiment. It is a lead/scintillating fibre calorimeter consisting of electromagnetic section of 28 radiation lengths long and hadronic calorimeter which is 1.02 interaction lengths long.

Both sections are built from the quadratic cells forming the circles with the inner radii of 10 cm limited by the focusing magnet GG and the outer radii of 80 cm to fit into the cryostat.

Every cell has scintillating fibres parallel to the z -axis pressed in the lead and at the end tied together to the cone to which a light mixer of the

photomultiplier is attached. The electromagnetic cells with the cross section $40.5 \times 40.5 \text{ mm}^2$ have the lead-to-fibre ratio of 2.3:1, whereas the hadronic section has the cells with cross section $119.3 \times 119.3 \text{ mm}^2$ and lead-to-fibre ratio of 3.4:1.

The backward calorimeter covers the angular area of $153^\circ < \theta < 177.5^\circ$ and have electron energy resolution $\frac{7\%}{\sqrt{E}}$. Since the Moliere radius of the electron in the electromagnetic part is about 25.5 mm a good e^\pm/π separation is ensured. Cluster position resolution is few mm. Additionally the Spacal is used for the triggering (for more details see [19] [20]).

2.2.3 Muon System

Muon detector of the H1 experiment is divided in two separate parts: Central Muon Detector (CMD) and Forward Muon Detector (FMD).

The CMD is placed in the iron yoke of the main solenoid magnet surrounding all major components (see Fig. 2.2). Its main detection component is constructed of limited streamer tubes situated in the slits of the iron yoke. It serves also as a hadronic tail catcher [13].

The forward muon spectrometer is placed in the forward region of the H1 experiment behind the CMD. It consists of the drift chambers on the either sides of the toroidal magnet. Its designed purpose is the detection of high energy muons between 5 to 200 GeV by reconstructing their tracks within the angular region of $3^\circ < \theta < 17^\circ$ [21].

2.2.4 Luminosity Measurement

The H1 luminosity measurement is estimated from the measurement of Bethe-Heitler process $ep \rightarrow ep\gamma$ which has rather high and precisely known cross section.

The system of detectors is situated far away from the interaction point and close to the beam pipe.³ It consists of electron taggers situated at $z = -5.4 \text{ m}$ (ET6) and $z = -40.0 \text{ m}$ (ET40), photon detector (PD) at $z = -101.8 \text{ m}$ and veto counter (VT) at $z = -101.4 \text{ m}$. The ET6 is an electromagnetic Spacal type calorimeter with 12 channels and depth 22 radiation lengths. The ET40 is a total absorption Čerenkov calorimeter with 6 channels (2x3 KRS₁₅

³The lumi detectors are movable in order to be protected from the radiation damage during the injection phase.

crystals) having a hodoscopic structure. The electromagnetic calorimeter made of quartz-fibre planes between the tungsten absorber plates is used as PD. The veto counter is a water Čerenkov detector of 0.15 radiation lengths long.

For online measurement ET and PD are coupled in coincidence to determine relative luminosity with a statistical precision of $\approx 2\% s^{-1}$ at nominal conditions. After offline corrections the absolute luminosity is measured with $\approx 5\%$ precision.

The luminosity system can be used additionally for photoproduction events triggering and for measuring hard photons from the initial state QED radiation.

2.2.5 Trigger System and DAQ

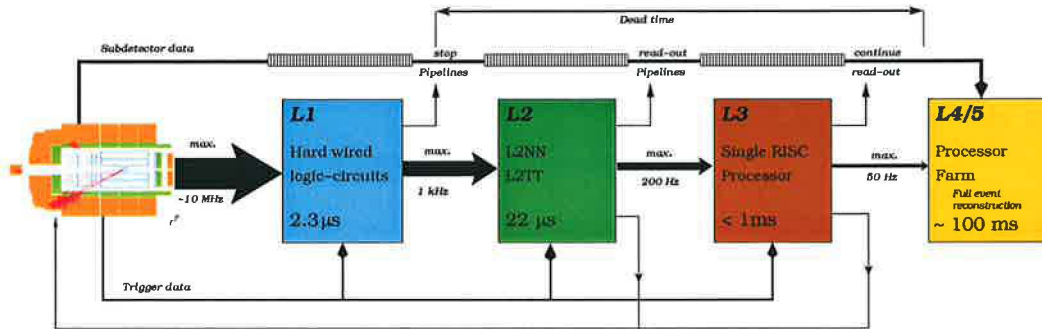


Figure 2.6: Schematic review of the H1 trigger system

Electron and proton bunches collide every 96 ns i.e. at 10.4 MHz rate, but the rate of interesting physics $e^\pm p$ interactions is much lower. DIS interactions have frequency of only few Hz. Unfortunately the rate of non $e^\pm p$ background events such as beam-gas, beam-wall interactions etc. is much higher.

Such a data stream can not be handled since the readout rate, data transfer and storage have limited capability. Therefore fast hardware and software algorithms have to decide whether to keep an event or not. The sophisticated multilevel trigger provides the event selection of relevant $e^\pm p$ interaction reducing the background rate.

The central trigger system consists of 4 levels. The complexity of the trigger algorithms increases with the level because the rate of events to be

treated decreases (see Fig. 2.6).

- L1** The L1 decision is based on the special trigger signals provided by various subdetectors which give 256 trigger elements combined into 192 subtriggers. An event is kept if one of the subtriggers gives positive decision delayed by $2.3 \mu\text{s}$ which is about 24 bunch crosses. The central trigger send an L1Keep signal stopping the subdetectors pipelines. Until the pipelines do not restart no data can be collected which contributes to the dead time. The subtrigger with too high rate can be suppressed using the so called prescale n . It means that only the n^{th} positive decision of this subtrigger is taken into account.
- L2** The neural network (L2NN) and topological trigger (L2TT) are implemented at L2. They verify or falsify the L1 decision working with more detailed information and having the response time of $22 \mu\text{s}$. After a positive L2 decision (L2Keep) the readout of all subsystems starts. The readout is finished after 1–2 ms which also contributes to the dead time of the detector. In case of negative L2 decision the pipelines are restarted to collect further data.
- L3** This level had not been active during the data taking used in this thesis. It had to act only after L2Keep signal and in case of negative decision the readout is aborted and the pipelines restart.
- L4/5** Since at this level complete information is available the full reconstruction and physics analysis proceed on the PC-farm. The events are processed asynchronously. If the decision of L1 and L2 triggers is validated the event is classified by L4 class software package. It can belong to one of the physics event classes e.g. "high Q^2 ", "diffraction", "open charm" etc. All events assigned to the physics classes are kept. The physics unclassified events are downscaled by the weighting factor L4weight.

Chapter 3

Forward Silicon Tracker Layout, Hardware and Data Acquisition

Forward Silicon Tracker (FST) was built¹ to provide the precise measurement of the charged particle tracks in the forward section of the H1 detector and to determine of the interaction vertex. It helps to identify forward scattered leptons and it increases the acceptance for the reconstruction of heavy flavour particles.

In this chapter the basic silicon detector properties are outlined, the FST detector geometry, properties and functionality of the front-end electronics and data acquisition system are described.

3.1 Silicon Detector Principles

The operating principle of silicon detectors is based on ionisation effects when charged particles pass through semiconductor material. There is a variety of types of semiconductor detectors which are used in high energy physics. This section is mainly focused on silicon tracking detectors. A detailed overview of

¹The tests of the silicon sensors and readout electronics, mechanic design and detector assembly were performed in DESY Zeuthen. Parts of the electronics (repeaters, subrepeaters and converter cards) were designed in Institute of Physics of the Academy of Sciences of the Czech Republic in Prague and their production was accomplished by the Czech industry.

principles and basics of other types of semiconductor detectors can be found in [23].

3.1.1 Semiconductors and their Properties

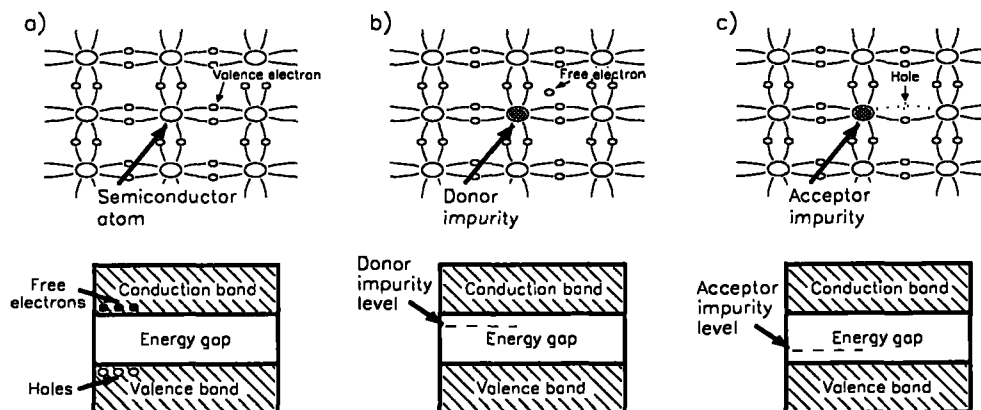


Figure 3.1: Structure of the semiconductor crystalline lattice and the energy bands: a) the pure semiconductor, b) the semiconductor with a donor, c) the semiconductor with an acceptor.

All semiconductors are crystalline materials with four valence electrons in the atomic shell (see Fig. 3.1 a). A pure semiconductor is an insulator at a temperature $0^\circ K$ with energy gap between the conduction and valence bands. The conductivity can be caused by exciting a valence electron into the conducting band accompanied by a creation of a hole. The excitation can be induced by an ionising particle or some thermal effect. The electron and hole become charge carriers or recombine.

To obtain conductive semiconductor material either pentavalent (donors) or trivalent elements (acceptors) are implanted into the crystalline lattice as depicted in Fig. 3.1 b),c). Since the pentavalent impurities cause the electron conductivity the semiconductor is called *n-type*. In case of the trivalent impurities the semiconductor has an excess of holes and is called *p-type*.

3.1.2 Semiconductor Detectors

The formation of the pn -junction is crucial for the functionality of the position sensitive semiconductor detectors. By applying bias voltage, positive pole on the n -type and negative pole on the p -type semiconductor, the depleted zone without free electron and holes is formed around the pn -junction which allows charged particle detection.

High enrichment with dopants is used for the electrical contact, because a direct contact of metal with semiconductor material would create the metal–semiconductor junction (so called Schottky diode).

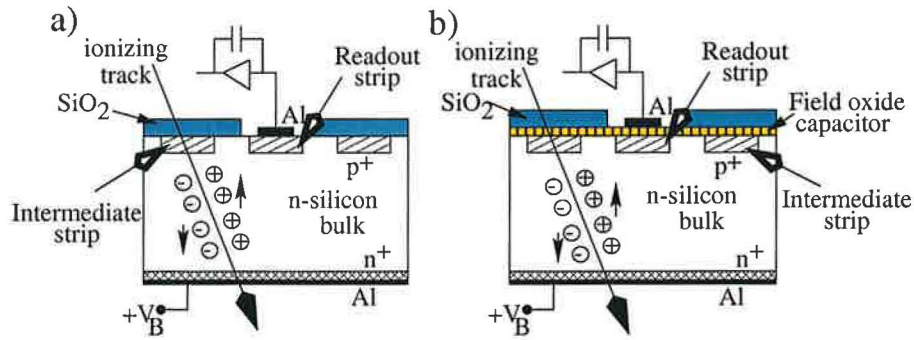


Figure 3.2: Schematic view of the passage of a particle through a semiconductor detector with readout elements. a) DC coupled readout, b) AC coupled readout.

Particles penetrating the semiconductor generate electron–hole pairs. Electrons start to drift to the n^+ layer whereas holes drift to the p^+ electrode as shown in Fig. 3.2. Such a semiconductor diode connected in reverse direction builds up a capacitor. The drifting of the electrons and holes will induce a charge on the capacitor electrodes which may be registered and amplified with a charge-sensitive preamplifier (see Fig. 3.2) placed as close as possible to the detector to avoid parasitic capacitances. Assuming two parallel electrodes at the distance d , the independence of the charge carrier mobilities μ_e , μ_h on the electric field and the density of donors much lower than acceptors, the time dependence of the induced charge caused by the drift of one electron–hole pair is given by the following formula:

$$Q(t) = Q_e(t) + Q_h(t) = \frac{e}{d} x_0 \left(\exp \frac{\sigma}{\varepsilon} t - \exp \frac{\mu_e}{\mu_h} t, \right) \quad (3.1)$$

where σ is the material conductivity, x_0 denotes the point where the electron-hole pair was created (the scale begins at the cathode), e is the elementary charge and $Q_e(t)$, $Q_h(t)$ are the charges induced separately from electrons and holes and ϵ is the dielectric constant of the material.

The microstrip detectors composed of separate strips are usually made of high resistivity *n-type silicon* on which p^+ doped strips are implanted. An n^+ layer is implanted on the opposite side. The electrical connection is provided by aluminium strips. Typically only every third or second strip is read out which is AC or DC coupled to the readout electronics (see Fig. 3.2). The thickness of such detectors is about $300 \mu\text{m}$ which corresponds to 25000 of electron-hole pairs created by a minimum ionising particle passing the detector perpendicularly. The average energy needed to create an electron-hole pair at room temperature is 3.62 eV .² The time of the charge collection is less than 10 ns.

If a particle passes the strip detector perpendicularly the charge is collected in one or two strips only. Due to the channel cross talk caused by the capacitances between neighbouring strips a small signal is visible on strips surrounding the hit strip too.

The implicit resolution Δx of a general strip detector is given by the equation

$$\Delta x = \frac{l}{\sqrt{12}}, \quad (3.2)$$

where l is the distance between the strips. By means of charge division better resolution can be achieved. The actual resolution depends moreover on the signal to noise ratio.

3.2 FST Layout

The FST placed in the forward region of the H1 experiment surrounds the elliptical beam pipe in the space between the $+z$ flange of the CST and the end of the central tracker. The radial extension of FST structures is limited by the available space between the beam pipe and a mounting tube below the adjacent cylindrical proportional chamber (see Fig. 3.3). It is divided into active part with silicon sensors mounted closer to the nominal vertex

²Since the energy gap is of the order 1 eV two thirds of the deposited radiation energy are spent on exciting lattice vibrations.

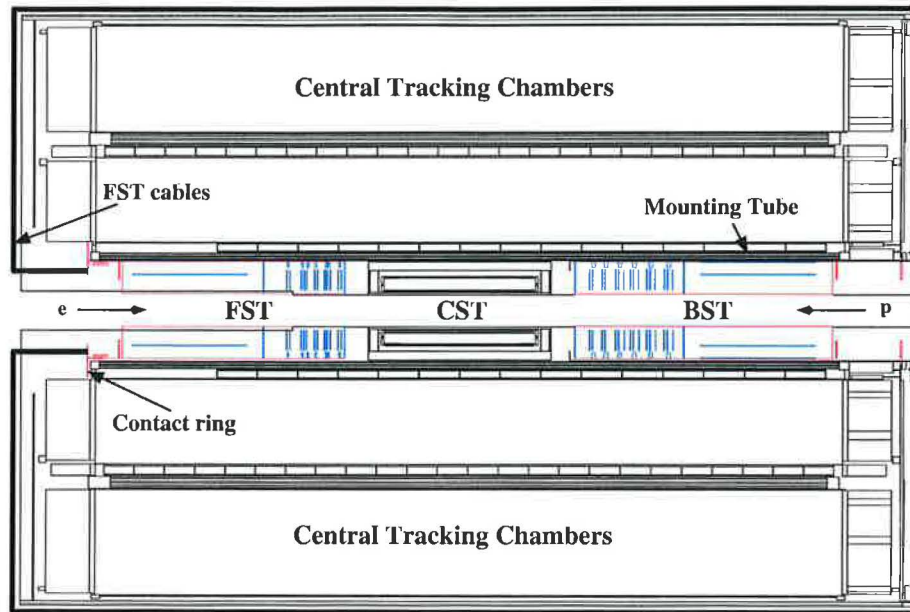


Figure 3.3: Arrangement of the silicon trackers in H1 detector

position and the readout part with front-end electronics. The (r, z) view of the FST is shown in Fig. 3.4. The front-end electronics is contacted to the supply cables and cooling media via so called contact ring. The detector frame is covered by a copper foil for shielding the electronics and protecting sensitive parts.

The active part consists of 7 carbon-fibre-composite (CFK) wheels five (see Fig. 3.5) of them equipped with the φ -strip modules (see Fig. 3.6) mounted back to back and two wheels with r -strip modules³ mounted on one side of the wheels only. Coordinates of the wheels are shown in table 3.1.

3.2.1 Active Part

Every strip module consists of the sensitive silicon sensor glued on the hybrid which houses front-end electronics. Every φ wheel is equipped with 12 modules on each side forming two planes. Since the sensors are mounted

³The r -strip detectors were installed to resolve the ambiguity in the r -coordinate measurement. They had been recycled from the modules of the BST used before 2001. Since they were found problematic, they were dismantled in 2005.

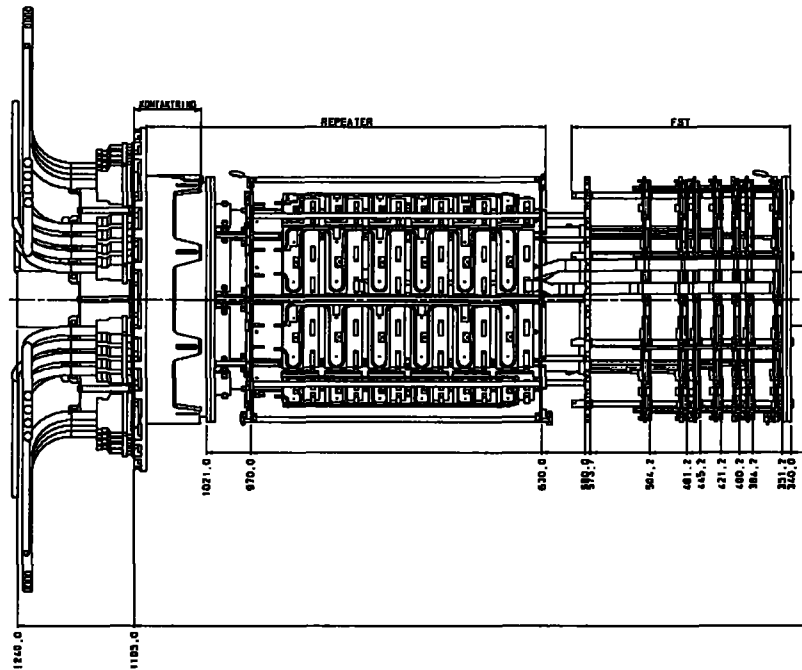


Figure 3.4: Forward Silicon Tracker (r, z) view with depicted contact ring, front-end electronics and the active part.

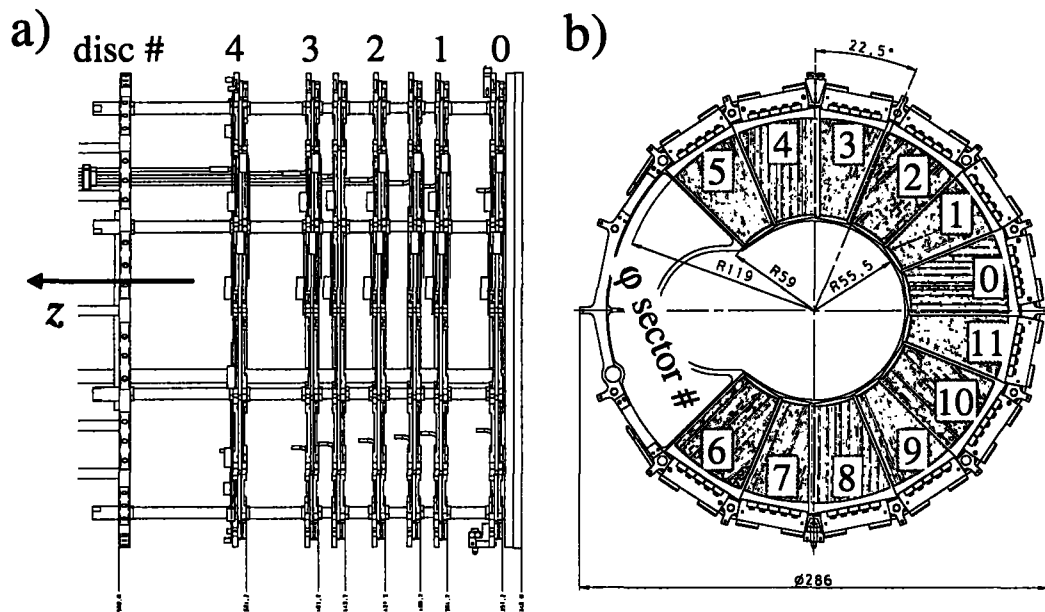
back to back their strips cross under the angle 22.5° achieving full spatial hit reconstruction. The sensors facing (back to) nominal vertex are called u (v) sensors. Because of elliptical beam pipe only part of φ acceptance is covered by these sensors. Filling the remaining angular region would require a special type of sensors which would be costly. The modules on one side are staggered in the z -positions to ensure their overlaps of about 1° . The parameters of the FST layout are summarised in Tab. 3.1.

φ Sensors

All Sensors have the same trapezoidal shape and size shown in Fig. 3.6. They have been manufactured from 6 inches wafers with the thickness $280 \mu\text{m}$ of the n-type silicon bulk. The p^+ active structures (strips) are ion implanted on the front side of the n-type silicon bulk whereas the enriched n^+ layer (back side) is made by high temperature diffusion. It covers the whole back-plane, the surface of which is covered with an aluminium layer. The sensor is AC coupled to the field oxide layer with a thickness of about 200 nm . The coupling capacitance between the aluminium and the silicon structure

minimum sensitive radius	58.77 mm
maximum sensitive radius	119.66 mm
<i>z</i> -position of <i>u</i> sector	
<i>u</i> disk 0	351.4 mm
<i>u</i> disk 1	384.4 mm
<i>u</i> disk 2	421.4 mm
<i>u</i> disk 3	461.4 mm
<i>u</i> disk 4	504.4 mm
<i>v,u</i> offset	9.1 mm
<i>z</i> -position of even <i>r</i> sector	
<i>r</i> disk 0	400.85 mm
<i>r</i> disk 1	454.35 mm
stagger odd/even sec.	-1.8 mm

Table 3.1: Nominal values of FST modules position.

Figure 3.5: FST active part: a) (r, z) view with disc numbering, b) a disk equipped with detector modules and with φ sector numbering.

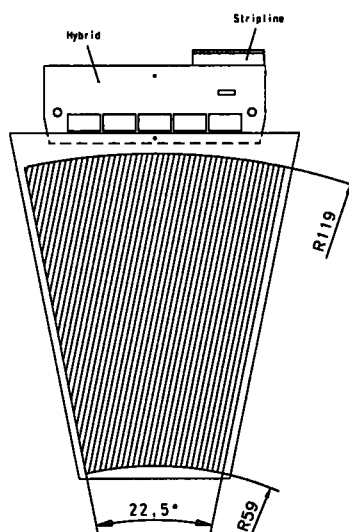


Figure 3.6: The φ module with schematically depicted strips and attached hybrid electronics.

underneath (width $10\ \mu\text{m}$) varies from 10 to 15 pF/cm.

The active area of a φ sensor is limited by an outer (inner) radius of 119.9 mm (59.0 mm) and by the borders parallel to the left and right edge of the sensor. The borders between the active area and the right and outer edge of the sensor are 1.5 mm wide. The strips have various lengths because they are parallel to one edge of the sensor. The surface of the sensor is passivated by the polyimid.

The strips are $12.5\ \mu\text{m}$ wide with the same gap between neighbouring ones. Every third strip is read out via the AC coupling composed of the aluminium strip of the same length as the strip separated from the p^+ silicon by the field oxide. The aluminium strip is contacted via contact pad in the upper part of sensor to the front-end electronics. The contact pads are gathered into five groups of 128 pads at the top of the sensor. Two intermediate strips lead to better charge division improving the spatial resolution of the detectors.

Two larger contact pads for the bias voltage and the guard ring are in the upper corners of the sensor. The p^+ area connected to the bias voltage leads around the whole active area. All strips need a sink for the leakage current. Therefore they are connected via the so called “punch-through” transistor to

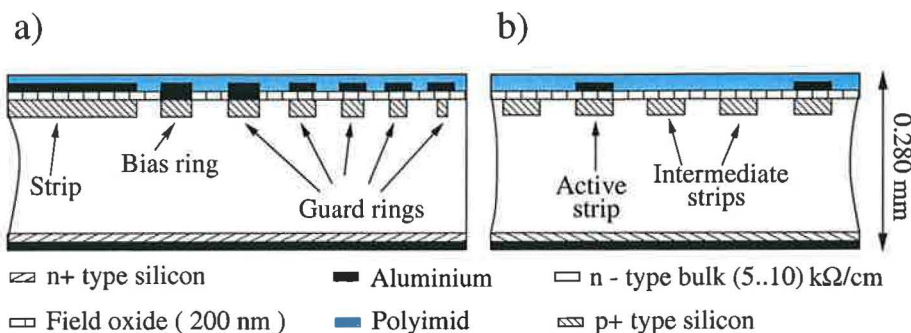


Figure 3.7: Cross section through the φ -sensor. a) Cross section along the strip. b) Cross section perpendicular to the strip.

the bias structure. This “punch-through” is made by a special design of the strip corner: A gap between the p^+ strip and the p^+ bias structure consists of n-material (bulk) forming the n-channel FET operated in pinch off mode.

The inner widest guard ring is also connected by “punch through” to the bias voltage ground. The outer guard rings are without a direct contact to the ground. They function like field effect transistors in series with a punch through effect similar to the bias voltage (see Fig. 3.7).

All the sensors has been evaluated in series of test before the installation (For details about tests see [24].).

3.2.2 Front-End Electronics

The aluminium support houses the front-end electronics which is placed on the $+z$ side of the active area of the FST (see Fig. 3.4). The aluminium frame causes more dead material than the CFK-frame of the active part, because it is not in overlap with the acceptance of other H1 subdetectors it does not have any significant impact.

On the aluminium support there are 6 repeater boards each of them carrying 6 subrepeaters. Four detector modules are contacted to the subrepeater via the flexible stripline of the hybrid. Front-end electronics functionality will be explained in section 3.3.

All the cabling has to enter the forward direction ($+z$) through a gap between the forward and the central tracker because the CST and BST do not leave any substantial place in the radial direction (see Fig. 3.3). Therefore a contact ring consisting of two parts matching together was designed as an

interface providing the contact for the electronics and cooling media.

3.2.3 Cooling

Whole detector is shielded by the copper foil on the outer and inner surface enclosing the detector completely to avoid any electromagnetic disturbances from outside. Since the electronics in the detector become hot during the operation two water cooling circuits ensures the heat dissipation.

The cooling for the hybrids consist of copper tubes built in the profile on the circumference of the CFK wheel. All pipes are then brought together resp. separated in the two distributor units placed between active and passive part of the FST.

The subrepeaters are cooled by another circuit. Two copper pipes, one as an input, one as an output are leaded in the space above the repeater in $+z$ end of the detector. On every pipe there are six openings to which aluminium plates with copper pipe soldered on the whole surface are connected in such a way that water runs through cooling the subrepeaters. The detector area is vented by nitrogen boosted into both active and passive parts of the detector to lower the humidity and the dew point eluding the water condensation.

3.3 Electronics

To ensure preshaping, storage, readout and amplification of the signal from the silicon sensor avoiding disturbance of other systems of the H1 experiment part of the front-end electronics is installed closer to the active region of the FST.

3.3.1 Hybrid

The electronic components placed on the hybrid ensures the analog signal amplification and shaping. The printed circuit board (PCB) is processed by the multilayer Starr-Flex-Technology with an aluminium layer. There are glued five APC128 chips and one decoder chip with their contacts bonded to the PCB. There are 128 active strips bonded to every APC128 chip. The APC chips are read out serially driven by the decoder (More details about the APC128 and the decoder functionality are presented in appendix A.).

The sensor is glued to the hybrid which ensures the mechanical stability of the module and fixing to the CFK frame. The coupling between the hybrid and the sensor is electrically conductive which provides the connection of one bias voltage pole. The aluminium layer at the bottom coupled to the cooling system ensures the heat dissipation. The flexible stripline of the hybrid is connected to the subrepeater.

3.3.2 Repeater and Subrepeater

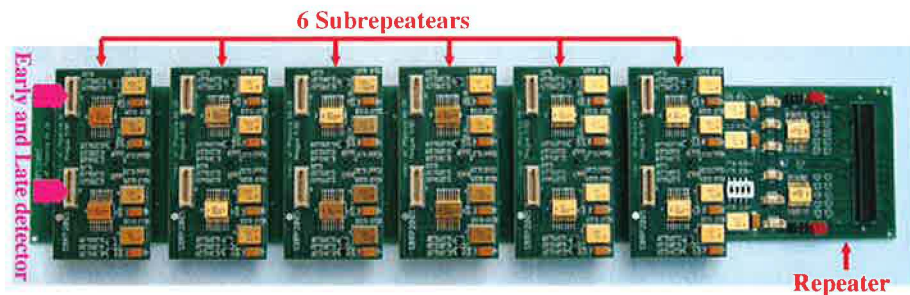


Figure 3.8: Repeater board with all 6 subrepeater modules.

The analog signals of a pair of detector modules from neighbouring φ sectors (early and late)⁴ are buffered in the subrepeater into one data channel and then they are amplified. The data channel contains 1280 amplitudes from readout strips. The subrepeater houses two data channels and provides the clock distribution and supply for all four detector modules. The digital voltage and analog current from the source are stabilised on the subrepeater to fit the chips supply requirements.

Six subrepeaters are plugged into the repeater (see fig. 3.8). The repeater itself provides mainly the distribution of the supply and data signals. The serial linked I/O (SLIO) chip provides the interface for the temperature and humidity sensors which are spread over the detector volume to detect possible overheat or water leaks.

Two pairs of set of bipolar clock signals are received by the clock boosters on the repeater and transformed to unipolar signals to be distributed to the subrepeaters, where they are transformed again to the bipolar signals suitable for the decoder chip.

⁴A pair of detector modules is read out sequentially.

3.3.3 Detector Supply

Several supply voltages are necessary for the detector module, the bias voltage for the sensor depletion, the analog and digital voltages for the chips supply. The bias voltage for the sensor can reach up to 100 V. The hybrid chips require two digital voltages of 5 V and 2.5 V and the analog current of 90 – 120 mA. All voltages provided by converter cards are processed in the subrepeater to reach the mentioned values.

Each converter card supplies 8 data channels via two 50 pin cables connected to the contact ring at the detector side with set of digital/bias voltage and the analog current source. The supply module functionality is driven by the VME bus (for details see appendix B). The analog data signals are fed through the card and contacted via two 20 pins (cori) cables to the ADC. The signal level can be adjusted at the converter to meet the ADC digitisation range.

The digital voltage and the analog current are floating and transformed from the VME-bus voltages. The analog current source has been chosen to provide the stable analog voltage because of the power requirements of the chips changes. There must be additional 50 V at the user bus in the crate which are transformed to the floating bias voltage adjustable in range 0 – 128 V with step of 0.5 V.

3.3.4 Clock Signals

Analog signals from the strips are read out by the APC128 chip, switches of which are driven by the decoder processing 4 bipolar clock signals (see appendix A).

The sequence of the clock signals can be programmed in so called sequencer code which is then downloaded into the VME module OnSiROC⁵. It generates the appropriate clock signals reacting to the trigger signals of the H1 trigger system. The clock signals are then send from OnSiROC to the Clock Distribution Unit (CDU).

The clock signals can be delayed with respect to each other by few ns to match the detector modules requirements. The CDU provides 4 outputs of the clock signals. Each output can be connected via 20 pin cable to the detector being received at one of the repeater clock receivers. Additionally the supply for the receivers is transformed from VME bus voltage. To

⁵Online Silicon Readout Controller

compensate the long cable capacitance (inductance) the piggy backs with corresponding capacitance can be plugged parallel to every output.

The repeater receives two inputs of the clock signals. The clocks are shaped, amplified and transformed from bipolar to unipolar signals to be distributed to the subrepeaters. In the subrepeater the received clock is again shaped by the transceivers and transformed to the bipolar signals to match the connected detector module requirements.

Although the clock system looks complicated it ensures the proper clock signal shaping avoiding disturbance by the outer noise possibly generated by the other systems. Clocking is crucial for the functionality of the FST.

3.4 Slow Control

All non front-end electronics for supply and clocking are VME modules which are being controlled by the complex slow control program. The requirements for user friendly interface, monitoring response as fast as possible, sending the status to the H1 experiment and the flexibility of the system lead to the schema shown in Fig. 3.9 (A detail description of the modules and their functionality is presented in appendix B).

The slow-control of the FST is driven by the Labview program running on the MacIntosh computer with the NuBus Micron card which provides the MacVEE bus to which up to 8 MacVEE cards can be connected. The MacVEE card acts as master in the VME crate able to handle only A24 or A16 addressing.

As it is visible in Fig. 3.9 the needed and minimal version of the FST slow control consists of 2 (OnSiROC and Converter) crates⁶ each with 1 MacVEE dedicated for the FST.

The OnSiROC crate houses OnSiROC and CDU units for the FST and for the BST too. The OnSiROC modules are monitored and the sequencer code is downloaded into the modules by the slow-control program.

The main part of the hardware driven by the slow control program is situated in the converter crate. Besides the 9 detector supply units (Converter cards) it houses IP-ariet with IP-Can SLIO and IP-Unidig modules, Watchdog card and the Status Link interface card.

⁶The crates are both VME with different depth, supplies and additional user buses to meet the module requirements.

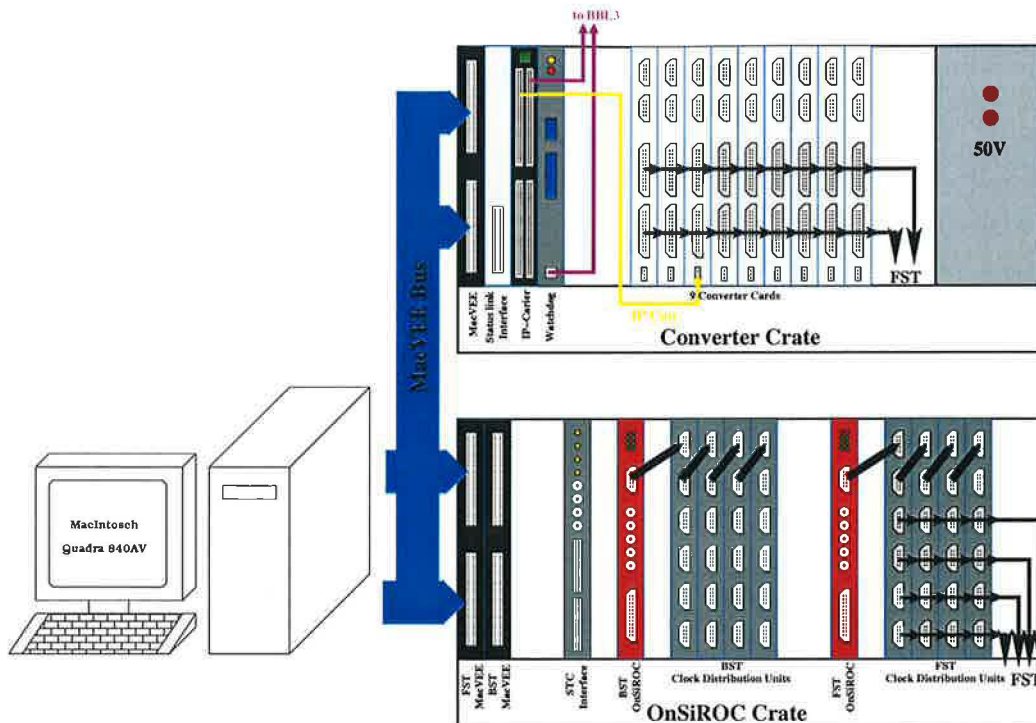


Figure 3.9: Slow control of the Forward Silicon Tracker.

The supply voltages for 8 detector data channels are controlled by means of one converter card. Together 9 converter cards are necessary for the FST. In addition the status of the supply is send via a status link bus through the interface card to the DAQ crate.

The temperature measurement in the FST is obtained from the SLIO circuitry on the repeater boards by means of the IP-Can SLIO module plugged in the IP-Carrier. The serial data transfer port of this module is connected through the converter card which connects data cable with the input of the repeater SLIO chain. The values are interpreted by the slow control program.

The status of the detector is additionally provided for the experiment by means of the IP-Unidig module connected to the H1-BBL3 system. Three signals are send to the BBL3: voltage status, high voltage status and temperature alarm.

To monitor the functionality of the slow control program the Watchdog card register is polled otherwise a BBL3 signal is send from this unit to inform the H1 system of non-functionality of the FST slow control program.

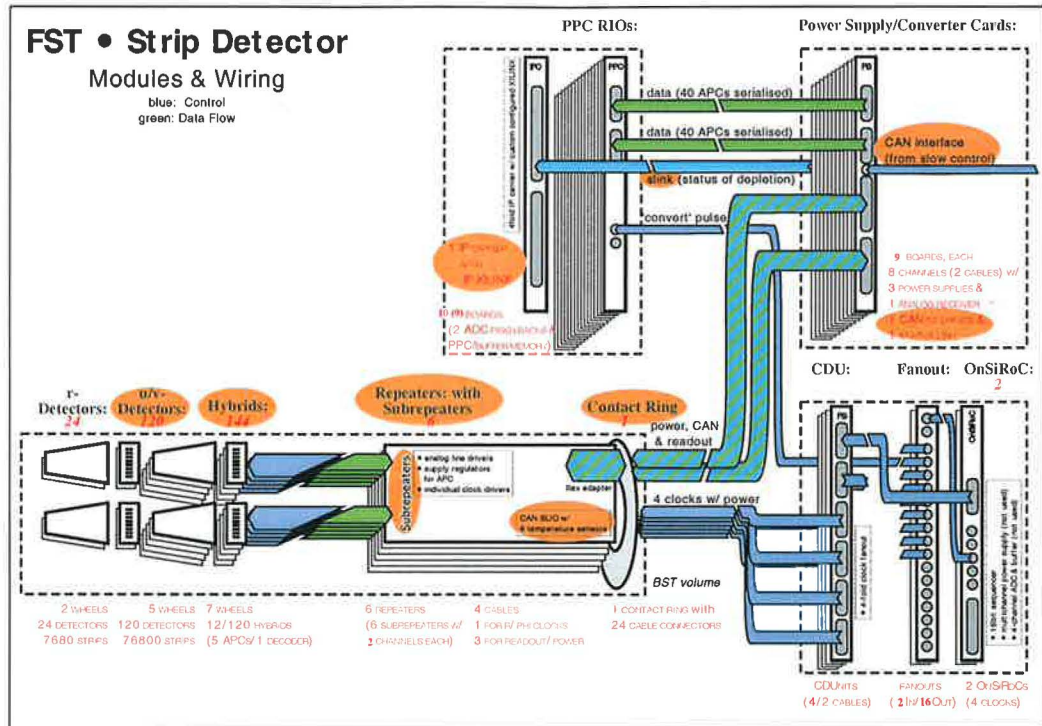


Figure 3.10: FST data acquisition chain with depicted clock and signal flow.

3.5 DAQ

The signal from the readout strip is amplified by the APC128 charge sensitive preamplifier and stored in the sampling pipeline every beam cross until the positive trigger decision arrives. The desired signal is read out by clocking in the sample register to appropriate pipeline given by the trigger delay. Every strip of 2 sensors (1280 strips) is readout sequentially by clocking through the APC128 readout pipeline (for more details see appendix A) driven by the OnSiROC clock. In this way one analog data channel is formed.

The analog signal of every data channel is amplified in the subrepeater and converter card. Additionally the level of the analog signal can be adjusted at the converter to match the digitisation voltage range of the ADC placed on the PMC board of the RIO 8062 card. A detail data and clock control signals flow are schematically depicted in Fig. 3.10.

The analog signal of every strip is converted to the 12 bit amplitude. The conversion is triggered by the NIM convert pulse which is programmable in

the clock sequence and send by the OnSiROC and distributed by the NIM fanout card to the appropriate PMC.

The raw amplitudes from an event are transferred from PMC in the RIO memory via FIFO. The code SiPPCUser running on the RIO board in normal data taking mode executes the hit finding procedure (see 4.1) storing compressed information about hits only and leaving them in bank format with data length and identification stored. When available the hit banks are taken by the master unit (VMETaxi, VMEPC) and send to the H1 DAQ for further processing by the track reconstruction program.

3.5.1 Event Building

The DAQ of the silicon trackers is divided into subbranches corresponding to each subdetector (see Fig. 3.11). The subbranches FST, BST, CST⁷ are reserved for readout of the strip detector data. The STC branch is meant for BST Pad detector readout and for handling and distributing the trigger signals to and from other subbranches.

Data from all subbranches are collected by the SiEventBuilder routine for each event, processed into the bank format and send to the H1 DAQ system for further processing.

The hardware in the strip detector subbranches (see Fig. 3.12) is basically identical within minor differences. The communication between DAQ Master board (VMETaxi or VMEPC) in the PPC crate and CES RIO 8062 [31] board is ensured by VME Bus. The event building is driven by 3 routines.

- i) The SiDAQ routine running at the master board collects data from the RIO boards. It ensures the communication between the master board and the RIO boards by writing the H1 DAQ parameters specifying common run conditions and the silicon DAQ parameters (see C.8 and C.9).
- ii) The R2PowerPC routine runs at each RIO 8062 board as a main routine. It initialises the RIO board, PPC processor, VME parameters and PMC⁸. It ensures communication between the PMC and the processor and it is responsible for the communication with the master board. In addition it calls the hitfinder routine.

⁷One RIO DAQ board housed in the CST PPC crate is used for BPC.

⁸PCI Mezzanine Card

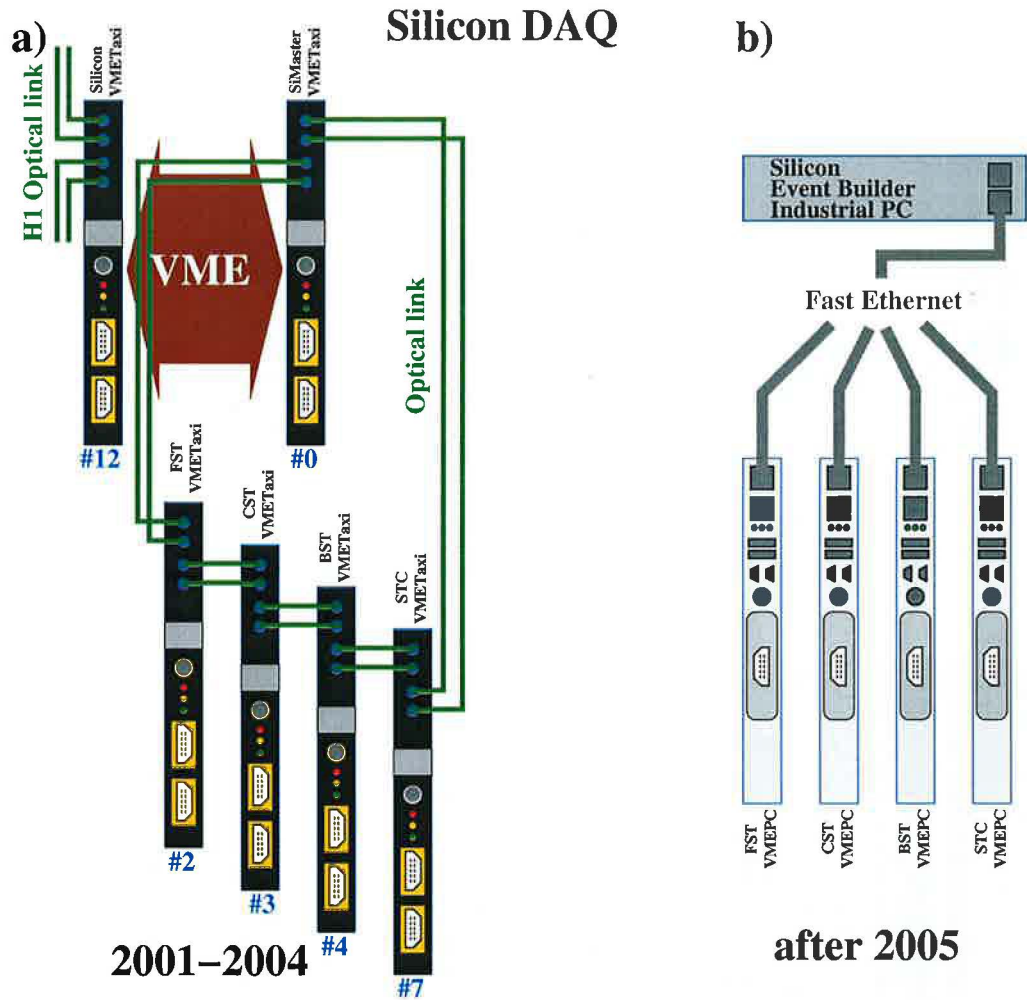
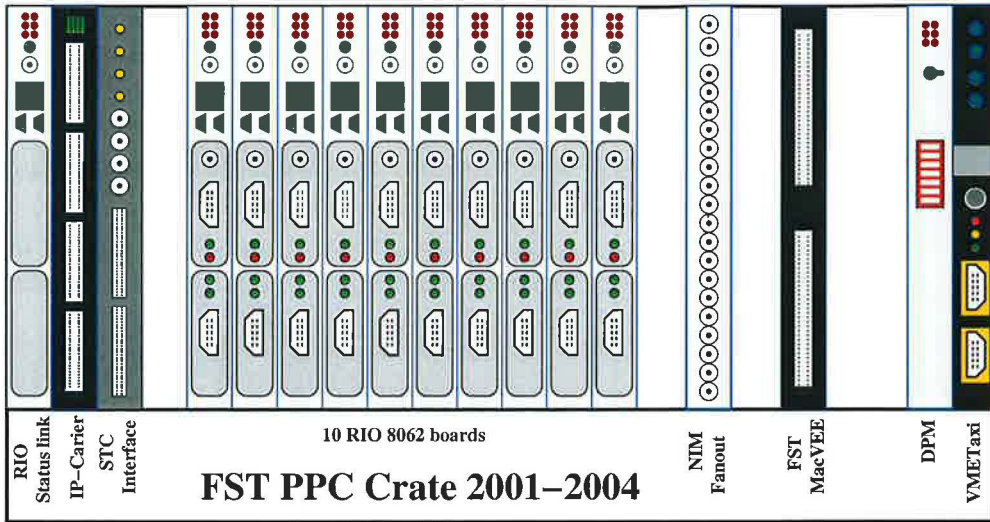


Figure 3.11: Silicon DAQ: a) The optical ring build from the VME Taxis. The communication and data transfer between Silicon Master VME Taxi (Silicon Event Builder) and H1 DAQ was ensured by the VME connection to the Silicon VME Taxi. b) Modified Silicon DAQ used since October 2005. The VME Taxis has been replaced by VMEPC which are connected to the Silicon Event builder by the fast ethernet and communication to the H1 DAQ is provided by the same connection from the Silicon Event Builder.

- iii) The SiPPCUser subroutine (hitfinder) processes raw data by finding hits and storing formatted data. Since the SiPPCUser is often modified

a)



b)

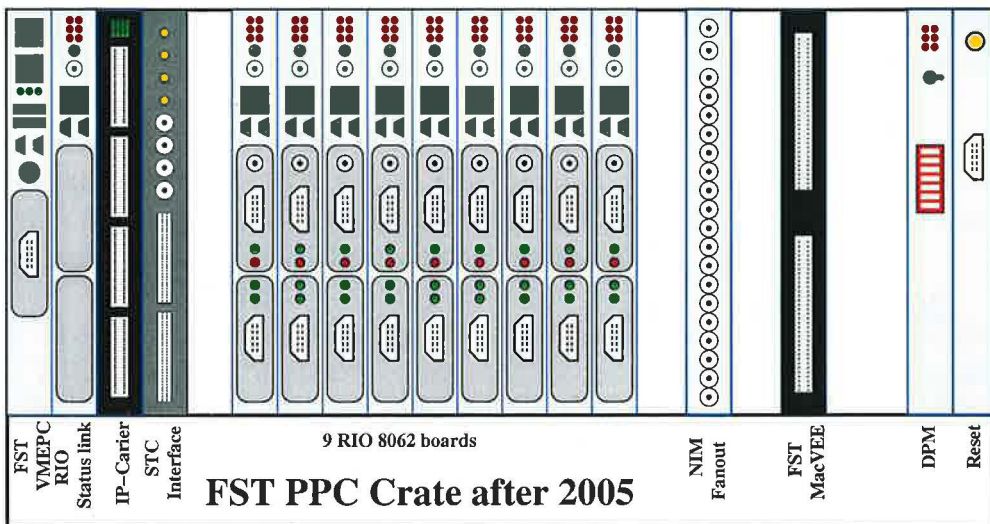


Figure 3.12: FST PPC crate: a) 2001-2004 b) Since October 2005 after Silicon DAQ upgrade.

it is downloaded into the RIO board memory from the DPM board (see C.5).

FADC PMC Signal Digitisation

The FADC PMC is a customer build PCI mezzanine module for CES RIO 8060/8062 design by RAL⁹ for digitisation of the analogue signals of the H1 silicon detectors.

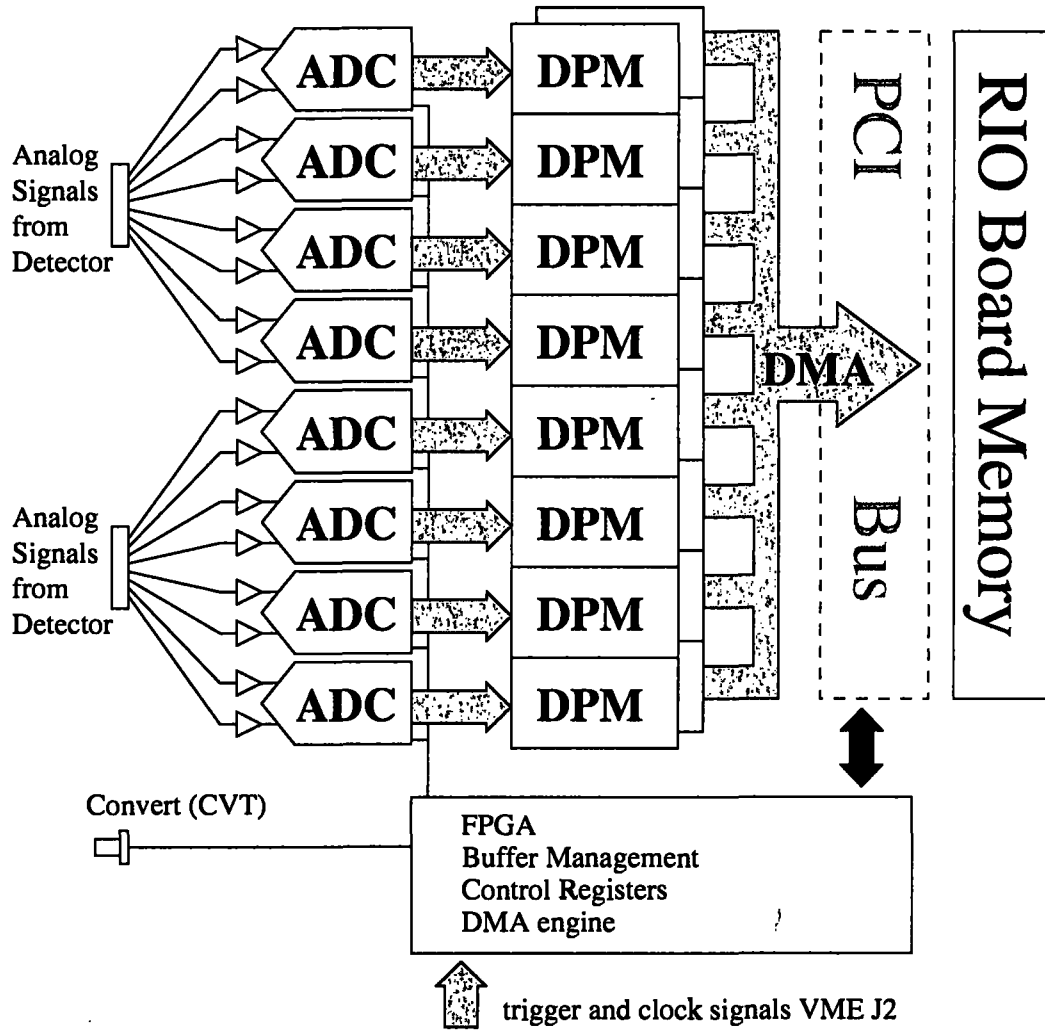


Figure 3.13: Schematically depicted digitisation of the analog signals and the data flow in the PMC.

The event building is synchronised by the H1 trigger and the clock signals

⁹Rutherford Appleton Laboratory

which are delivered on the VME-J2 user bus by the STC interface card plugged in the PPC crate. The digitisation of the analog signal is triggered by the convert pulse (CVT) delivered by the OnSiROC which is distributed by the NIM fanout card to the lemo connector on the FADC PMC board.

FADC digitises analogue signals of 8 data channels (8x1280 strips). For a given event 1288 analogue signals can be converted into twelve bit amplitudes per channel which corresponds to a number of strips read out by 10 APC128 chips sequentially plus 8 calibration signals.

The amplitudes are stored for each event to one of two buffers of PMC dual-port memory (DPM). One buffer is being filled by the ADC while the other is being emptied by a direct memory access (DMA) according to the address in the FIFO into one of 16 RawData memory buffers in the RIO board memory. The schematic diagram of the PMC memory and the data flow is depicted in Fig. 3.13.

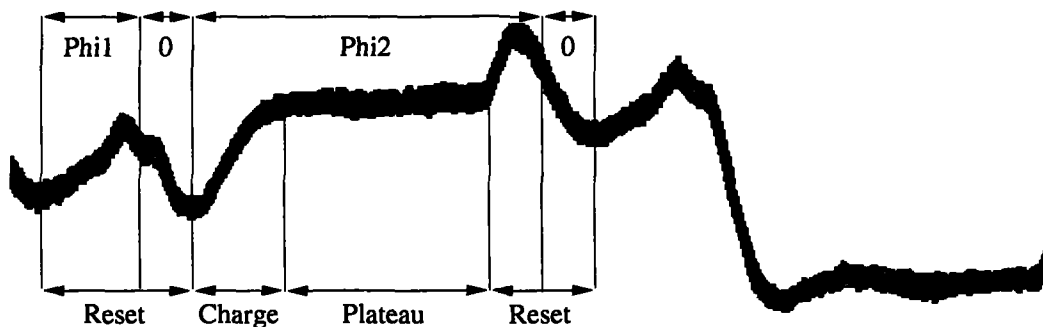


Figure 3.14: Analogue signal from one strip with depicted phases according to the clock signal which drives the readout.

The incoming analogue signal from one strip consists of three phases as it is shown in Fig. 3.14: reset, charge and plateau. The CVT pulse of at least 48 ns length has to be synchronised to trigger the conversion, when the plateau arrives. There is a delay between CVT and the digitisation which has to be foreseen in the sequencer code¹⁰.

By handling the trigger signals the PMC stores also the event number as the count of L2Keep signals and the pipeline counter (PIC) number obtained by counting the clock pulses generated in the sampling phase of the H1

¹⁰Additionally there is a delay of the signal caused by cable length.

detector. The PIC corresponds to the position in the sample register of the APC.

Silicon DAQ Protocol and Data Processing

The process of event building with the subroutines and memory blocks is schematically depicted in Fig. 3.15. The FADC PMC reacts to the trigger

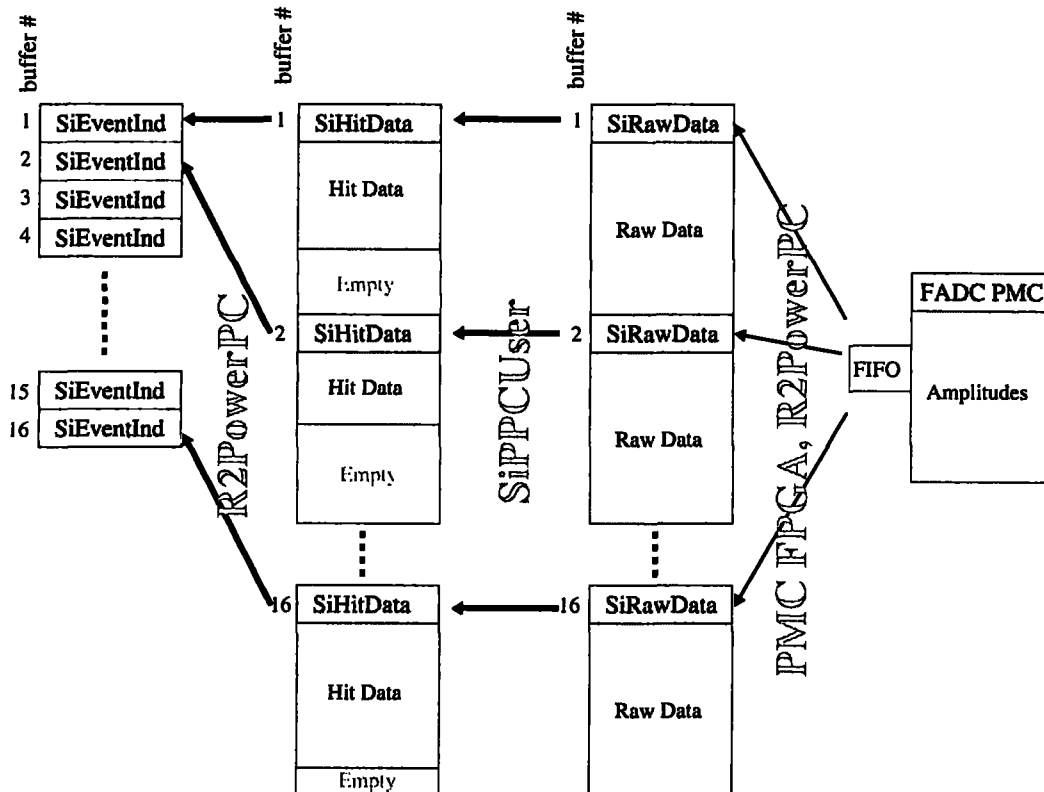


Figure 3.15: RIO board memory organisation with schematically depicted routines.

signal and stores the digitised amplitudes from one of its internal buffers to one of 16 RawData buffers accordingly to the address in PMC FIFO. The R2PowerPC subroutine ensures that the FIFO register always contains an address of the free RawData buffer or 0 in case there is no free buffer.

The lowest event in the RawData buffer is processed by SiPPCUser subroutine which requires the RawData address, event number, pipeline counter

number, high voltage status (FADC HV Mask) and desired format of the data (SiMode)¹¹.

SiPPCUser routine process the data, stores the packed data into a HitData memory buffer and exits back to the R2PowerPC routine returning length of the hit data. It writes then the parameters of the processed event into the event identification area EventIND (see Tab. C.10).

The length of the HitData can differ event by event. Memory buffers reserved for them are of the same length equal to RawData buffer length. The data in the buffer stays there until the master routine takes them and sets the event number in the EventIND to 0. Then the corresponding buffer is set free and can be used for further events.

¹¹There is a special mode when the SiPPCUser subroutine is not called and the RawData are directly taken by the master board.

Chapter 4

FST Response

In this chapter some aspects of the particle detection in the FST and the data reconstruction are explained with the focus on the resolution, acceptance, efficiency and occupancy.

4.1 Reconstruction

The reconstruction of the FST track starts by the hitfinding procedure. The found hits are then combined in clusters which are further used for tracking and an estimation of the track parameters.

4.1.1 Online Hit Reconstruction

The hit reconstruction program running online on the RIO board finds hits by processing the digitised amplitudes for every strip. Stored raw data of one FADC channel contains 1280 amplitudes digitised from one readout channel. The raw data signal Rd_i of the strip i consists of several contributions,

$$Rd_i = Ped_i + \Sigma_i + Cm_{128} + Ph_i. \quad (4.1)$$

The aim of the hitfinder is to subtract the pedestal (Ped) and the common mode (Cm_{128}) and to distinguish the pulse height (Ph) of the signal induced by the particle from the noise (Σ). The pulse height then writes

$$Ph_i = Rd_i - Ped_i - Cm_{128}. \quad (4.2)$$

It is obtained in several steps shown in Fig. 4.1. In the first step the pedestals are subtracted. By the subtraction of the pedestals the nonlinearities in the

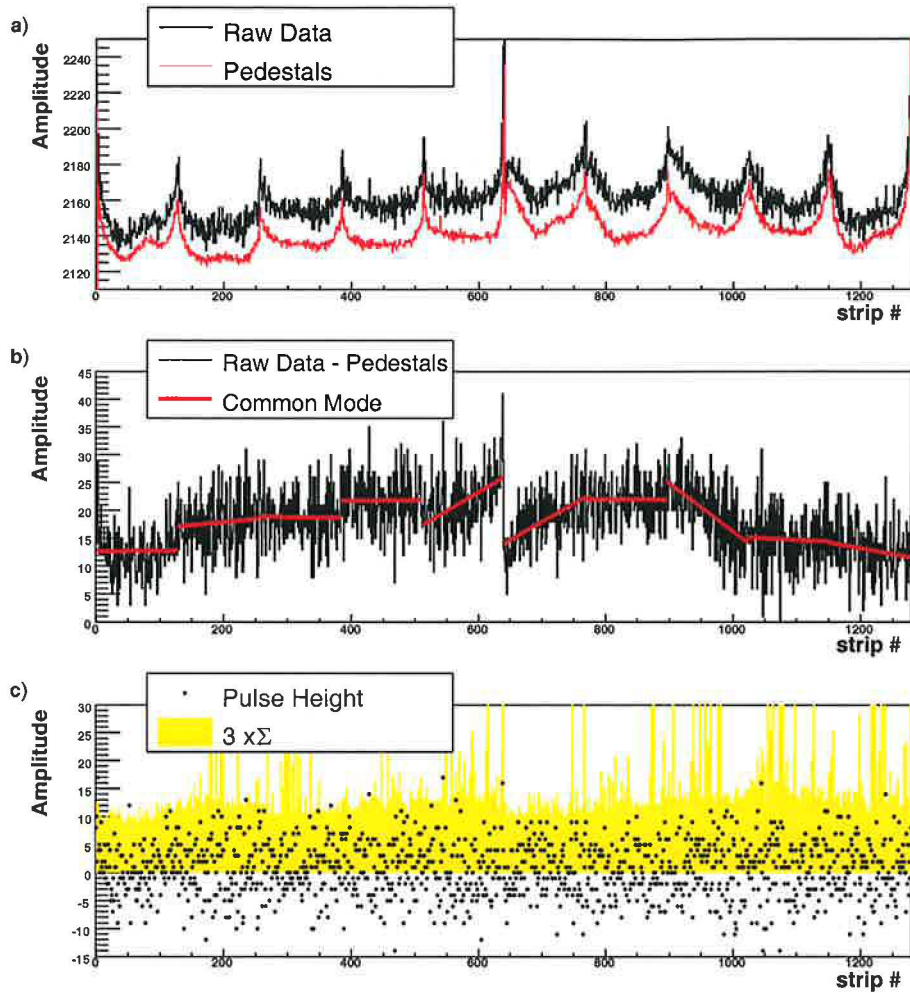


Figure 4.1: An example of hitfinding procedure for one channel of the FST. a) Raw data with pedestals. b) Raw data with subtracted pedestal and fitted common modes. c) Data with subtracted pedestals and depicted region of $3 \times \Sigma_i$.

shape of the spectra and spikes caused by the dead strips are suppressed which is crucial in the common mode calculation.

The common mode contribution stems from the shift of the common baseline of the signals of one detector between single events. It is caused by the short term fluctuations of the bias voltage of the silicon sensor and

front end electronics supply voltages. Since the smallest electronic unit is the APC128 chip common mode is calculated as linear regression of 128 amplitudes after the pedestal subtraction. Ten common modes obtained for one data channel are subtracted to determine the pulse heights.

The pulse heights are compared with the variations $Var_i = \Sigma_i^2$. The assignment of the hits is evaluated by the following conditions:

$$Ph_i > 0, \quad (4.3)$$

$$Ph_i^2 > Var_i \times Cut_{const}, \quad (4.4)$$

where $Cut_{const} > 1$ is a confidence level constant applied to suppress the noise. The raw data amplitudes are stored in 12 bits and thus the first 4 bits are unused. The highest unused bit of the data word is used to mark the hit data.

The procedure is repeated once again from second step. The already marked hits are excluded from calculation of the common mode. The hits found after the second iteration are marked, their positions (strip number), amplitudes and variations are stored and later send for offline analysis. The data without marked hits are used for pedestals and variations update.

Pedestal and Variations Initialisation and Update

Pedestal is an average amplitude specific for every strip when no particle induced signal is present. Pedestals are initialised at the beginning of the data taking and updated to react to possible changes caused by temperature variations etc. Since the properties of the pedestal and noise are dependent on the front-end electronics their values are further segmented by the storage pipeline number in APC128 chip (PIC).

The pedestal is updated by means of the weights (w), raw data without common mode in the current event (n) and the pedestal from the previous events ($Ped_{i,n-1}$),

$$Ped_{i,PIC,n} = \frac{w_{PIC,n} \cdot Ped_{i,PIC,n-1} + (Rd_{i,PIC,n} - Cm_{128,n})}{w_{PIC,n} + 1}. \quad (4.5)$$

The variations Var_i are updated in the same manner as the pedestals,

$$Var_{i,PIC,n} = \frac{w_{PIC,n} \cdot Var_{i,PIC,n-1} + (Rd_{i,PIC,n} - Cm_{128,n} - Ped_{i,PIC,n})}{w_{PIC,n} + 1}. \quad (4.6)$$

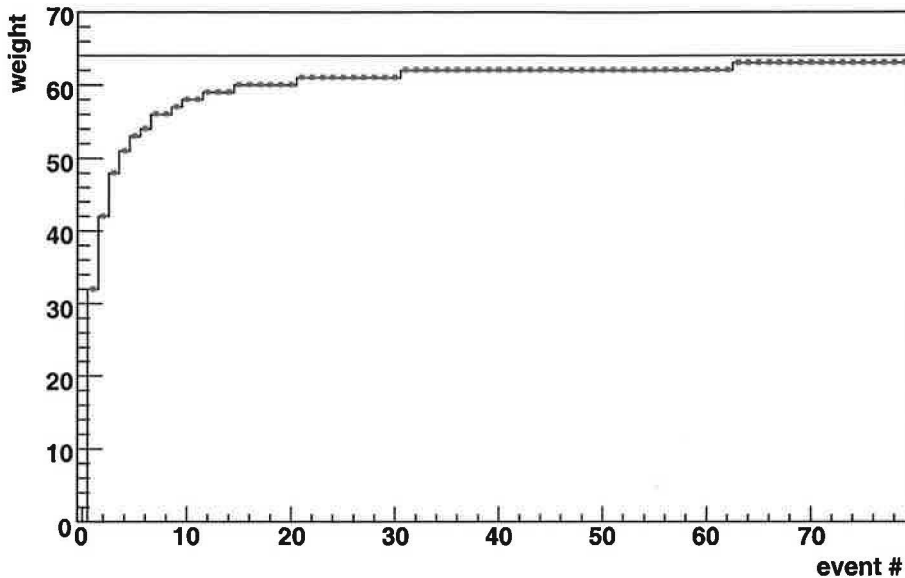


Figure 4.2: The weights for pedestals during the initialisation

The weights change at the beginning of the data taking in order to properly initialise the pedestals and variations. The value of the weight remains 63 after the initialisation is finished. Pedestals and variations are updated reflecting possible changes in the detector response (see Fig. 4.2).

4.1.2 Cluster Reconstruction

Hit amplitudes delivered by the hitfinder for offline reconstruction are further combined into clusters. The deposited charge induced by a passing particle is distributed to two closest strips according to the relative position of the passage. The signal amplitudes from these strips corresponds to the amount of the collected charge. Having amplitudes from two neighbouring strips the relative position of a hit between two strips can be calculated as

$$\nu = \frac{A_{n+1}}{A_n + A_{n+1}}, \quad (4.7)$$

where A_n , A_{n+1} denote the amplitudes from the strips n , $n + 1$ and ν is the asymmetry. The relative position of one hit clusters is defined to be $\nu = 0$.

Clusters with more than 3 hits are considered to be 2 hit clusters, the lowest amplitude is not included into the asymmetry calculation since it is caused by the cross-talk of the capacitances between two strips.

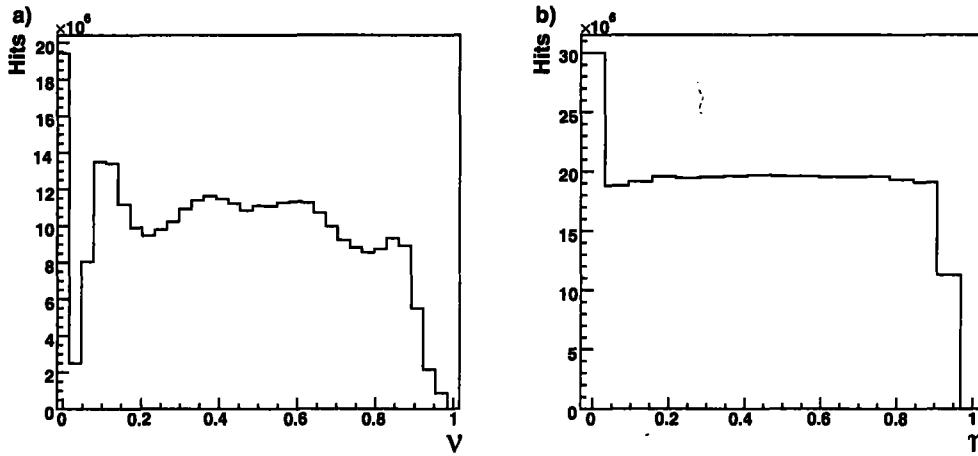


Figure 4.3: a) Distribution of the asymmetry ν . b) Distribution of the corrected asymmetry η .

The electrical field between strip and the backplane is not homogeneous in the whole volume of the sensor. Inhomogeneities are centred around the intermediate and active strips (see Fig. 4.3 a) because of field distortions around the strips. The higher population at 0 is caused by the contribution of one-hit clusters. To reach a homogeneous distribution and more precise asymmetry estimation η a correction to the variable ν is applied (see Fig. 4.3 b).

4.1.3 Tracking

The track reconstruction is done in two steps.

- i) **2D pattern recognition** where obtained 2D coordinates of clusters are fitted by the parabolas.
- ii) **3D track fit** where the parabolas are combined forming space points which are used for a helix fit.

The alignment of the detector plays an important role in the reconstruction of hit positions.

2D Pattern Recognition

Two coordinates can be determined from the reconstructed cluster. The coordinate ξ of the hit which denotes the distance from the first strip of the sensors (relative position of the hit within the sensor) is calculated as:

$$\xi = (-1)^t (n + \eta) \cdot d, \quad (4.8)$$

where $d = 75 \mu\text{m}$ is the readout pitch, n is a strip number for which the corrected value of asymmetry η was calculated. The sign of the coordinate is denoted by the type of the detector t .

$$u : \quad t = 0 \quad (4.9)$$

$$v : \quad t = 1 \quad (4.10)$$

The second coordinate of the hit is given by the nominal z -position of the detector module.

All reconstructed cluster coordinates from u -sensors within one ϕ -sector and from v -sensors in neighbouring ϕ -sector are fitted by the parabolas (see Fig. 4.4) applying a χ^2 minimisation procedure. The parabola reliably fits the tracks with minimum transverse momentum p_t of 50 MeV. The sequential

	sector number												
u	-	6	7	8	9	10	11	0	1	2	3	4	5
v	6	7	8	9	10	11	0	1	2	3	4	5	-

Table 4.1: Numbers of ϕ sectors of u and v modules used for the fitting of the parabolas in 2D pattern recognition.

numbers of u and v sectors included in the parabola reconstruction are shown in Tab. 4.1. There are two empty fields since the sectors are not adjacent. FST vertex, which is further used as a track selection criterion, is calculated from the parabolas.

Track Reconstruction

The parabolas obtained in 2D pattern recognition from two overlapping (u, v) sectors are combined together to determine hit space points. The pairs of (u, v) sectors for the parabola combination are shown in Tab. 4.2. A parabola combination where any of the obtained space points is outside the geometric acceptance of the sensor is excluded. The obtained space points are fitted by track parameters. The tracks are sorted according to the following criteria:

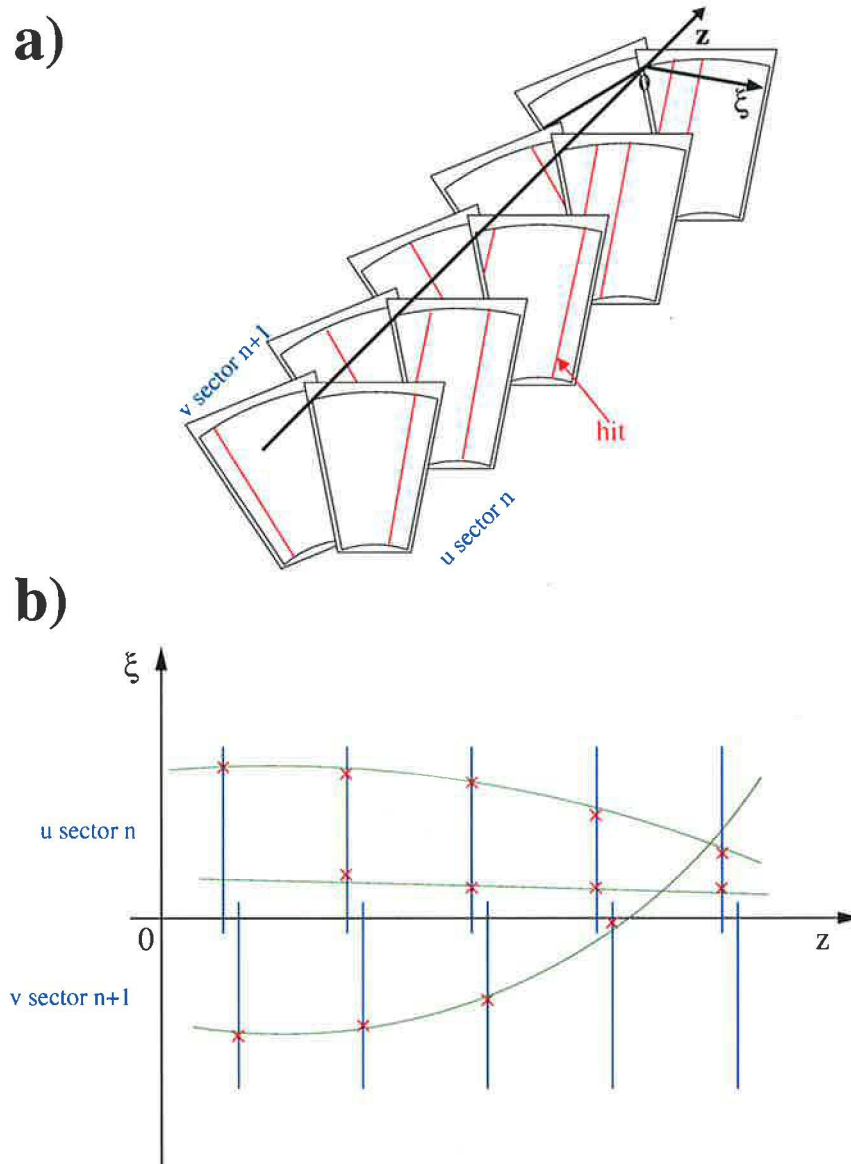


Figure 4.4: Schematically depicted u and v sensors in neighbouring sectors for the 2D pattern recognition. a) 3D view of hits. b) ξ, z projection with the parabolas.

- i) **Number of hits:** The tracks with the highest number of hits are of the highest priority.

	ϕ -sector number											
u,v	-,6	6,7	7,8	8,9	9,10	10,11	11,0	0,1	1,2	2,3	3,4	4,5
u,v	6,7	7,8	8,9	9,10	10,11	11,0	0,1	1,2	2,3	3,4	4,5	5,-

Table 4.2: Pairs of (u,v) sectors parabolas of which are combined to form tracks.

- ii) **Vertex pointing:** If the track points to the parabola fitted vertex it is preferred to the non vertex pointing track.
- iii) χ^2 : Sorting of the tracks according to χ^2 of the fit. ($\chi^2 < 3.5$ is required.)

The points and parabolas of the best track are excluded from the other tracks. The procedure of combining parabolas and selection are repeated until there remains at least one track with minimum number of hits required for fitting the helix.

Alignment

The position of every detector module can differ from its nominal position. The alignment parameters must be applied to correct the hit position for the shifts and rotations of every detector module in space. There is a set of parameters for each module: $(\Delta z_0, \Delta \xi_0, \Psi_\xi, \Psi_\zeta, \Psi_z)$.

The Δz_0 denotes the correction to the nominal z -position of the sensor and $\Delta \xi_0$ adjusts for the shift in measured coordinate ξ . They are used in both steps of the tracking for correcting the position of the hit.

The rotation angles $\Psi_\xi, \Psi_\zeta, \Psi_z$ are used only in the 3D reconstruction of tracks (subscripts denote the rotation axis). They are applied to correct the rotation of the module. Subscript ξ denotes the axes of the coordinate measured by the module, ζ is used for the axes defined by the direction parallel to the strips of the sensor and z stands for z -axis of the H1 coordinating system.

Track Parameters

The movement of the charged particle in the magnetic field is described by a helix curve with axis parallel to the magnetic field. The trajectory projection into the plane perpendicular to the helix axis forms a circle. Neglecting

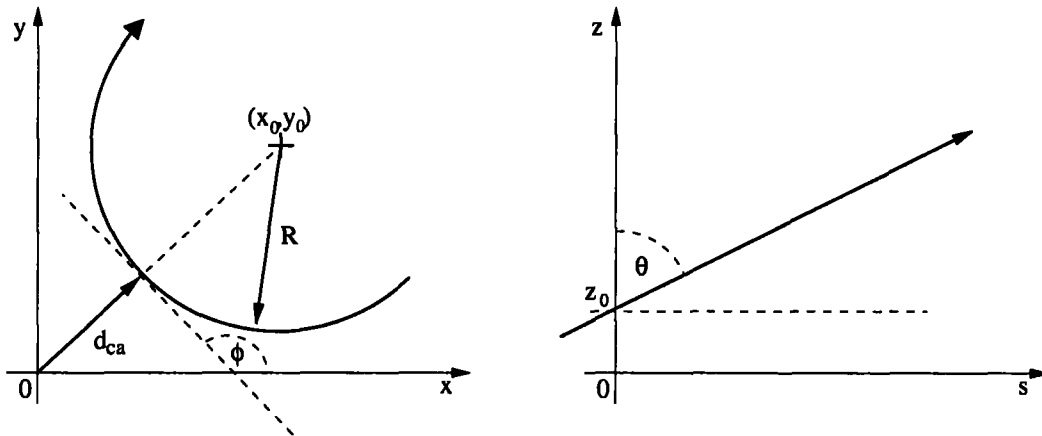


Figure 4.5: Schematically depicted the helix trajectory in x, y and s, z plane with the helix parameters.

the inhomogeneities and multiple scattering the helix description of particle track can be applied in H1 experiment. Since the magnetic field is parallel to the z -axis the circle trajectory is formed in the x, y plane. The natural parametrisation by the circle center and the radius is unfavourable in this case. Since the radius of high momentum particle is large it is difficult to determine the center point of the circle. A set of parameters $(\kappa, d_{ca}, \phi, \theta, z_0)$ is chosen to describe the track (see Fig. 4.5).

κ Curvature $\pm 1/R$ signed inverse radius. The $\kappa > 0$ if the trajectory turns counter clockwise and $\kappa < 0$ if clockwise in x, y plane. In the H1 coordinate system, where magnetic field is oriented in positive z -direction, a positive particle has negative curvature and vice versa.

d_{ca} Signed distance of the closest point of the trajectory to the origin. The sign is positive if the origin is situated left from the trajectory.

ϕ Azimuthal angle. An angle between x -axis and tangent to the circle at d_{ca} point.

θ Polar angle. An angle between tangent to the trajectory and z -axis at d_{ca} point.

z_0 z -coordinate at d_{ca} point.

Any point on the trajectory is calculated as follows:

$$x(s) = x_0 + 1/\kappa \sin \phi + \kappa s \quad (4.11)$$

$$y(s) = y_0 - 1/\kappa \cos \phi + \kappa s \quad (4.12)$$

$$z(s) = z_0 + s \cdot \cot \theta \quad (4.13)$$

where s denotes the length of arc in x, y plane from the d_{ca} point and x_0, y_0 are the coordinates of the center of the circle (see Fig. 4.5).

$$x_0 = -(1/\kappa - d_{ca}) \sin \phi \quad (4.14)$$

$$y_0 = (1/\kappa - d_{ca}) \cos \phi \quad (4.15)$$

As it can be seen from the relation 4.13 one of the advantages of this parametrisation is the straight line propagation of the trajectory in (s, z) plane which is depending only on the angle θ .

The momentum $\vec{p}(p_x, p_y, p_z)$ of the charged particle can be calculated using the track parameters:

$$p_t[\text{GeV}] = \sqrt{p_x^2 + p_y^2} = 3 \cdot 10^{-3} \frac{Z \cdot B[\text{T}]}{|\kappa[\text{cm}^{-1}]|} \quad (4.16)$$

$$p_x = p_t \cdot \cos \phi \quad (4.17)$$

$$p_y = p_t \cdot \sin \phi \quad (4.18)$$

$$p_z = p_t \cdot \tan \theta \quad (4.19)$$

$$p = \sqrt{p_x^2 + p_y^2 + p_z^2} = p_t / \sin \theta \quad (4.20)$$

where B is the magnetic field, Z denotes the charge of the particle in elementary charge units and p_t stands for the transverse momentum.

4.1.4 Distribution of Track Parameters

Most of the track parameters are distributed according to the FST geometrical acceptance which can be estimated from Tab. 3.1.

θ Range

The θ range of FST tracks with at least 5 hits is estimated to be $7.8^\circ < \theta < 15.9^\circ$ which follows from the layout parameters (see Tab. 3.1). The angular acceptance of the FST extends towards lower and higher values because the z coordinate of the nominal primary vertex has a Gaussian distribution with

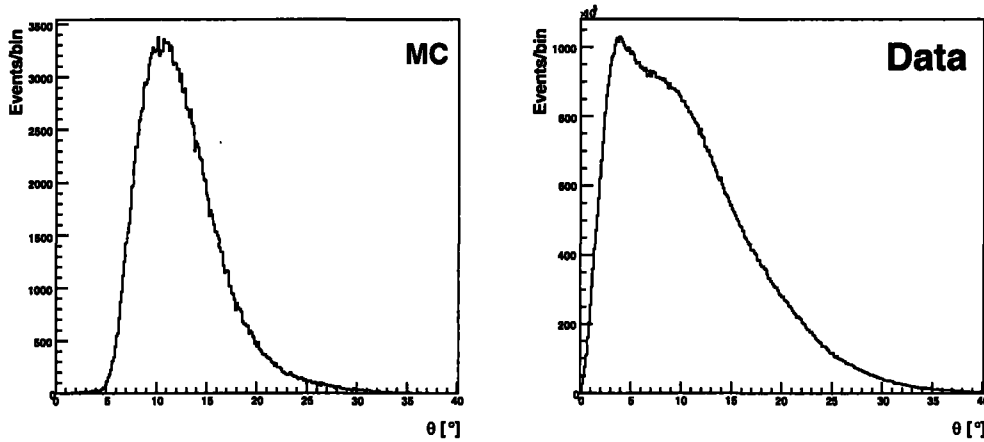


Figure 4.6: Distributions of the polar angle θ of FST tracks. Left: MC simulation, right: experimental data.

$3 \cdot \sigma = 35$ cm. The lower limit 4.3° is determined from tracks originating from the vertex at $z = -35.0$ cm and the upper limit of 41° is given by the distance of the discs since at $z = 35.0$ cm the vertex is inside the FST. The real range of the angle θ is smaller because of the helix trajectories of the charged particles. This is seen in Fig. 4.6, where the distribution of the angles θ of the simulated events is plotted. The data distribution significantly differs from the MC distribution since the simulation does not include background which is contained in the data. Therefore a lot of tracks detected in the FST comes from background events too. The reasonable θ range for the non background particle track reconstructed by the FST is $5^\circ < \theta < 35^\circ$.

ϕ Range

Empty sectors of the FST limit the geometrical acceptance of $|\phi| < 135^\circ$. It is visible in MC distribution of the ϕ parameter of FST tracks (see Fig. 4.7). The distribution is not homogeneous since the interaction vertex of the e^+p is misplaced from the reference point of the H1 coordinate system to $(x, y) = (0.3, 0.65)$. The difference between the data and MC distribution is caused again by the background events which originate farther from the interaction region.

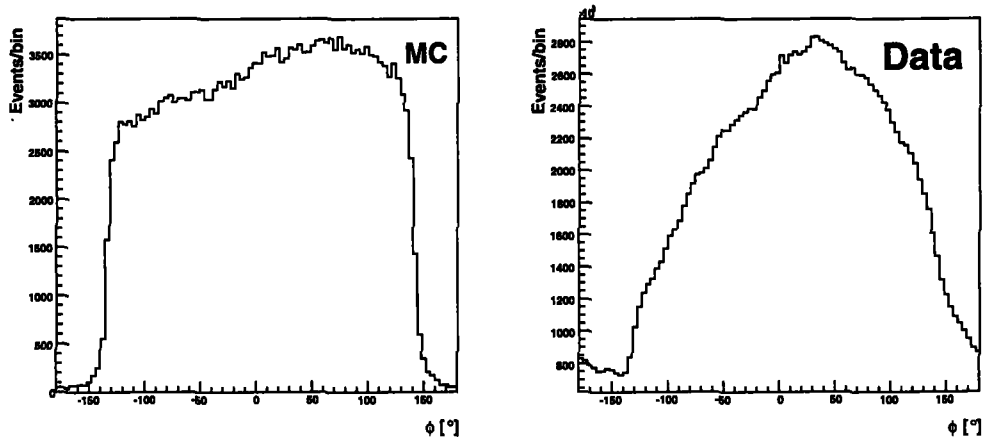


Figure 4.7: Distributions of the azimuthal angle ϕ of the FST tracks.

z_0 Range

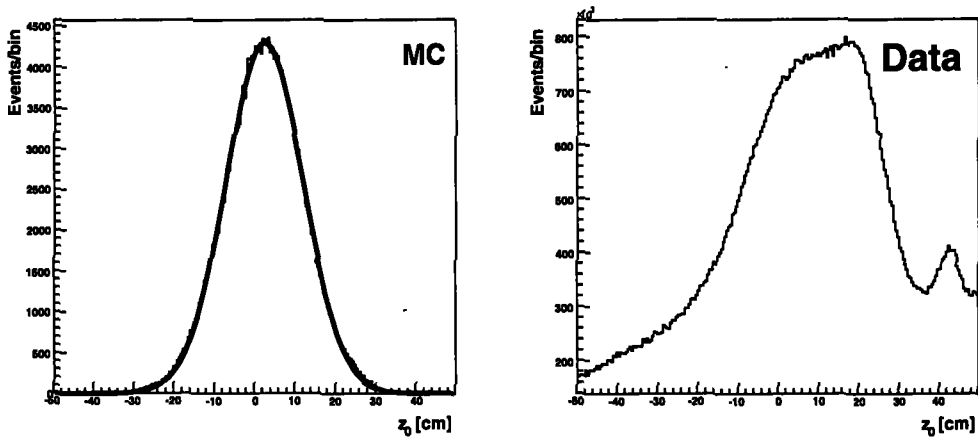


Figure 4.8: Distributions of the track parameter z_0 .

The distribution of z coordinate of the primary vertex is reflected in the z_0 parameter distribution (see Fig. 4.8). Whereas in the MC simulation particles come mainly from the interaction vertex only the data includes background induced charge particles too which are produced in beam gas

and beam wall interactions. A weak cut of $|z_0| < 35$ cm can be introduced to suppress some background.

d_{ca} Range

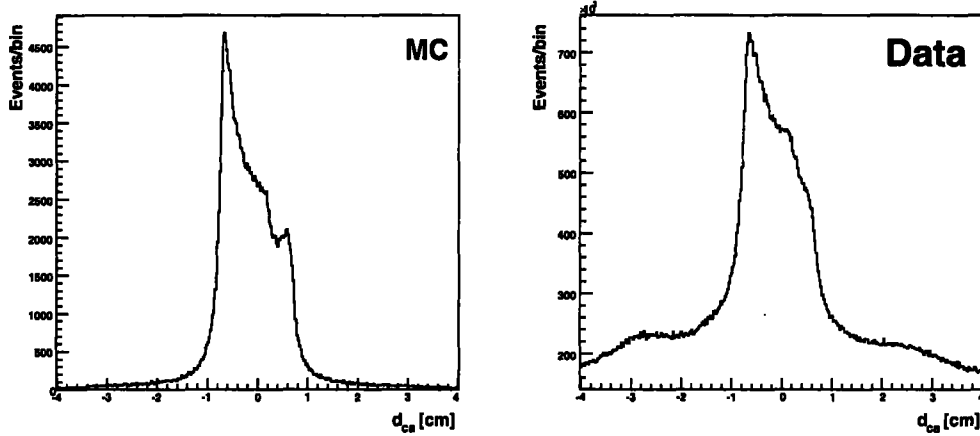


Figure 4.9: Distribution of the parameter d_{ca} of the FST track.

The distribution of the parameter d_{ca} shown in Fig. 4.9 does not peak at 0 because of misplacement of the e^+p interaction vertex. The data extends to the higher values of the $|d_{ca}|$ since the origin of the background events can be far away from the nominal vertex.

κ Range

The distribution of the curvatures κ (Fig. 4.10) depend on the momentum of the particles and their charges. The minimal value of $|\kappa|$ is limited by the resolution. No cut can be applied to suppress the background without losing part of the physics signal.

4.2 Detector Response

The implicit resolution of the measured coordinates is given by the equation 3.2. Better resolution can be achieved using the amplitudes of the signals in the calculation of hits relative positions according to the equation 4.7. The

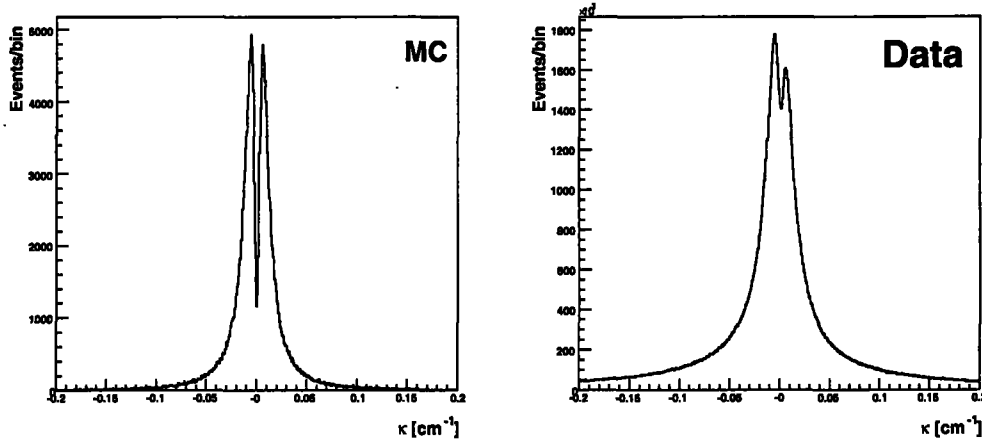


Figure 4.10: Distributions of the track parameter κ of the FST tracks.

resolution is dependent on the distance between two active strips and signal to noise (S/N) ratios of the strips.

4.2.1 Signal to Noise

The S/N ratios for the clusters, track fitted clusters and “golden” track fitted clusters are depicted in Fig. 4.11. The signal height of the cluster is calculated as a sum of hit amplitudes A_n and A_{n+1} of the strips n and $n + 1$ which form the cluster. The cluster noise is estimated as:

$$\Sigma = \sqrt{\Sigma_n^2 + \Sigma_{n+1}^2}. \quad (4.21)$$

“Golden” track means an FST track crossing all discs, i.e. with more than 8 hits, because it has the lowest possibility to be reconstructed with fake hits.

The distributions in Fig. 4.11 does not show very low S/N ratios since the hitfinder contains a minimal cut for the signal height (see relation 4.4). The signal is not accepted as a hit if it is smaller than octuple of the noise specific for the strip (see sec. 4.1.1). Despite this limit there still remains some noise accepted as a hit which is visible in the difference of the shape of the spectra of all clusters and track fitted clusters at the lower S/N values. On the other hand there still remain good hits with higher S/N which are not included in the track reconstruction for reasons of the track acceptance.

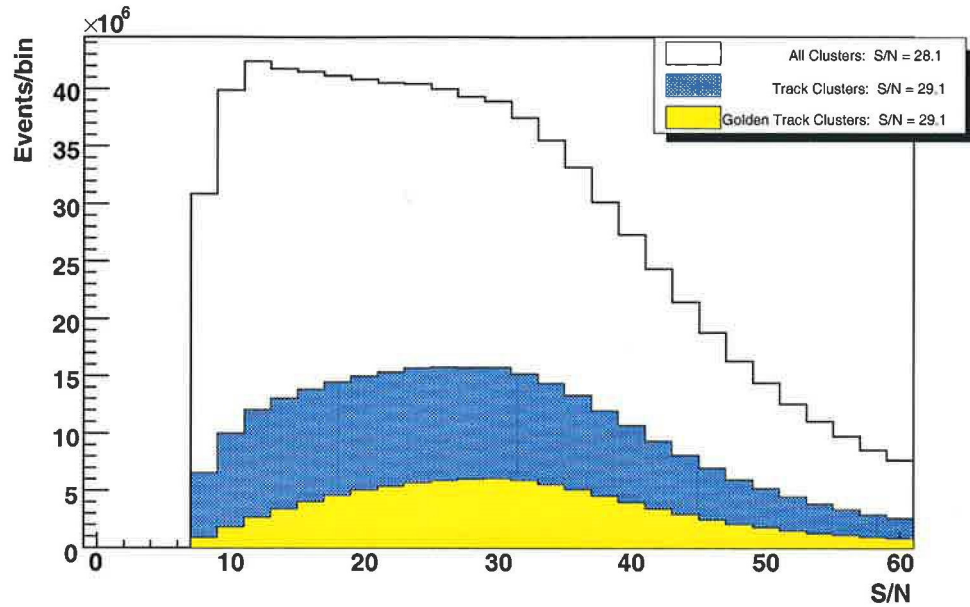


Figure 4.11: Distribution of the signal-to-noise-ratio for the raw and fitted hits.

The distributions of S/N ratios for several modules are shown in Figs. 4.12 and 4.13. Since all sensors were selected by a strict quality test (see [24]) their S/N distributions should not significantly differ. Despite that there is a dependence on the φ sector and z disc.

The φ -sector dependence is caused by the clock signals adjustment (see sec. 3.3.4) which is crucial for the S/N ratio. The modules in two neighbouring even and odd sectors are driven by the same clock signals. It is rather complex to meet all modules specific requirements within one sector. Although for some sensors the S/N ratios are smaller the whole sector¹ is working under reasonable conditions e.g. the sectors 10, 11.

The disc dependence of the S/N ratio is caused by the different temperature of the sensors. In several wheels the cooling was worse. For example the water flow around the disc 3 was blocked and therefore the S/N values are lower.

¹The whole sector means the same φ sectors in all discs.

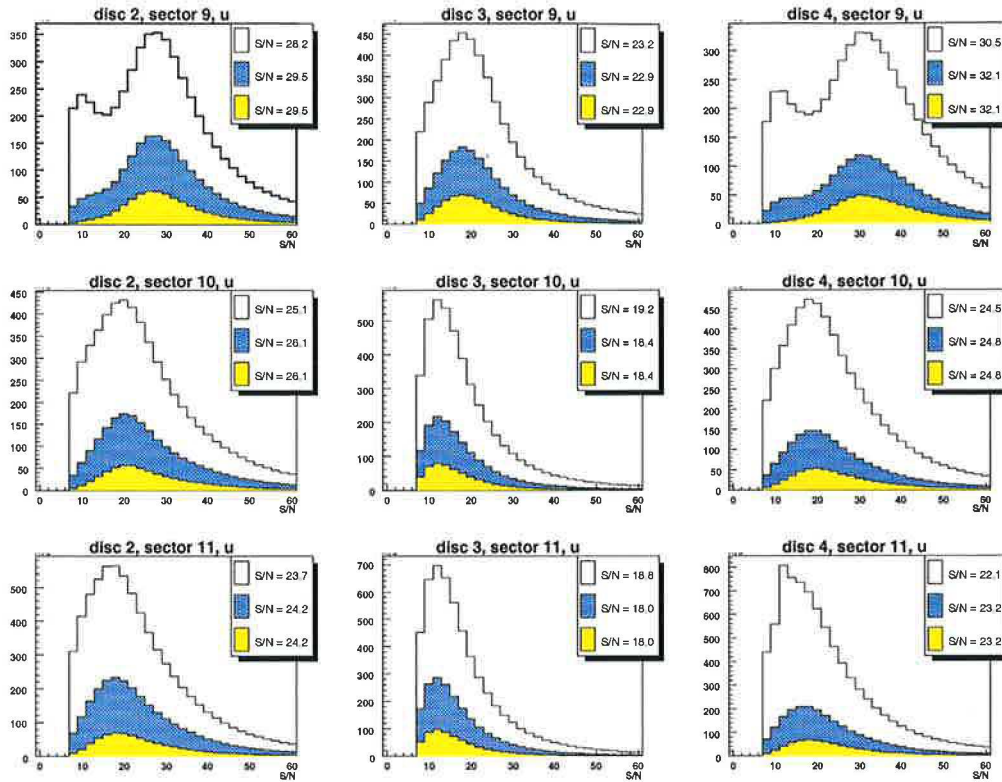


Figure 4.12: Distributions of the signal to noise ratios (S/N) for single modules of u -type in the discs 2,3,4 and sectors 9,10,11.

4.2.2 Hit Resolution

The hit resolution is determined from the residuals which are calculated as signed distances between the hits and the hit points estimated from the track projection². Tracks with more than 20 hits are used for the residual calculation which ensures usage of good tracks with minor influence of track-fit errors. The distribution of the weighted residuals is depicted in Fig. 4.14. The weight of a residual is calculated as:

$$w_{res} = \frac{N_{hits}}{N_{df}}, \quad (4.22)$$

²The track is projected into the z -coordinate of the hit.

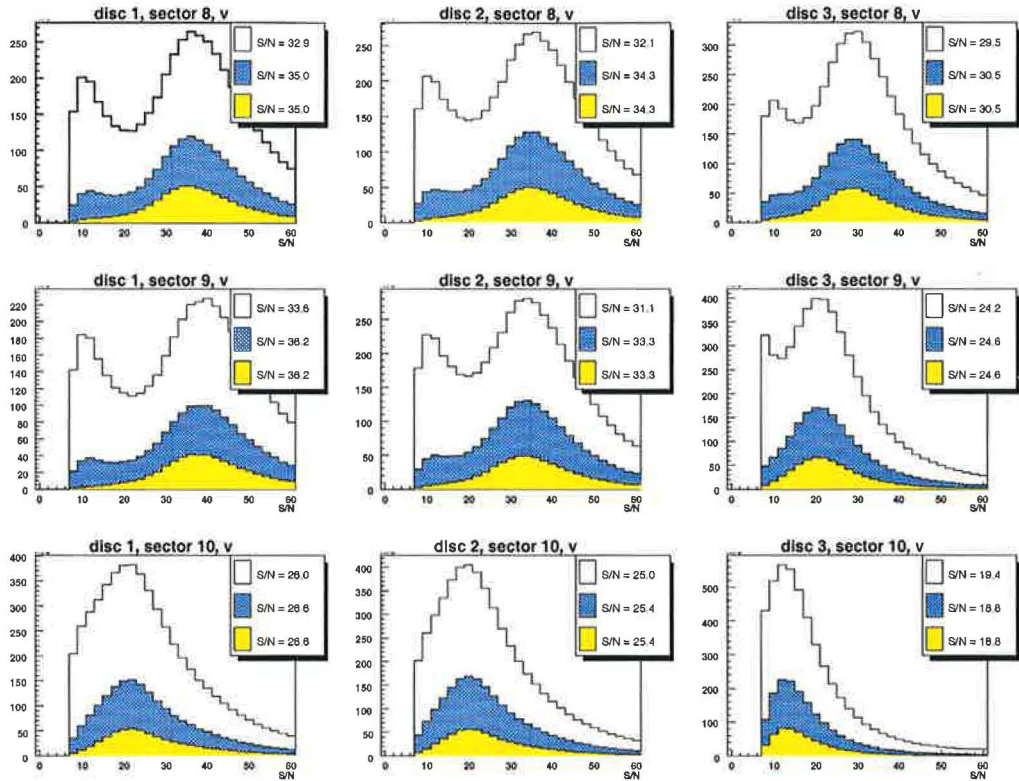


Figure 4.13: Distributions of the signal to noise ratios (S/N) for single modules of v -type in the discs 1,2,3 and sectors 8,9,10.

where N_{hits} is the number of hits included in the track fitting and N_{df} is the number of degrees of freedom of the fit. The average resolution in this calculation is $15.68 \mu\text{m}$. The resolution of the module is strongly dependent on the precision of the detector alignment. The best resolution of the module is twice better, i.e. $\sigma = 8.37 \mu\text{m}$. On the other hand the worst resolution of the single module reaches $20.14 \mu\text{m}$. Several single module distributions of the residuals with the resolutions around the average value are shown in Figs. 4.15 and 4.16.

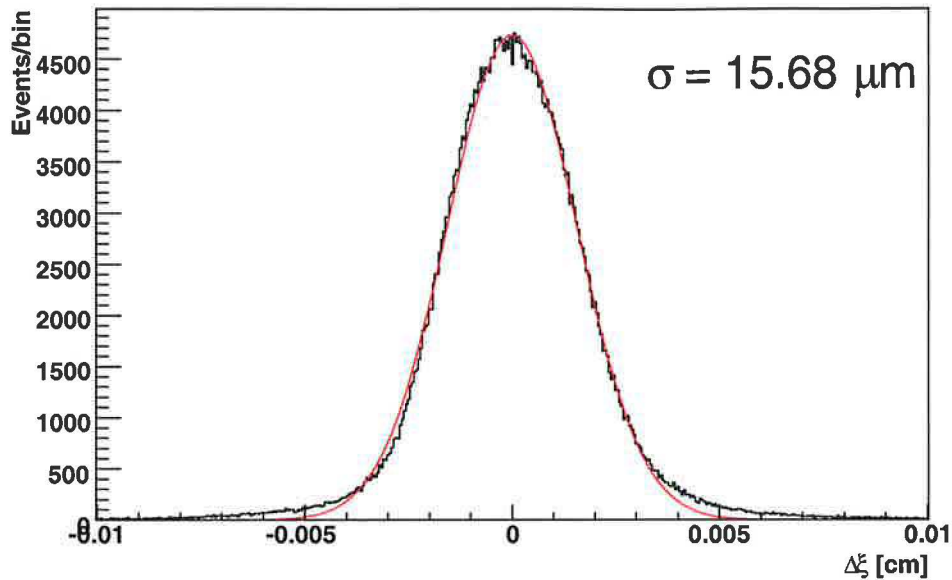


Figure 4.14: Distribution of the FST track residuals. The curve represents Gaussian fit with the width σ .

4.3 Occupancy

The occupancy is used mostly as immediate quality factor which characterises the status of the detector momentarily.

4.3.1 Strip Occupancy

The strip occupancy shown in Fig. 4.17 can be determined mostly online since the strip number is coded in the hit information. It serves as the first quality check for the adjustment of the detector. It must correspond to the length of the strip. It reveals the possible noisy and dead strips pointing to the inefficiencies and problems.

The distributions of the strip occupancy are depicted in Fig. 4.17. The distribution, which includes all hit clusters without any cuts, reflects the length of the strips and shows the pattern of 5 APC chips in readout. The strip numbering starts from the shortest strip. There are some spikes visible in the spectrum caused by fake hits from noisy strips. Within one APC

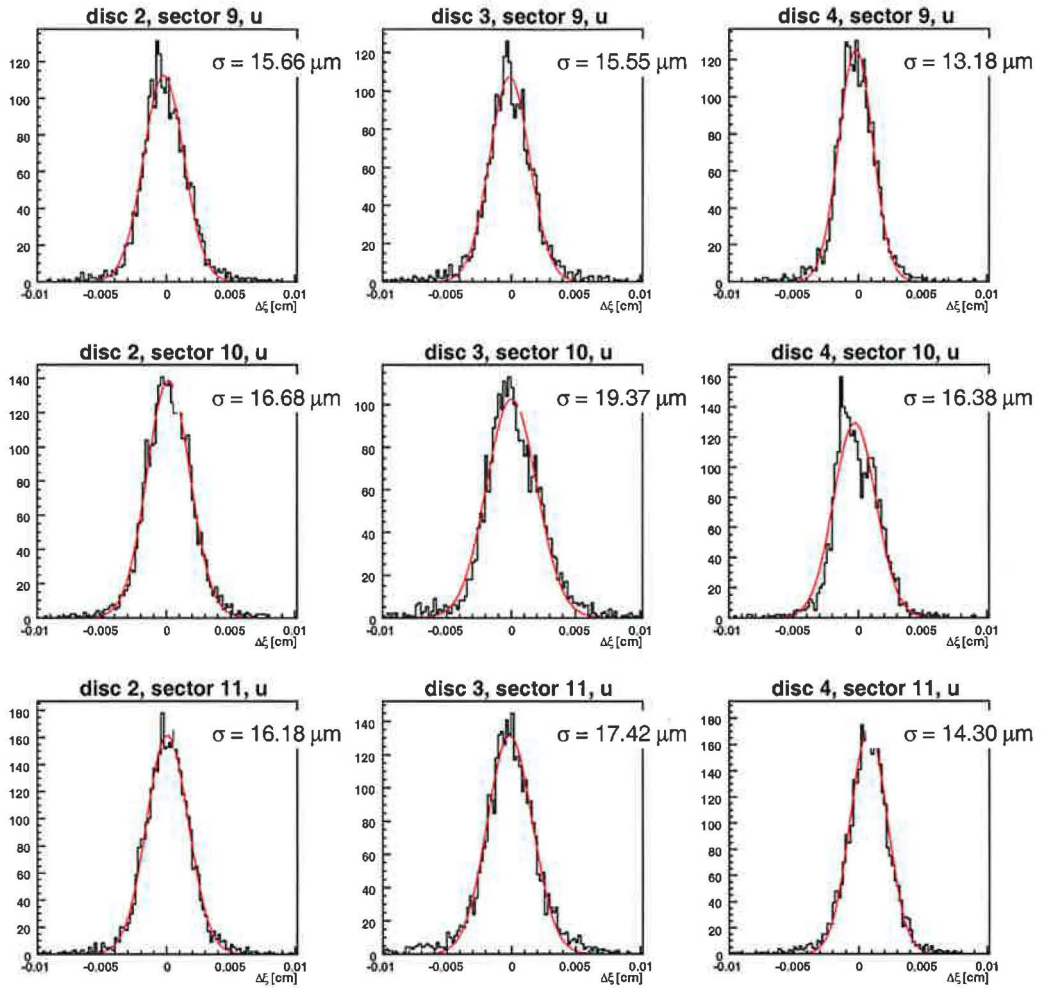


Figure 4.15: Distributions of the FST track residuals for single u modules in the discs 2,3,4 and sectors 9,10,11.

the occupancy slightly decreases up to the last channel of the APC which is caused by the chip readout properties. The noisy hits are suppressed when the strip occupancy is calculated for the track clusters with the fitted hits.

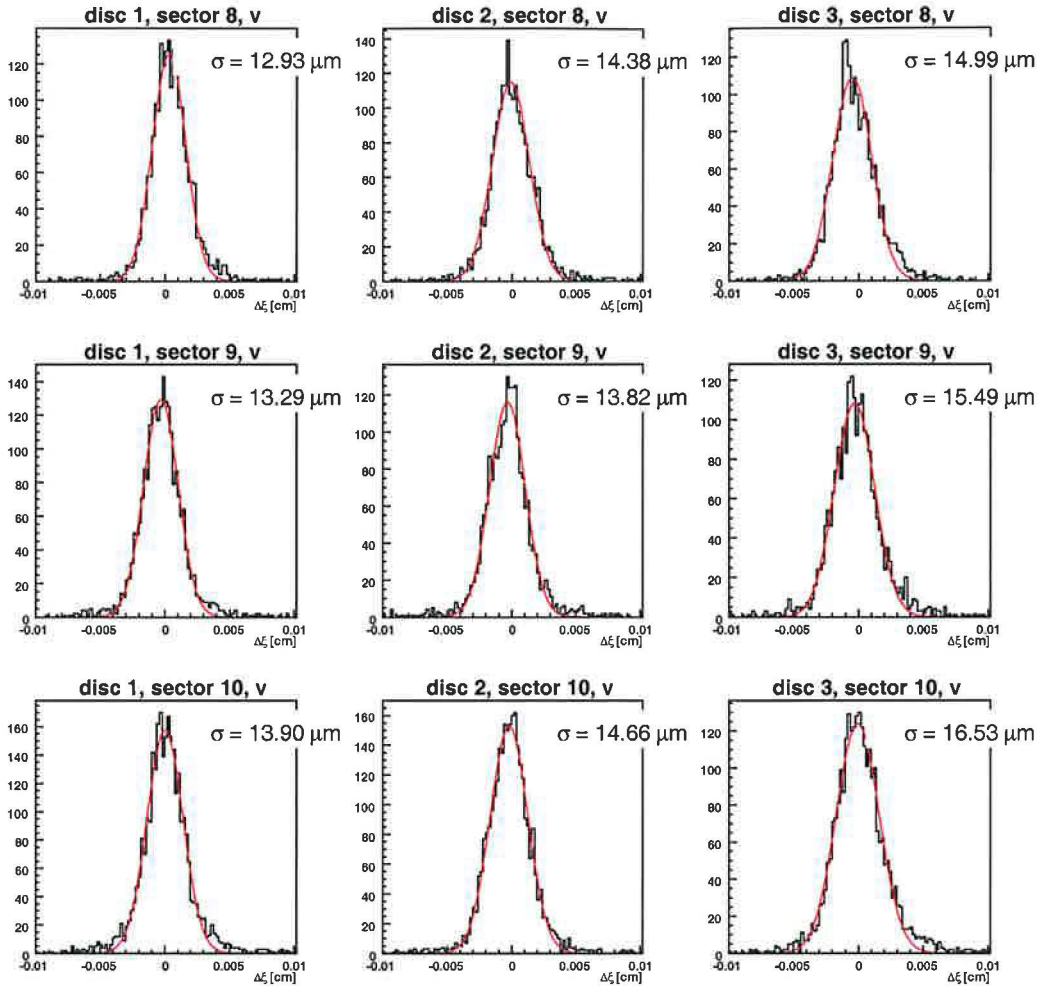


Figure 4.16: Distributions of the FST track residuals for single v modules in the discs 1,2,3 and sectors 8,9,10.

4.3.2 Module Occupancy

The spatial (x, y) occupancy of the reconstructed 3D hits from all tracks and using long tracks only are shown in Figs. 4.18 and 4.19 respectively. Missing u modules in disc 0 were not functional. The densities of points correspond to θ acceptance of the FST. Most of the hits are at lower radii in the discs closer to the vertex. The distribution maxima shift to the higher radii with the higher disc number.

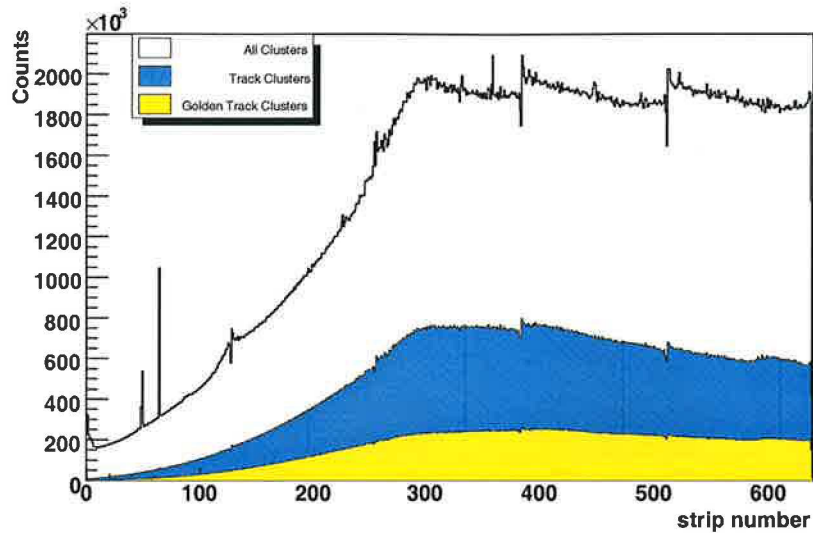


Figure 4.17: Strip occupancy. The strip numbering starts from the shortest strip (see Fig. 3.6).

The middle discs are more populated (see Fig. 4.18) because of the FST acceptance. The track must be reconstructed with at least 5 hits which means that some of the middle planes has to be crossed by the particle. The edges of the detectors are more populated because of the sensor overlaps.

The long tracks contain mostly reliable hits i.e. basically without fake hits (see Fig. 4.19). The density of the hits corresponds to the trapezoidal shape of the sensor. The global radial asymmetry of the density of the hits is caused by the misplacement of the nominal vertex. The population of long track hits within one sensor is more or less constant for a constant radius. On the other hand it is visible in Fig. 4.18 that some noise fake hits contribute and the middle of the sensor is preferred.

4.3.3 Pipeline Counter Occupancy

The occupancy of the pipeline counters (PIC) should be homogeneous over all data if the H1 trigger system does not prefer some pipeline. The occupancy of PIC exhibits homogeneous behaviour (see Fig. 4.20 a)). Distribution of average number of hits has to be independent on the PIC, but it shows significantly lower value around pipeline number 10 (see Fig. 4.20 b)). It is

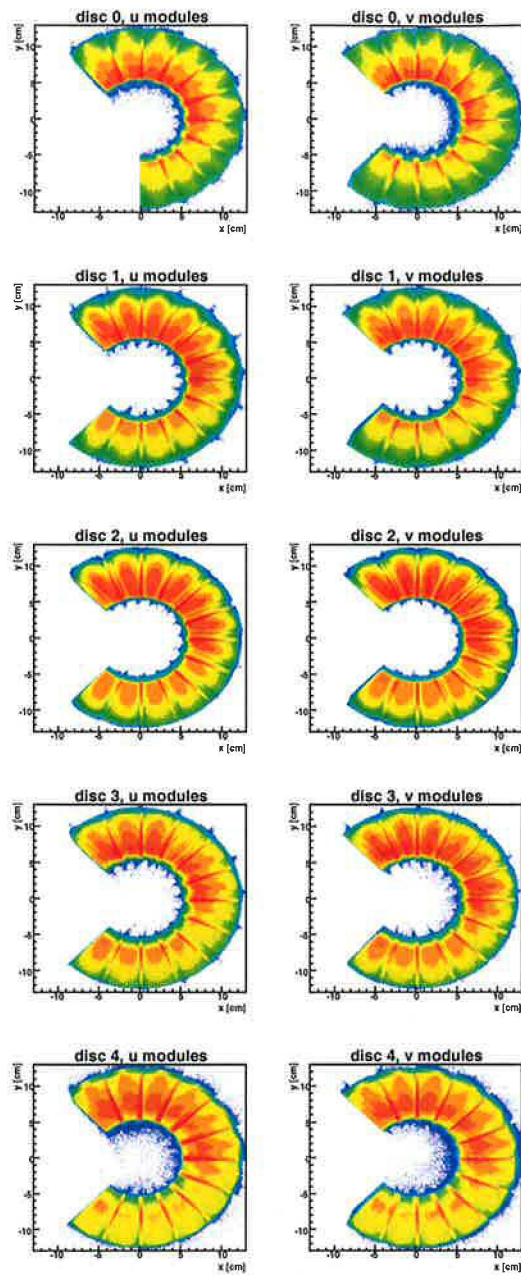


Figure 4.18: Occupancy of the FST reconstructed hits in the u and v modules for all discs.

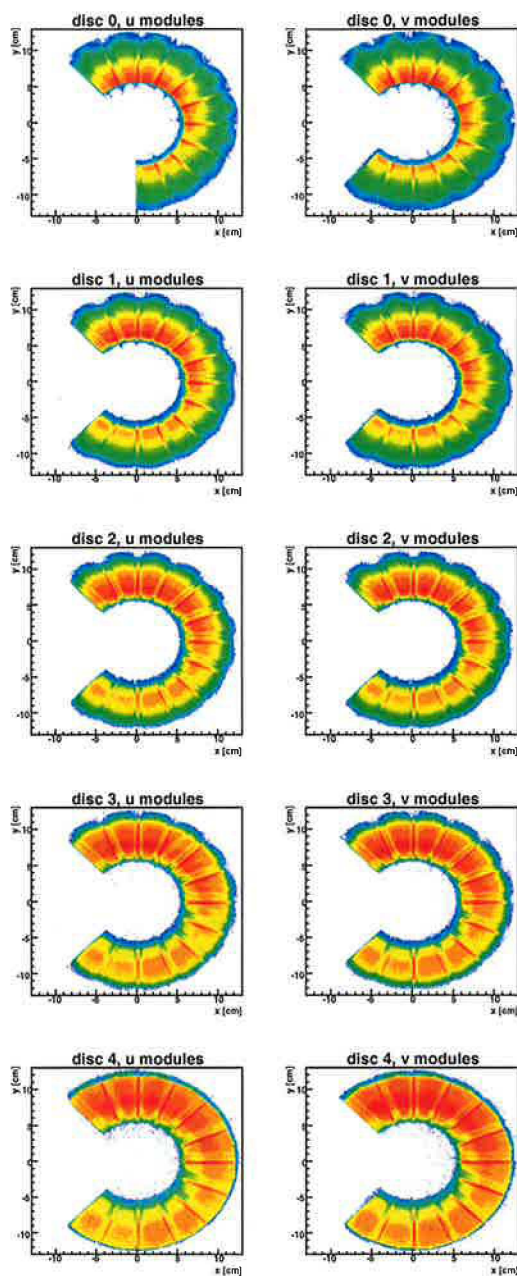


Figure 4.19: Occupancy of the FST reconstructed hits of long tracks in the u and v modules for all discs.

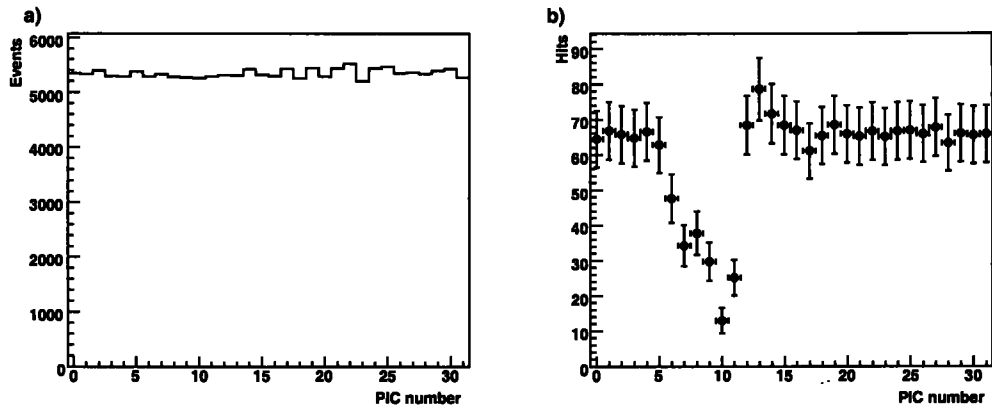


Figure 4.20: a) Pipeline counter (PIC) distribution b) Average number of hits per PIC.

caused by malfunctional hardware which drives the clock. Basically no track can be reconstructed in the event with PIC 10. The inefficiency caused by this effect is estimated to be $\approx 10\%$.

4.3.4 FST Internal Efficiency

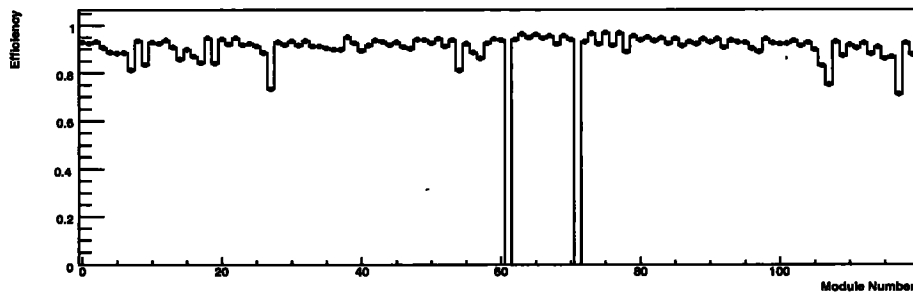


Figure 4.21: FST internal efficiency of the modules.

The efficiency of the module is calculated as a ratio of the module hit points used for the track reconstruction and intercept points of the tracks and active area of module. The points and hit points within the sensor in distance 0.5 cm from the sensor border are taken into account only to avoid uncertainties and efficiency loss caused by the sensor misalignment and error

of the intercept point. The internal efficiency of the modules is depicted in Fig. 4.21. Most of the sensors has the efficiency over 90% except the dead or problematic detector modules.

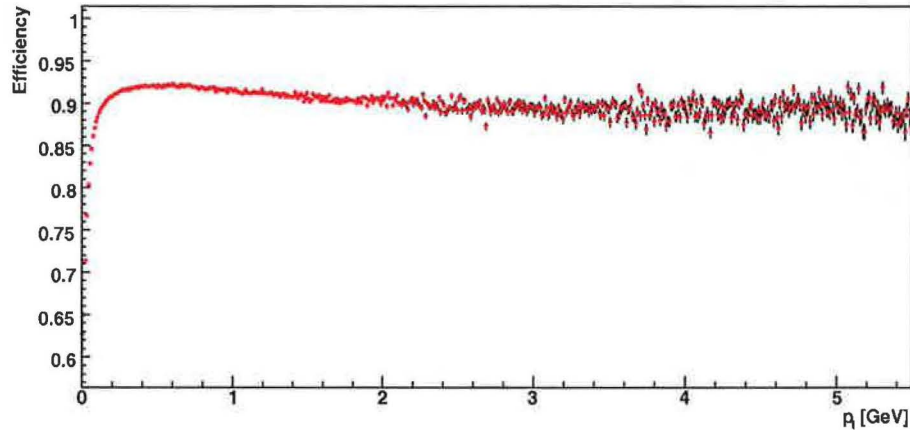


Figure 4.22: FST internal efficiency vs. reconstructed transverse momentum.

Dependence of the efficiency on the reconstructed transverse momentum depicted in Fig. 4.22 shows the efficiency drop towards the lower p_t values.

4.4 Momentum Resolution

The momentum of the particle is determined from the track parameters (see equations 4.16, 4.17, 4.18, 4.19 and 4.20). The transverse p_t and absolute momenta p are functions of the curvature κ and the polar angle θ only. The resolutions of polar angle θ and transverse momenta p_t have been studied.

4.4.1 Theta Resolution

The reconstruction precision of the angle θ depends on the resolution of the measured coordinates. Moreover the multiple scattering (MS) can cause the change of the helix curve. The distribution of (MS) deflection angles can be approximated by a Gaussian function with the width given by the formula

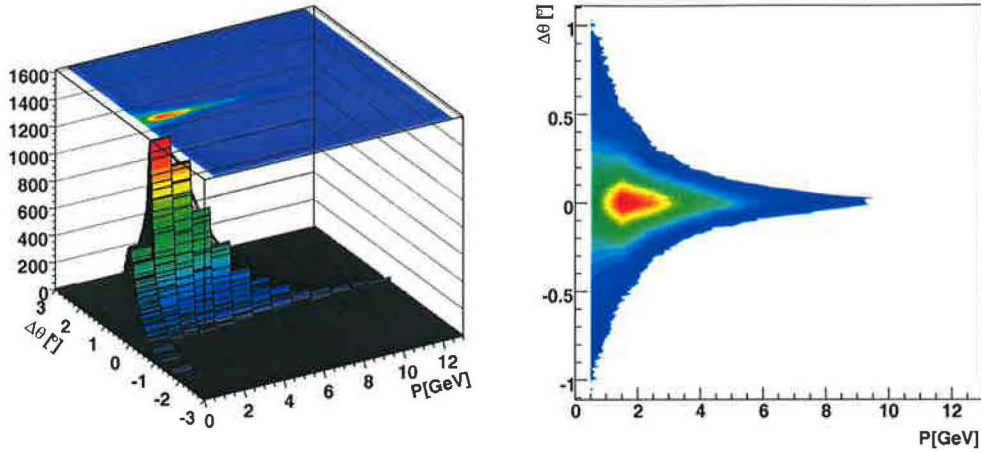


Figure 4.23: $\Delta\theta$ dependence on the generated momentum p .

[25]

$$\sigma_{MS} = \frac{13.6 \text{ MeV}}{p\beta c} Z \sqrt{x/X_0} [1 + 0.038 \ln x/X_0], \quad (4.23)$$

where p , βc and Z are the momentum, velocity and the charge (in elementary charge units) of the particle and x/X_0 is the thickness of the material in the radiation lengths X_0 . The radiation length of the silicon material is 9.36 cm. A pion with the momentum of 1 GeV passing all ten layers of the FST would have a distribution of the angular deflections with the width of 0.02° .

The dependence of the difference $\Delta\theta = \theta_{gen} - \theta_{rec}$ of the particle generated angle θ_{gen} and the reconstructed angle θ_{rec} on the generated particle momentum p is depicted in the Fig. 4.23. The width of this difference is obviously bigger than the expected one because the particle passes more material in front of the FST³.

4.4.2 Transverse Momentum Resolution

The precision of the reconstruction of the transverse momentum p_t is related to the precision of the curvature κ of the track. The resolution of the

³Beryllium beampipe, CST end flange with housed electronics etc.

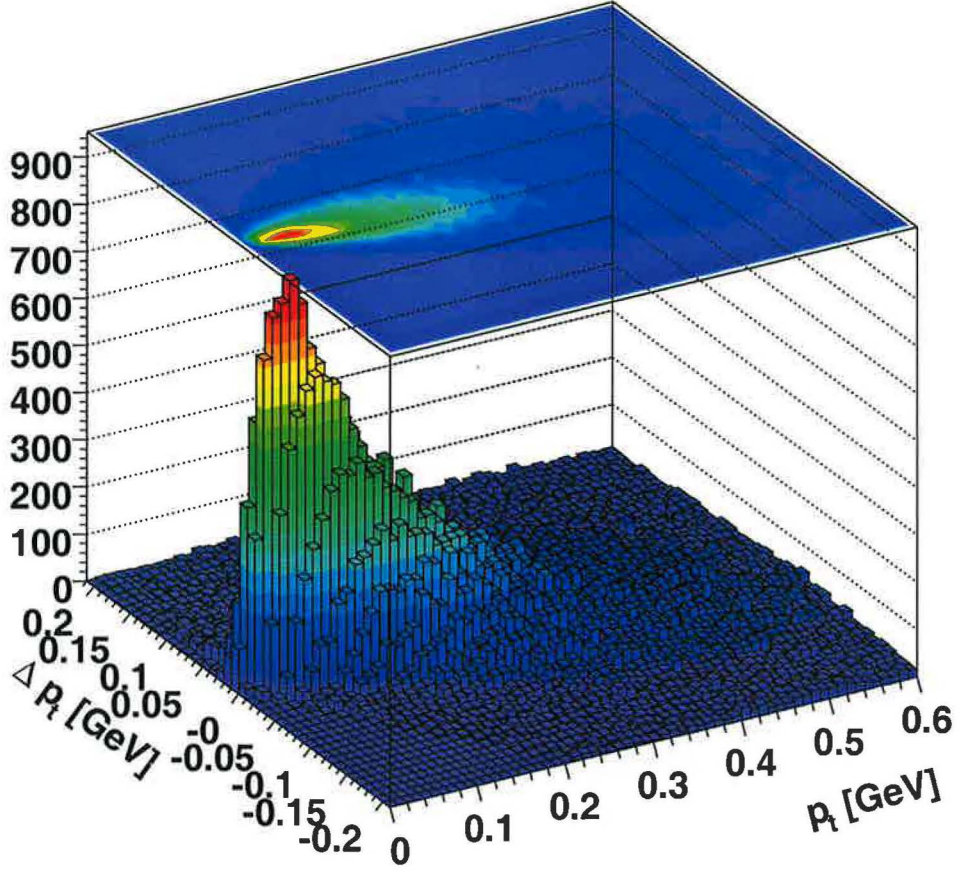


Figure 4.24: Scatter plot of Δp_t vs. p_t .

transverse momenta can be determined from equation 4.16

$$\frac{\delta p_t}{p_t} = \frac{\delta \kappa [\text{m}^{-1}]}{0.3 \cdot Z \cdot B} \cdot p_t, \quad (4.24)$$

where $\delta \kappa$ is the error of the track curvature. In ideal case the $\delta \kappa$ is given only by the curvature error $\delta \kappa_{res}$ due to finite measurement resolution [25]

$$\delta \kappa_{res} = \frac{\epsilon}{L'^2} \sqrt{\frac{720}{N+4}}, \quad (4.25)$$

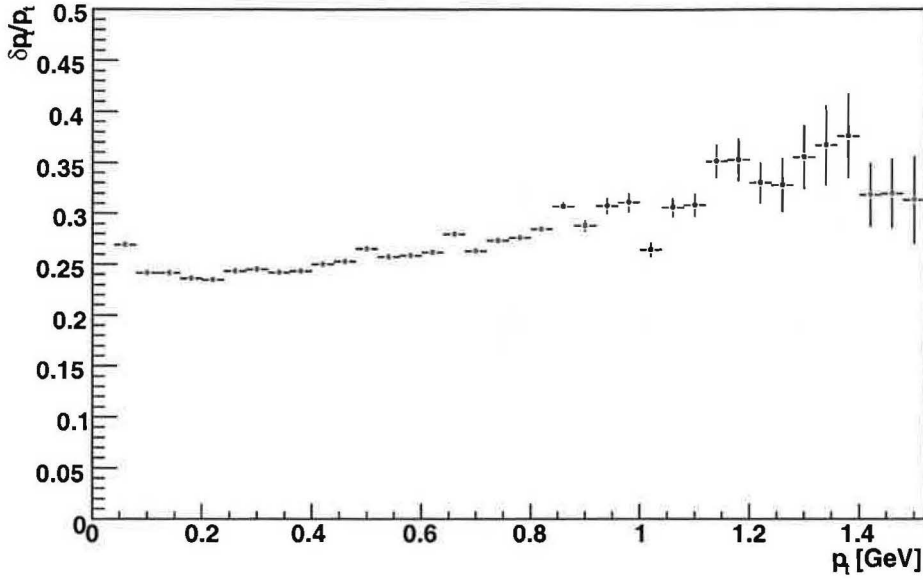


Figure 4.25: Resolution $\delta p_t/p_t$ as a function of p_t .

where N (≥ 10) is the number of uniformly spaced positions used for fitting of the helix, ϵ is a measurement error which is supposed to be constant in every point and L' denotes the length of the track arc. The contribution $\delta\kappa_{MS}$ of the multiple scattering to the curvature error must be taken into account

$$\delta\kappa_{MS} \approx \frac{(0.016)(\text{GeV}/c)Z}{Lp\beta \cos^2 \lambda} \sqrt{\frac{L}{X_0}}, \quad (4.26)$$

where L and X_0 are the total length of the track and radiation length of the scattering medium respectively. Variable λ denotes the pitch angle ($p \cos \lambda = p_t$).

The difference Δp_t and $\delta p_t/p_t$ ratio are shown in Fig. 4.24 and 4.25 as a function of p_t . The points in Fig. 4.25 are obtained as σ of a Gaussian fit for every p_t bin of the plot in Fig. 4.24. The $\delta p_t/p_t$ ratio is rather high starting at 25% and reaches up to 35%.

Chapter 5

D^* Reconstruction with the FST

D^* meson production was investigated in recent years by the H1 and Zeus collaborations at HERA (see [7], [8], [9], [10]). In all the publications the central tracks were used for the determination of the D^* signal which gives the limitation to the pseudorapidity of $|\eta^{D^*}| < 1.5$. In this chapter the detection of the D^* meson by means of the FST will be described mainly using the Monte Carlo simulation.

The theoretical predictions indicate decrease of the cross section with the higher D^* pseudorapidity. Additionally, the acceptance range of the FST is rather narrow. Therefore the number of D^* mesons detected by means of the FST is expected to be lower than the number of D^* mesons detected in central region. Moreover the combinatorial background will increase due to the contribution of the forward jets. Similarly the imprecision of the particle momentum determined by the FST will smear out the D^* signal which will decrease with respect to the combinatorial background.

The analysis of the D^* production has been done within the H1OO framework. It is an object oriented framework with the algorithms and the data organised in classes, based on ROOT package and implemented in C++. The data is organised in a three-layer structure, each layer corresponds to a different ROOT tree. The uppermost layer, HAT, contains event level information for fast selection of events e.g. Q^2 , y etc. The particle four-vector informations are stored in the middle layer, mODS. The lowest layer, ODS, contains the reconstruction output e.g. reconstructed tracks, clusters etc. All three layers are used in this analysis.

5.1 D^* Meson Properties

The D^* meson decays in various ways. The decay with minimum number of charged particles in the final state proceeds in the following way

$$D^{*\pm} \rightarrow D^0 + \pi_{slow}^{\pm} \quad (5.1)$$

$$D^0 \rightarrow \pi^{\pm} + K^{\mp} \quad (5.2)$$

Since the branching ratios of D^* and D^0 are $67.7 \pm 0.5\%$ and $3.80 \pm 0.09\%$ [25], respectively, the branching ratio of the $D^{*\pm} \rightarrow \pi_{slow}^{\pm} + \pi^{\pm} + K^{\mp}$ is equal to $2.573 \pm 0.080\%$. Because the mass difference between D^* and D^0 is

$$m_{D^{*\pm}} = 2010.0 \pm 0.5 \text{ MeV}$$

$$m_{D^0} = 1864.6 \pm 0.5 \text{ MeV}$$

$$\Delta m = m_{D^{*+}} - m_{D^0} = 145.421 \pm 0.010 \text{ MeV}$$

$$m_{\pi^{\pm}} = 139.57018 \pm 0.00035 \text{ MeV}$$

$$m_{K^{\pm}} = 493.677 \pm 0.016 \text{ MeV}$$

Table 5.1: D^* and its decay product masses.

slightly above the π mass only small phase space is available for momenta of the secondary particles of the process 5.1. Therefore π in the decay 5.1 is called slow pion (π_{slow}). The momenta of D^0 and π_{slow} in the laboratory frame are determined mainly by the D^* momentum. Because the momentum phase space of D^0 decay products is large the momenta of K and π can reach higher values compared to the momenta of π_{slow} .

5.2 D^* Monte Carlo

MC simulation of deep inelastic scattering events was performed with RAP-GAP 2.8 Monte Carlo generator [26]. Generator parameters are summarised in Tab. 5.2. Neutral current deep inelastic scattering events with boson gluon fusion processes and with radiative corrections for the initial and final state were generated under HERA 2004 beam conditions. Peterson model was used for the fragmentation of c (\bar{c}) quark into D^{*+} (D^{*-}) mesons. Events with the D^* and D^0 meson decays 5.1 and 5.2 were accepted for further reprocessing by simulation and reconstruction programs. In total 121351 events corresponding to the luminosity 120 pb^{-1} were reconstructed and used for this analysis within the H1OO framework.

$p_z(p) = 920 \text{ GeV}$	initial proton momentum
$p_z(e^+) = -27.5 \text{ GeV}$	initial positron momentum
$e^+ + p \rightarrow e^+ + c + \bar{c} + X$	boson gluon fusion
Peterson fragmentation $\epsilon = 0.078$	fragmentation model
$m_c = 1.5 \text{ GeV}$	mass of charm quark
$Q^2 > 1 \text{ GeV}^2 \quad 0.01 < y < 0.99$	event kinematic selection
CTEQ5L (PDFLIB 1446)	proton structure function
SaSGAM	photon structure function
$\tau \geq 0.8 \cdot 10^{-8}$	particle decay disabled
$D^{*\pm} \rightarrow D^0 + \pi_{slow}^\pm \rightarrow K^\mp + \pi^\pm + \pi_{slow}^\pm$	event selection

Table 5.2: RAPGAP generator parameters.

5.2.1 D^* Signal Determination

The reconstruction of D^* mesons is based on the D^* four-momenta determination which is obtained from the four-momenta of their decay products. Three tracks with suitable charges are combined to calculate the D^* effective mass. No explicit particle identification is applied and each track is assumed to belong to either K or π as necessary. The meson K is assigned to the track with opposite charge of the D^* candidate. The other remaining tracks are supposed to be pions resulting in two possible D^* candidates. The effective mass of the K and π must lie within D^0 mass region which is specified below. The Δm tagging technique is applied [27]. Fit of Δm distribution provides a mean to determine the number of reconstructed D^* candidates. Since systematic imprecisions of reconstructed momenta partially cancel, the Δm peak is much narrower than the peak in the mass distribution of the D^* candidates.

5.2.2 Estimation of the FST D^* Acceptance

The FST has been build mainly to extend the acceptance for the detection of heavy quarks in the forward region of the H1 detector. Since the angular range of the FST is rather small the probability of the registration of the D^* decay products in the FST only is negligible. The D^* acceptance can be increased if the FST is combined with the FTD and CTD.

An FST D^* candidate must have at least one track reconstructed in the FST. Since the performance of FTD was very unstable in 2004 FTD tracks could not be used for the D^* identification. Therefore the FST tracks are

combined with a central fitted tracks only. A central fitted track is mainly a CJC reconstructed track with complementary hits from the CST, COZ, or CIP refitted to the reconstructed vertex.

The acceptance is calculated as a ratio of a number of reconstructed and generated D^* mesons. The reconstructed D^* meson is a D^* candidate formed by tracks coming from the generated particles originating from D^* and D^0 decays 5.1 and 5.2. No restrictions on kinematic variables of D^* candidates or their decay products were applied. It means that this is the most optimistic estimation of the acceptance.

If the FST tracks are included into the reconstruction of D^* mesons the polar angle range θ^{D^*} is extended toward the lower angles. Therefore the acceptance increases at higher values of D^* meson pseudorapidity η

$$\eta = -\ln \tan \frac{\theta}{2} \quad (5.3)$$

Similarly the FST D^* mesons contribute to the energy acceptance at higher values of D^* energies (see Fig. 5.1).

Furthermore the acceptance of the events with D^* mesons increases at higher Bjorken x values (Fig. 5.2). This effect could be expected since a D^* meson produced under smaller angle tends to have higher energy. Therefore the interacting parton should carry higher fraction of the proton momentum. The increase of the acceptance allows to determine the gluon density functions at higher x values.

The acceptance of the FST is roughly around 15% (see Fig. 5.1). The total number of reconstructed D^* mesons without any selections applied was 6300 which corresponds to the value of the cross section estimated from the results of the HVQDIS program in section 1.5.

5.2.3 Selections, Efficiencies and Purities Study

Various selections have to be applied to suppress the combinatorial background to achieve reasonable signal height without losing too much of D^* events. The impact of applied cuts on the efficiency and purity of the signal was studied with the aim to obtain clean signal distinguishable from combinatorial background.

The efficiency and purity are defined as follows

$$\epsilon(a) = \frac{N_{st}(a)}{N_t} \quad (5.4)$$

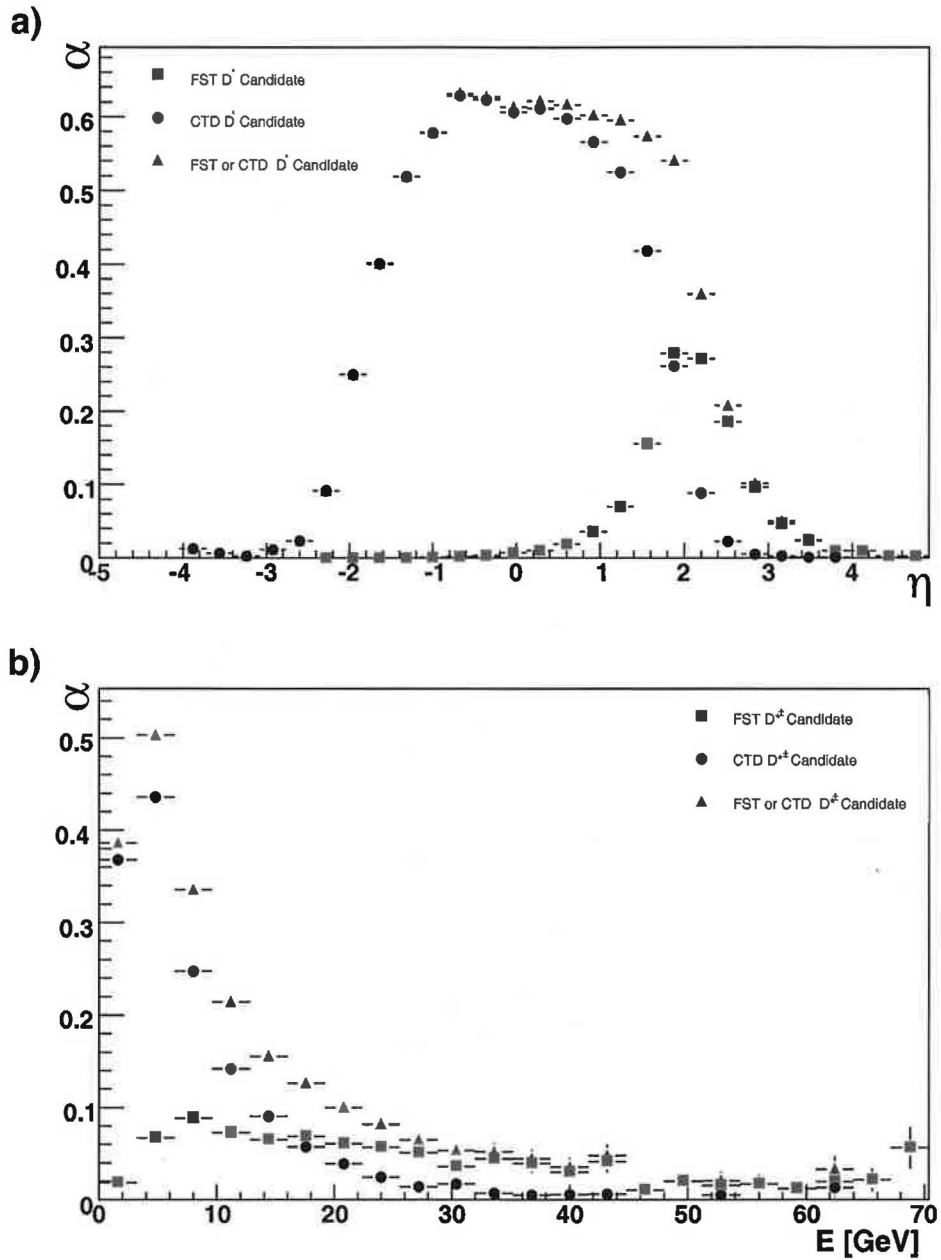


Figure 5.1: D^* acceptance α of CTD and FST as a function of a) pseudorapidity η and b) energy of reconstructed D^* mesons.

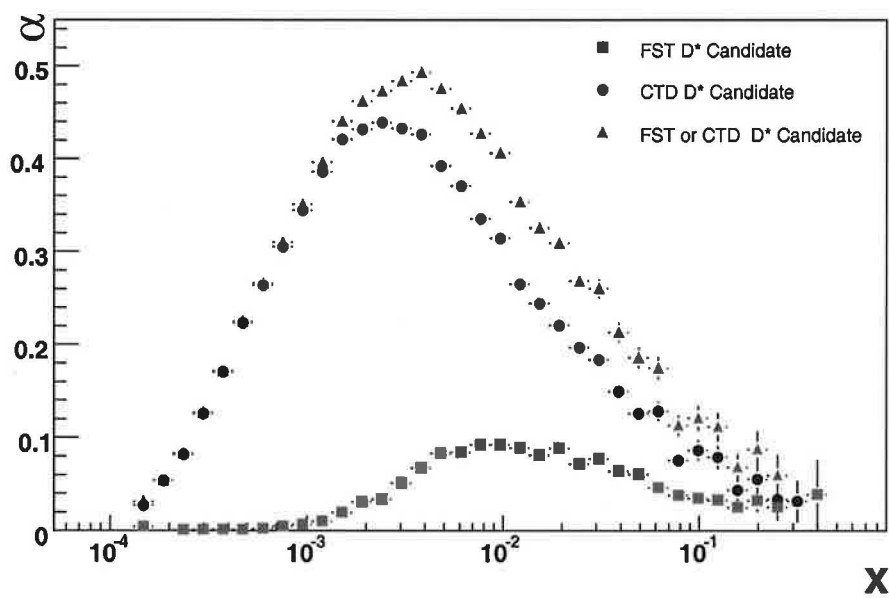


Figure 5.2: D^* acceptance α of the CTD and FST as a function of Bjorken x .

$$P(a) = \frac{N_{st}(a)}{N_s(a)} \quad (5.5)$$

where a is any variable used for the D^* selection. N_t is the number of reconstructed D^* mesons, N_{st} denotes the number of reconstructed D^* mesons accepted by selection criteria and N_s is the number of selected D^* candidates.

There can be distinguished four types of cuts:

- i) **Track selection:** Reliable and precise tracks are selected.
- ii) **Global event properties:** Event kinematic variable cuts, track multiplicities etc.
- iii) **Geometry cuts:** Reconstructed D^* and D^0 pseudorapidity.
- iv) **Kinematic restrictions:** Selection criteria on the momenta of D^* candidates and their decay products.

Candidate Geometry Cuts

A D^* candidate with a track in the FST has rather small polar angle θ i.e. it has high pseudorapidity η . The normalised distributions of η of all D^* candidates and of reconstructed D^* mesons are depicted in Fig. 5.3 a). The purity and efficiency dependence on the limit $\eta_{min} < \eta$ is shown in Figs. 5.3 c), e). It is obvious that choosing $\eta_{min} = 0$ the efficiency is high and the purity is slightly decreased from its maximum value. Similar conclusions are also valid for D^0 originating from the D^* decay (see Fig. 5.3).

Kinematic Restrictions

Kinematic restrictions are based on the comparison of various quantities and on the dependence of the efficiencies and purities on the kinematic limits. Normalised distributions of π_{slow} transverse momenta p_t are depicted in Fig. 5.4 a). There is a difference in the shape of the spectra towards the higher values. The effect of the lower limit p_t^{min} of the π_{slow} momentum on the efficiency and the purity is illustrated in Figs. 5.4 b), c). The D^* candidate is accepted only if the transverse momentum of π_{slow} is higher than p_t^{min} .

The efficiency decreases with higher p_t^{min} whereas the purity rises significantly. At higher values of p_t^{min} purity starts to be unstable because of small number of true and selected candidates.

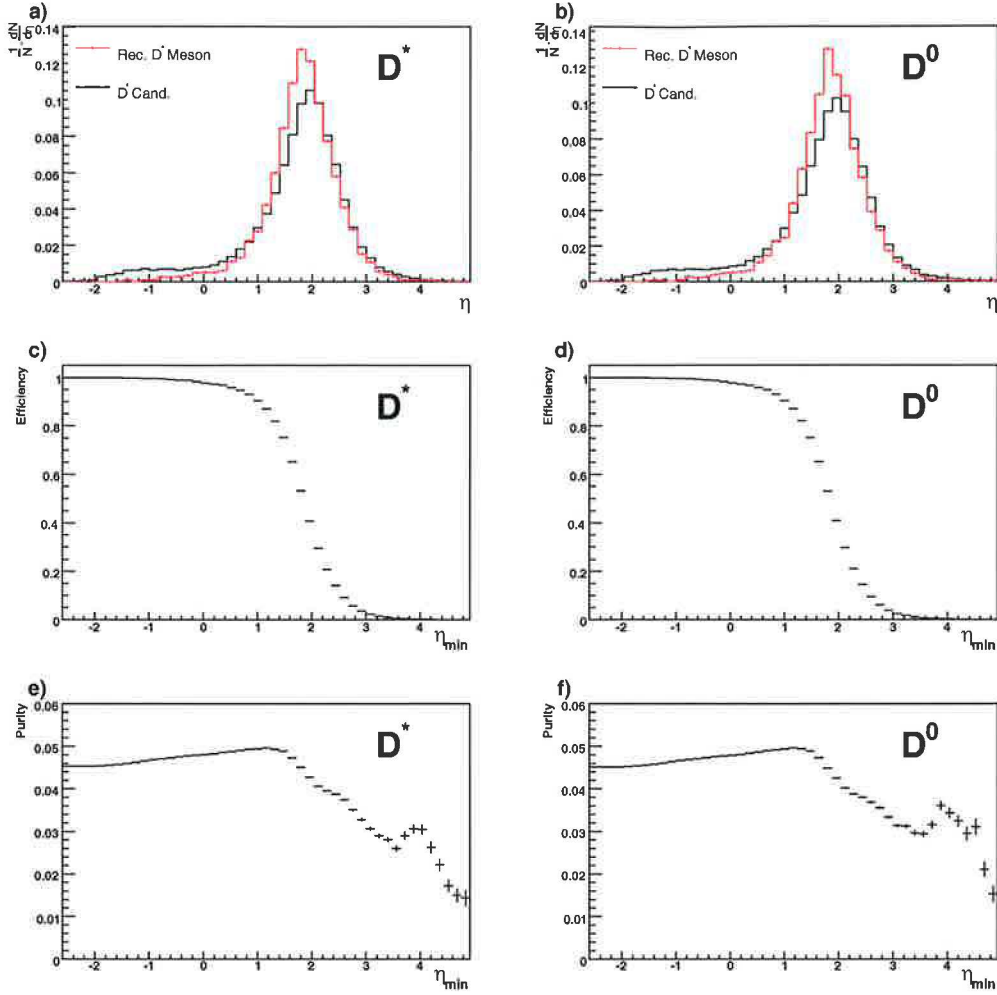


Figure 5.3: a), b) Normalised D^* , D^0 pseudorapidity distributions. c), d) Efficiency dependence on the lower limit of the pseudorapidity η_{min} . e), f) Purity dependence on η_{min} .

Similar conclusions are valid for the minimum value of the absolute momentum p^{min} (see Fig. 5.4). The purity rises with increase of p^{min} and the efficiency decreases.

The efficiency and purity dependence on the lower limit of the transverse and absolute momenta of π are shown in Fig. 5.5. The analogous plots for K meson minimal momenta are depicted in Fig. 5.6. The kinematic limits

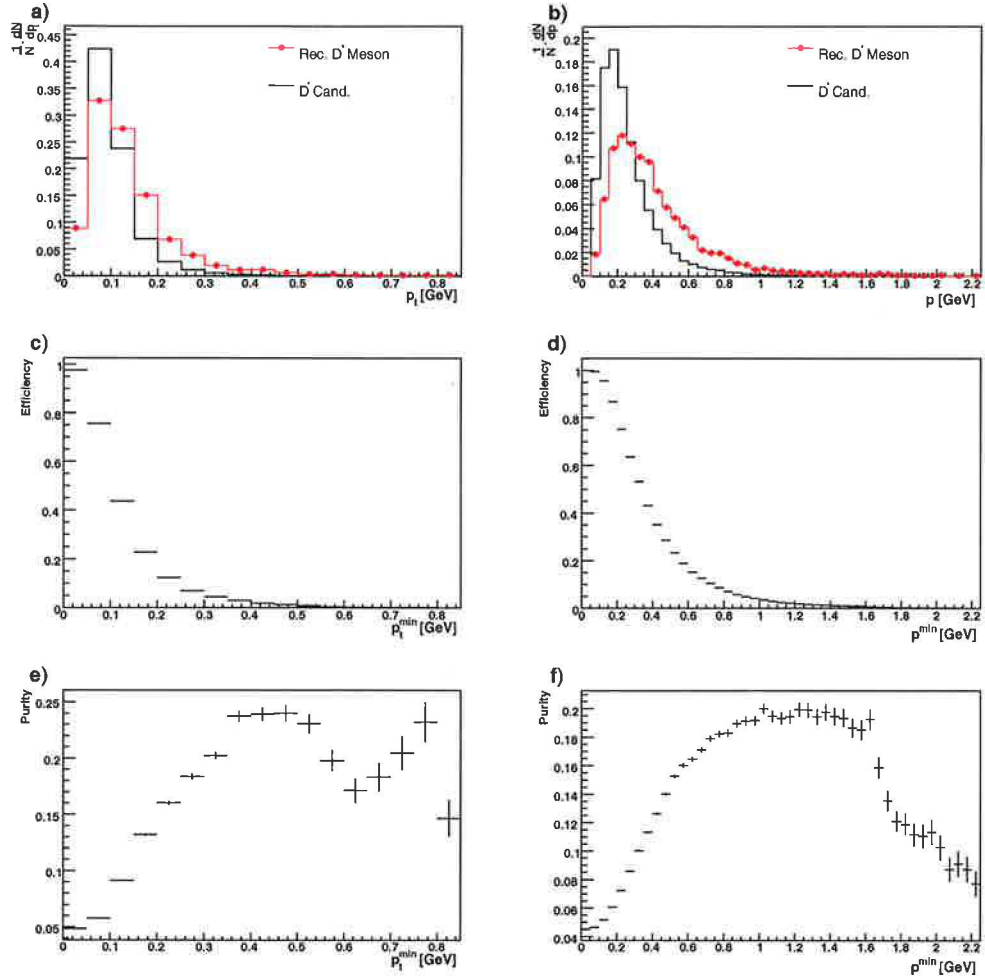


Figure 5.4: Normalised distributions of a) transverse momenta p_t and b) absolute momenta p of π_{slow} . Efficiencies (c,d) and purities (e,f) as functions of the lower limits p_t^{min} and p^{min} of π_{slow} .

applied on π and K have similar effects since they originate from the decay of D^0 .

The momentum restrictions of D^* and D^0 have the biggest influence on the purity of the signal as it is demonstrated in Figs. 5.7 and 5.8. The purity changes from the small value of 5% up to about 25% before it starts to oscillate or saturate, whereas the efficiency is decreasing. Here one can

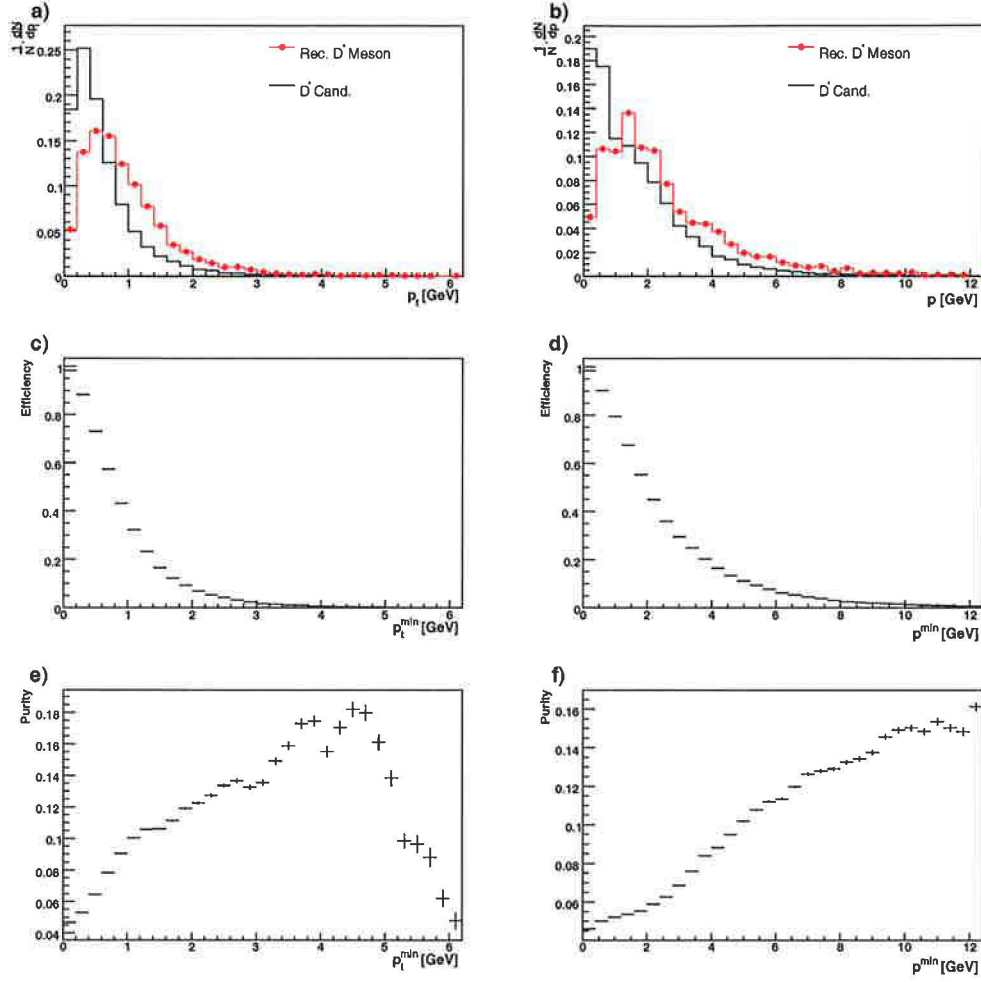


Figure 5.5: Normalised distributions of a) transverse momenta p_t and b) absolute momenta p of π . Efficiencies (c,d) and purities (e,f) as functions of the lower limits p_t^{\min} and p^{\min} of π .

reach better optimisation of the limits of the momenta than for K , π and π_{slow} mesons.

Distributions of the effective mass m of the D^0 candidates and reconstructed mesons are shown in Figs. 5.9 a), b). The D^* candidate is accepted if its reconstructed mass m of D^0 is within the region

$$\Delta m_0 < |m_{D^0} - m| \quad (5.6)$$

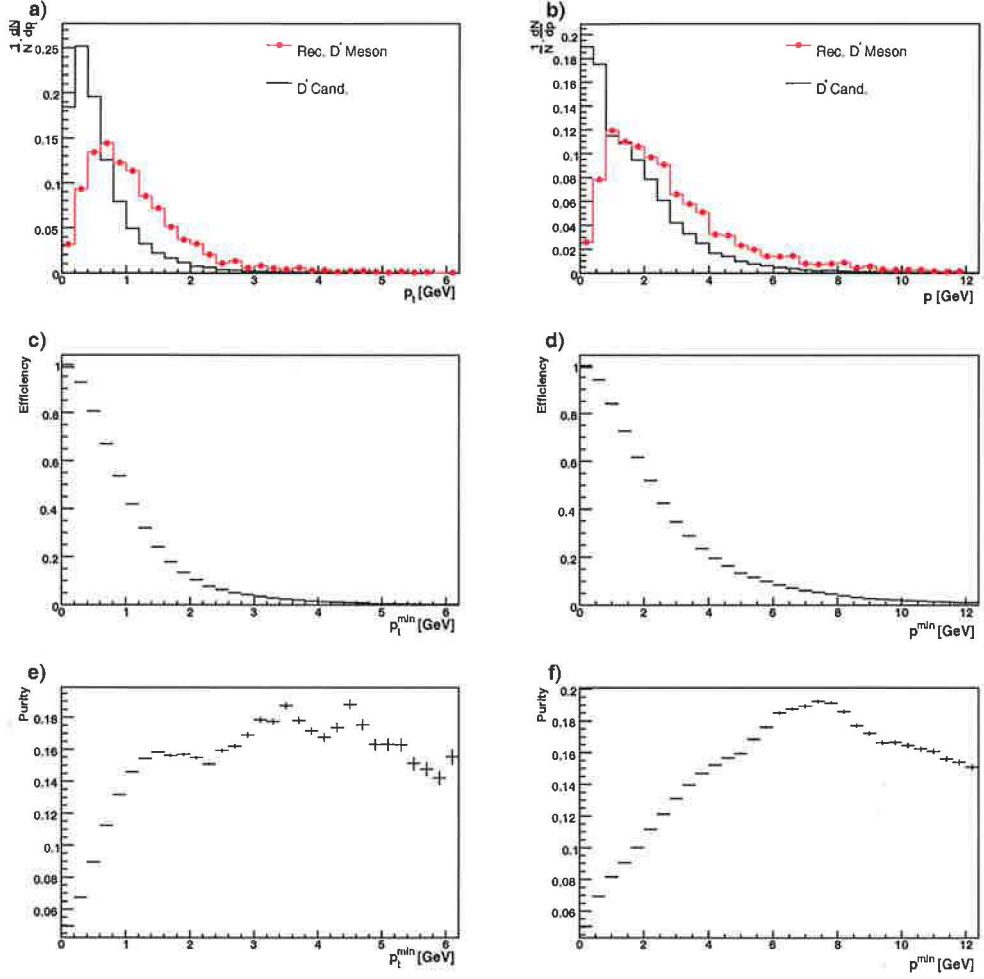


Figure 5.6: Normalised distributions of a) transverse momenta p_t and b) absolute momenta p of K . Efficiencies (c,d) and purities (e,f) as functions of the lower limits p_t^{\min} and p^{\min} of K .

where the m_{D^0} is the nominal mass of the D^0 meson. The influence of the limit Δm_0 is shown in Figs. 5.9 c), d). On one hand the efficiency increases with Δm_0 on the other hand the purity decreases since the contribution of background candidates rises.

Another selection criterion can be based on the absolute momenta ordering of the stable decay particles. The momentum of π_{slow} can be required

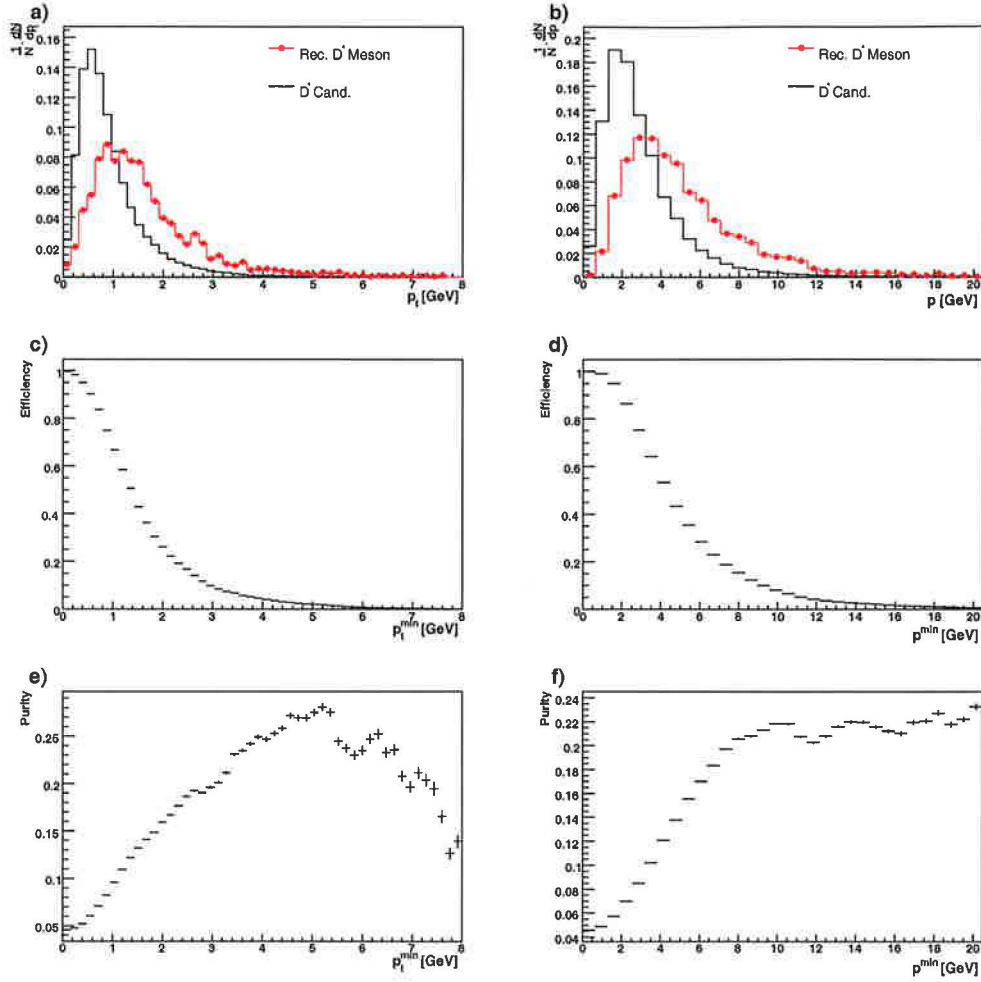


Figure 5.7: Normalised distributions of a) transverse momenta p_t and b) absolute momenta p of D^0 Efficiencies (c,d) and purities (e,f) as functions of the lower limits p_t^{\min} and p^{\min} of D^0 .

to be the lowest one of all stable decay products which is visible in the momentum distributions in Figs. 5.4, 5.5 and 5.6. The multiplicity of the D^* candidates then decreases by a factor 2 with negligible efficiency loss.

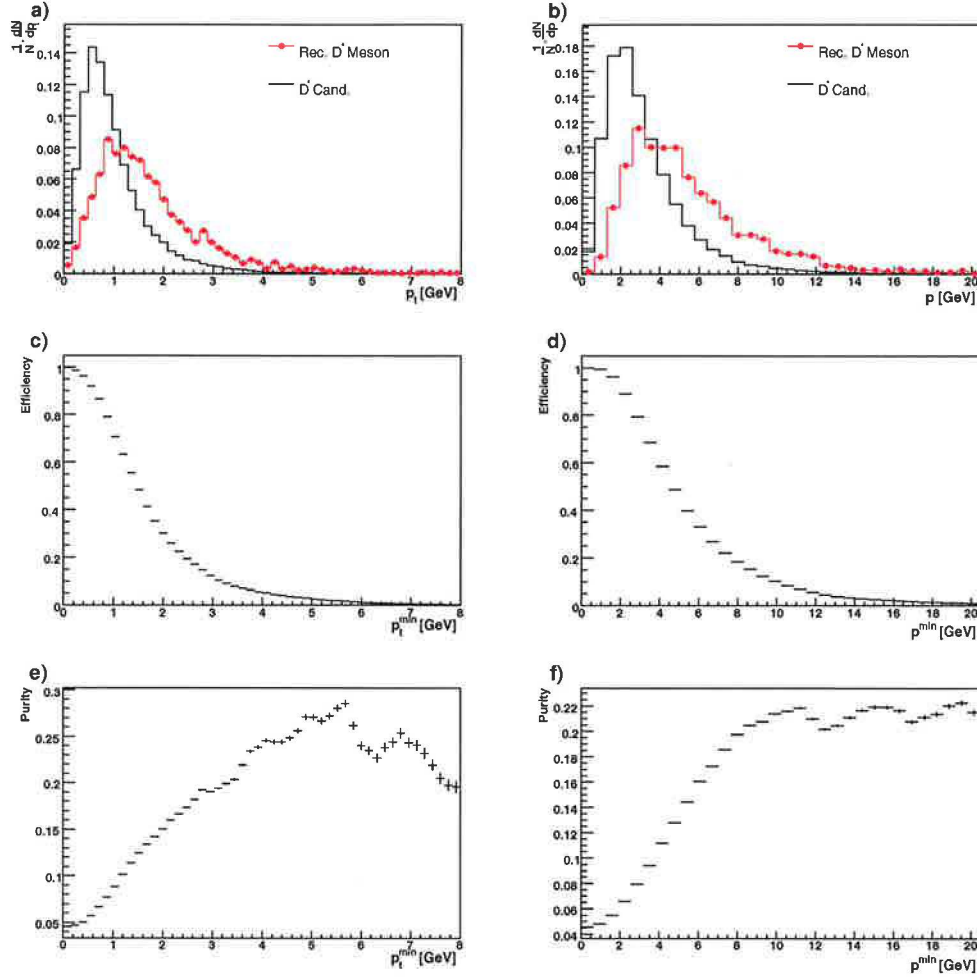


Figure 5.8: Normalised distributions of a) transverse momenta p_t and b) absolute momenta p of D^* . Efficiencies (c,d) and purities (e,f) as functions of the lower limits p_t^{\min} and p^{\min} of D^* .

Track Selection

Tracks which are reliable and rather precise are used for the reconstruction of π_{slow} , π and K mesons. FST and CTD tracks must have non zero curvature in order to determine particle charges and momenta. The reliable track reconstruction is ensured by selecting the central fitted track with at least 15 hits. The FST tracks must be reconstructed with at least 8 hits.

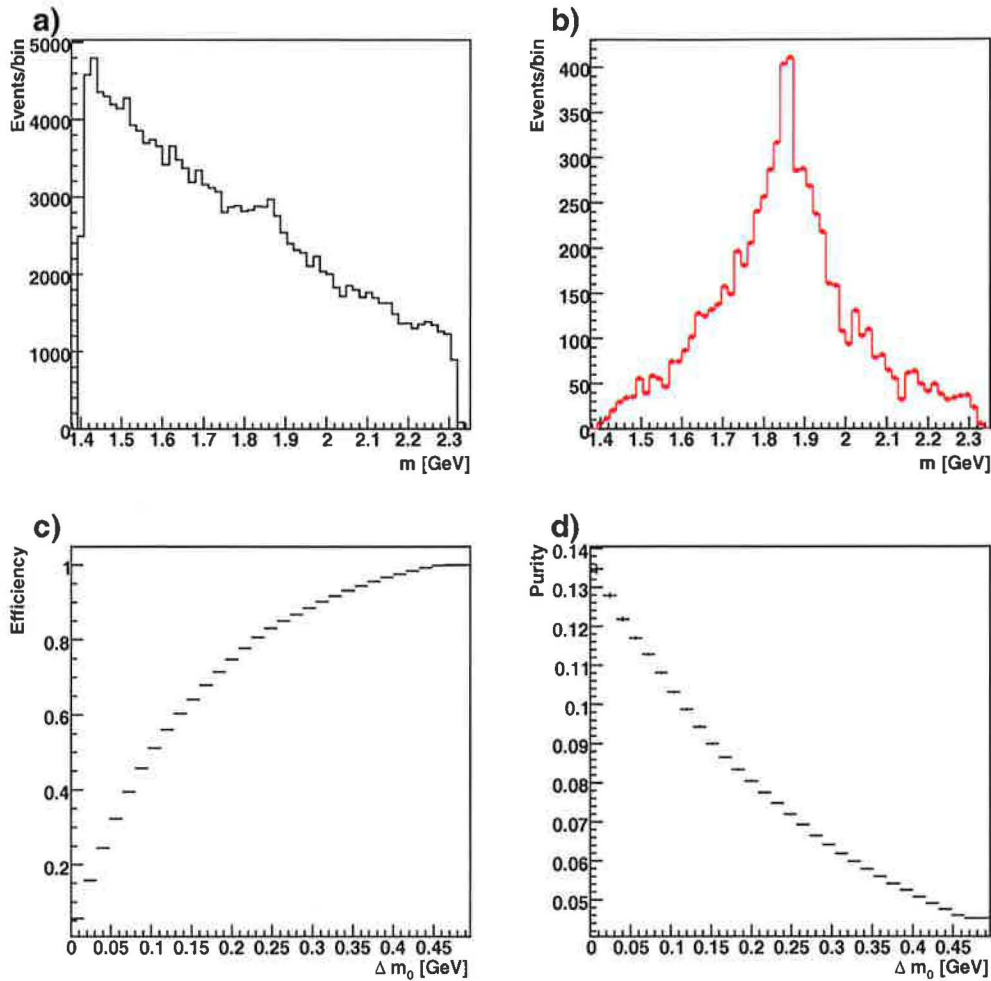


Figure 5.9: a) Effective mass distribution of D^0 candidates. b) Effective mass distribution of D^0 reconstructed mesons. c), d) Efficiency and purity dependence on Δm_0 limit.

Global Selection

For further purity improvements the track multiplicities has been studied. The multiplicity of the FST tracks is very low therefore no restriction of the maximum number of the FST tracks would lead to an improvement of the purity. On the other hand the multiplicity of the CTD tracks in an event with the reconstructed D^* meson shows lower values than in any other event (see

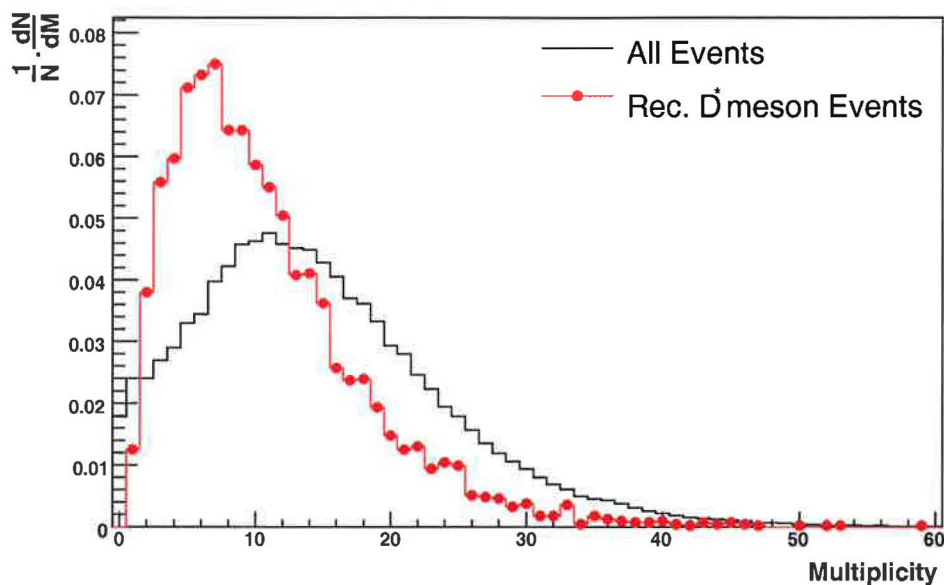


Figure 5.10: Normalised distributions of multiplicities of the central fitted tracks for all events and events with the reconstructed D^* meson.

Fig. 5.10). Therefore a selection of events with the number of reconstructed central fitted tracks < 20 is used.

5.2.4 D^* Selection

The optimisation of various cuts resulted in the set of limits presented in Tab. 5.3. The distribution of Δm depicted in Fig. 5.11 was obtained from MC data applying the geometry and kinematic cuts presented in Tab. 5.3 and including the track requirements and the global event properties mentioned above.

The background (black) is determined as a difference between the contributions of all D^* candidates and the reconstructed D^* mesons. The mass peak is clearly visible in the spectrum and can be fitted by a Gaussian curve supplemented by a function specific for combinatorial background. The mean value of the peak $\langle \Delta m \rangle = 145.9 \pm 0.3 \text{ MeV}$ is close to the nominal Δm value (see Tab. 5.1). The width $\sigma = 1.9 \pm 0.3 \text{ MeV}$ of the Gaussian fit corresponds to the resolution of the tracks used for the reconstruction.

Geometry limits	
D^0 :	$0.0 < \eta < 5.0$
D^* :	$0.0 < \eta < 5.0$
Kinematic limits	
π_{slow} :	$p_t > 0.125 \text{ GeV}$ $p > 0.5 \text{ GeV}$
π :	$p_t > 0.250 \text{ GeV}$ $p > 0.5 \text{ GeV}$
K :	$p_t > 0.250 \text{ GeV}$ $p > 0.5 \text{ GeV}$
D^0 :	$p_t > 1.0 \text{ GeV}$ $p > 2.0 \text{ GeV}$
	$ m_{D^0} - m < 0.1 \text{ GeV}$
D^* :	$p_t > 1.0 \text{ GeV}$ $p > 2.0 \text{ GeV}$
	$ m_{D^*} - m < 0.2 \text{ GeV}$

Table 5.3: Set of cuts used.

The numbers of D^* candidates within $3 \cdot \sigma$ interval around the peak value are summarised in Tab. 5.4. The purity of the signal determined from the histogram values reaches relatively high value of 56.6% whereas the purity which can be obtained by the fit is 35.14% only. The smaller value of the fit is caused by the contribution of worse reconstructed D^* mesons visible at the higher values of Δm .

The overall efficiency after the mentioned cuts has decreased to 4.7%. It is calculated from the number of the reconstructed D^* mesons without any cuts within the $3 \cdot \sigma$ of the obtained peak and the histogram value of the reconstructed D^* mesons. Better purity of the signal could be achieved with stricter cuts at the expense of further efficiency loss.

5.3 Data Analysis

Experimental data, which contain FST tracks, were collected with the H1 detector at HERA in the time period¹ 29.02. 2004–14.05. 2004 which corre-

¹A water leak appeared on the 14th May in the cooling circuitry inside the FST. It destroyed most of the FST sensors.

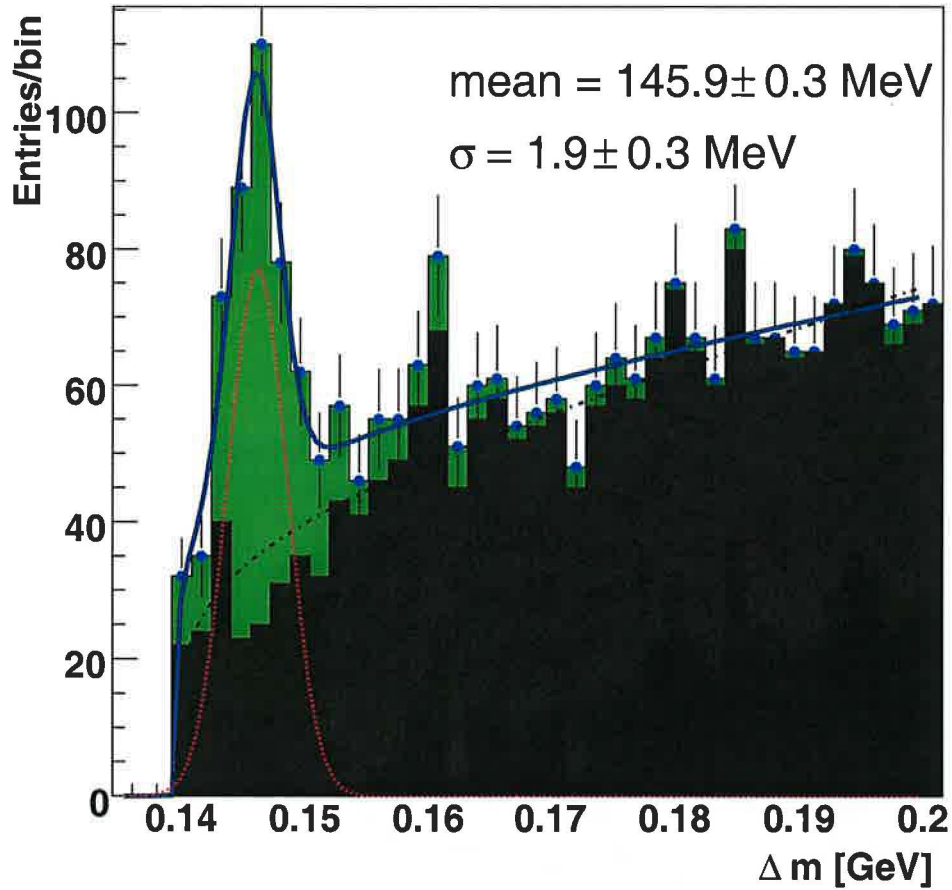


Figure 5.11: Distribution of Δm of simulated events. The black filled area corresponds to the combinatorial background of the D^* candidates. The green area above is the contribution of reconstructed D^* mesons. The dotted red line is the Gaussian fit of the reconstructed D^* mesons only. The background is fitted by the dash-dotted line. The full black line is the fit of the whole spectrum (blue points) by the Gaussian curve and supplemented by a background function. The mean and σ are the parameters of the Gaussian function included in the fit.

sponds to the run number range 373419–381911. This data sample will be further referred as data or data 2004 period.

	Histogram values	Fit values
Number of D^* mesons	296	185 ± 20
Background	232	342 ± 52
Sum	528	527 ± 55
Purity	56.6%	$35.1 \pm 5.3 \%$
S/N	1.3	0.54 ± 0.10

Table 5.4: Number of D^* mesons, combinatorial background candidates and their sums within $3 \cdot \sigma$ interval determined from the histogram and fit shown in Fig. 5.11. The histogram values are obtained from the number of entries in the histograms. The fit values are determined from the integral of the function.

5.3.1 Luminosity

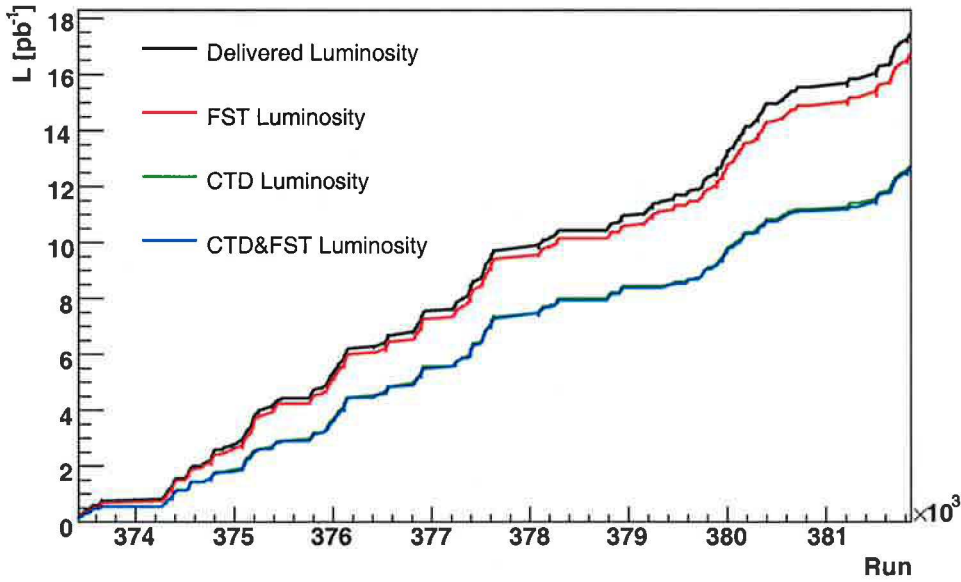


Figure 5.12: Integrated luminosity evolution vs. run number.

The luminosity was measured by the H1-luminosity system (see 2.2.4). The evolution of the integrated luminosity in data 2004 period is shown in Fig. 5.12. The total integrated luminosities are summarised in tab. 5.5.

The delivered luminosity is the overall luminosity provided by the HERA

Delivered luminosity	$\mathcal{L} = 17.43 \text{ pb}^{-1}$
FST luminosity	$\mathcal{L} = 16.68 \text{ pb}^{-1}$
CTD luminosity	$\mathcal{L} = 12.75 \text{ pb}^{-1}$
CTD & FST luminosity	$\mathcal{L} = 12.66 \text{ pb}^{-1}$

Table 5.5: Integrated luminosity for the 2004 FST luminosity data.

accelerator. The FST luminosity is calculated from runs where the FST was in operation. The CTD luminosity was determined from the running period where the CJC and complementary trackers CIP, COZ, CST were switched on full high voltage (HV). It is 76% of the delivered luminosity since the background conditions were not ideal and sometimes the chambers could not be operated at full capacity. The CTD & FST luminosity corresponds to the runs with good performance of both trackers.

5.3.2 Event Selection

The data 2004 itself contain non negligible amount of background induced events. The aim of the event selection is to choose DIS neutral current process events and to suppress the background events.

The distribution of z -coordinates (z_{vtx}) of the reconstructed primary vertices is shown in Fig. 5.13. It was fitted around the maximum with a Gaussian function which gives the mean value $z_0 = 2.3 \text{ cm}$ and the width $\sigma = 10.8 \text{ cm}$. To reduce the background the limits $|z_{vtx}| \leq 35 \text{ cm}$ was set. It is obvious that some background still remains in the selected data sample.

The variable $E - P_z$ denotes the difference between sums of all energies E of the measured particles and the sum of the longitudinal momenta P_z . Under the HERA conditions it should peak around the value of 55 GeV as it is demonstrated in Fig. 5.15 where the difference $E - P_z$ of simulated events is plotted. Since some particles can escape the detection lower values of $E - P_z$ can be expected. On the other hand higher values can be caused by neutral particles the momenta of which can not be reconstructed. The difference between the distributions in Figs. 5.14 and 5.15 indicates, that the cut $27.5 \text{ GeV} < E - p_z < 70. \text{ GeV}$ will reduce the background significantly.

The analysis is based on events which contain a scattered positron detected in the Spacal backward calorimeter. Scattered positrons are identified

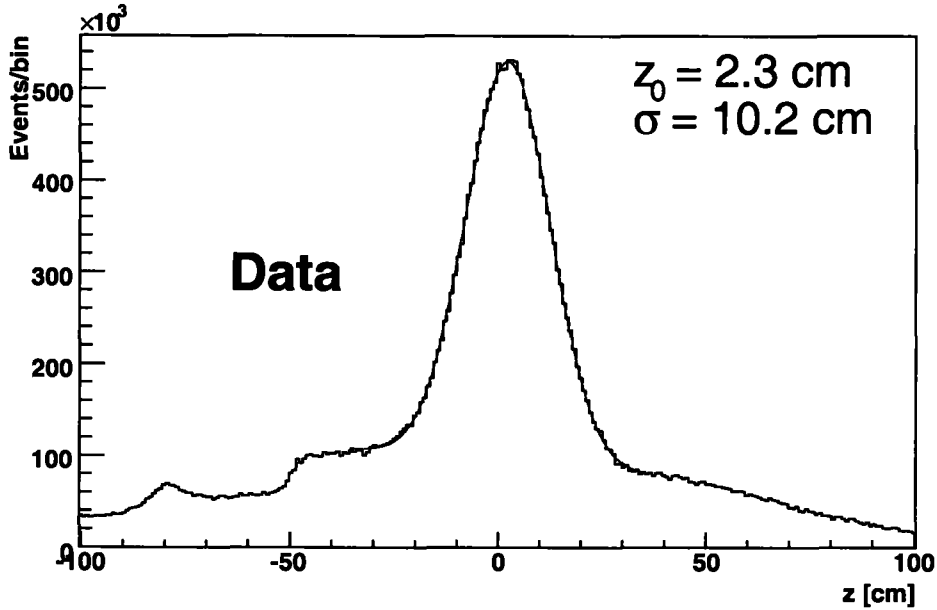


Figure 5.13: Distribution of reconstructed z -coordinates of the primary vertices for data 2004.

as clusters in the Spacal with energies $E_{e'} > 8$ GeV, with cluster radii less than 3.5 cm. The cluster centers must be spatially associated with a charged track candidate in the BPC. The restrictions $Q^2 > 2$ GeV and $y < 0.7$ ensures the DIS process selection.

The above mentioned cuts lead to the vertex distribution shown in Fig. 5.16 and $E - p_z$ distribution in Fig. 5.14 which have negligible background contribution.

The improvement of background conditions is visible in the distributions of the FST track parameters depicted in Figs. 5.17 and 5.18. The agreement between the simulation and data is much better compared to the Figs. 4.7 and 4.6. The azimuthal angle ϕ distribution (see Fig. 5.17) improves significantly. Small difference between MC and data distribution in the angular range $-135^\circ < \phi < -70^\circ$ is caused by the dead u detector modules in disc 0 (see Fig. 4.18). The polar angle θ distribution of the FST tracks (see Fig. 5.18) shows still some background contribution especially at lower values of θ .

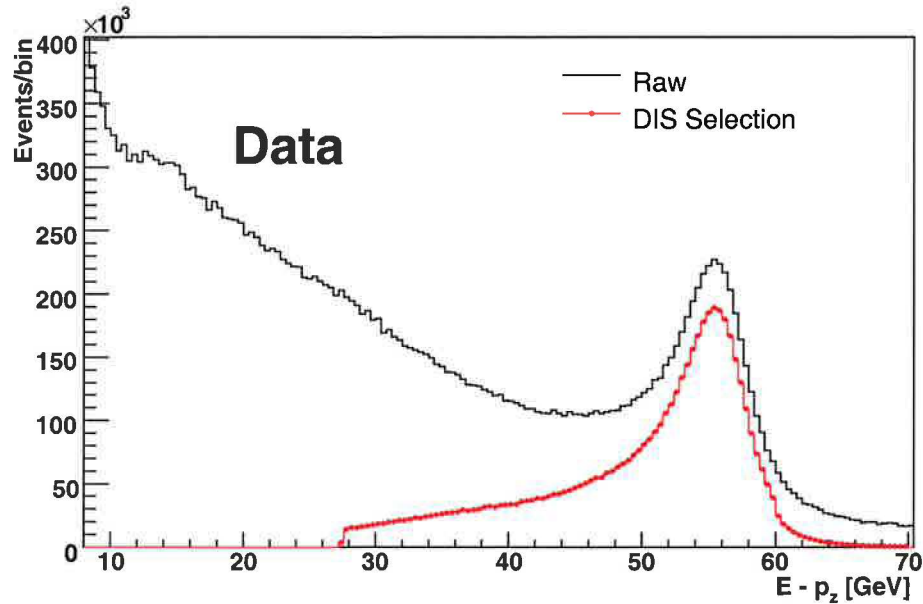


Figure 5.14: Distribution of $E - P_z$ variable for data 2004 before applying the selection criteria (Raw) and after the selection (DIS Selection).

5.3.3 Trigger Conditions

In the running period of 2004 there was not implemented any dedicated trigger for the event detection in the FST. The selected events were registered by subtrigger elements in which other subdetectors are included. The occupancy of L1 subtrigger elements² depicted in Fig. 5.19 is obtained from MC events in which FST D^* meson was reconstructed. In the first bin at value -2 the number of events is plotted. Bin at value -1 denotes the number of not triggered events. It is apparent that all events are triggered.

5.3.4 D^* Data Analysis

All selections were applied to search for FST D^* events. Fig. 5.20 shows Δm distributions for MC and the data sample. Monte Carlo distribution was normalised to the data luminosity with assumption of 100% FST track reconstruction efficiency. The D^* selection criteria were chosen according

²Numbering of subtrigger elements starts from 0.

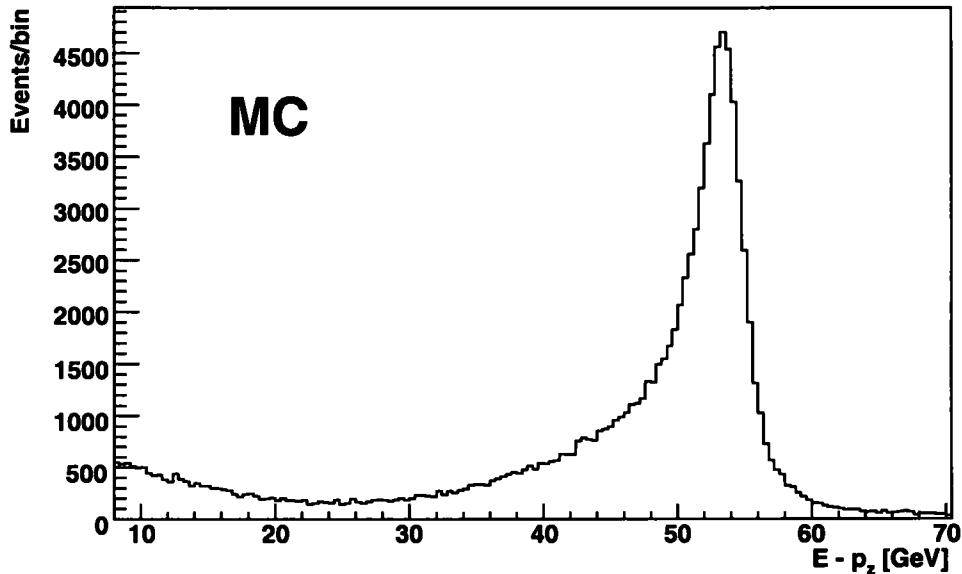


Figure 5.15: Distribution of $E - P_z$ variable for MC.

to the previous efficiency and purity studies (see Tab. 5.3). Moreover the selection of the FST tracks with parameters $|z_0| < 35$ cm and $5^\circ < \theta < 35^\circ$ were used to suppress background induced tracks (see section 4.1.4).

There still remain other inclusive DIS processes in data which contribute to the combinatorial background. The cross section of these processes is higher than the cross section of the heavy flavour production in e^+p DIS. Therefore combinatorial background is so high that the Δm peak is on the level of fluctuations and therefore not visible.

To reach the detection of D^* by means of the FST in the data stricter selection criteria should be applied. That would result in loss of the efficiency of the detection and cannot be used for limited amount of the analysed data. Therefore higher luminosity is needed to detect D^* meson with the FST.

There still remains the possibility to use the FST in combination with FTD, or to get more precise FST tracks to reach better resolution and therefore narrower and higher Δm peak. For that purpose a link with the tracks of FTD or CTD is planned for future analyses of data taken in 2006-2007.

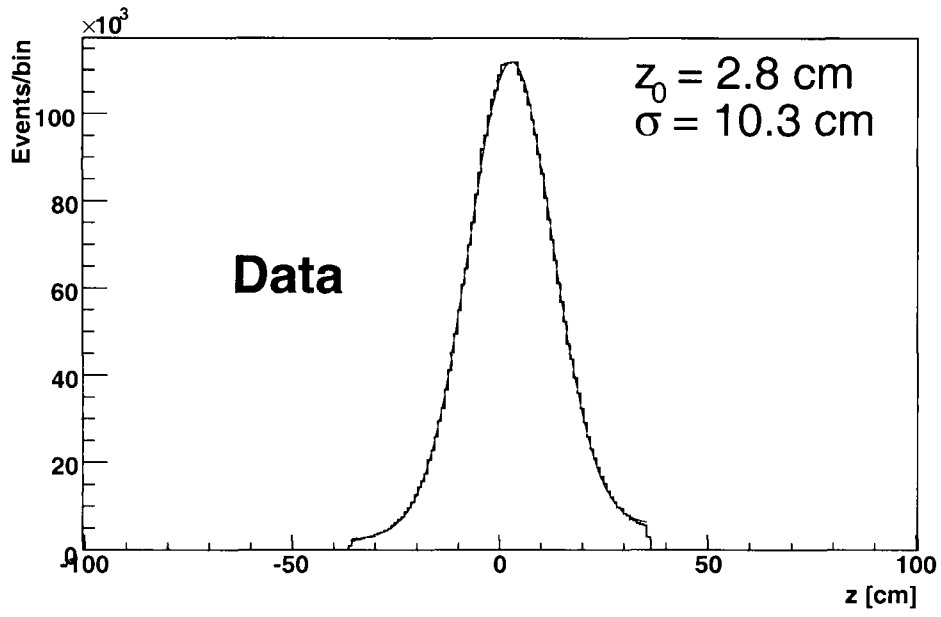


Figure 5.16: Distribution of reconstructed z -coordinate of the primary vertex for data 2004 after the event selection.

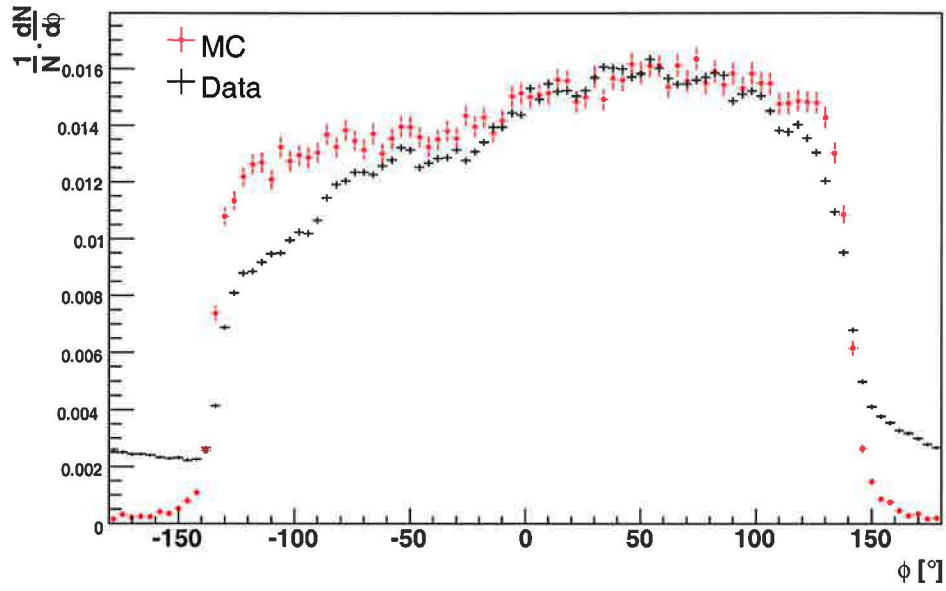


Figure 5.17: Normalised distributions of the azimuthal angle ϕ of FST tracks for MC and selected data. The MC distribution is normalised to 1. For better comparison the data distribution is normalised to the maximum value of the normalised MC distribution.

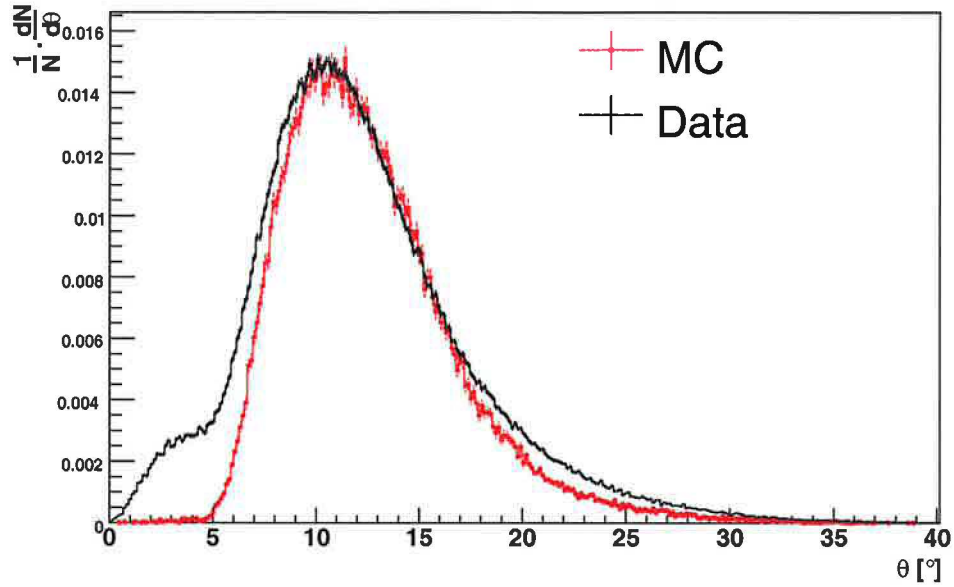


Figure 5.18: Normalised distributions of the polar angle θ of FST tracks for MC and selected data.

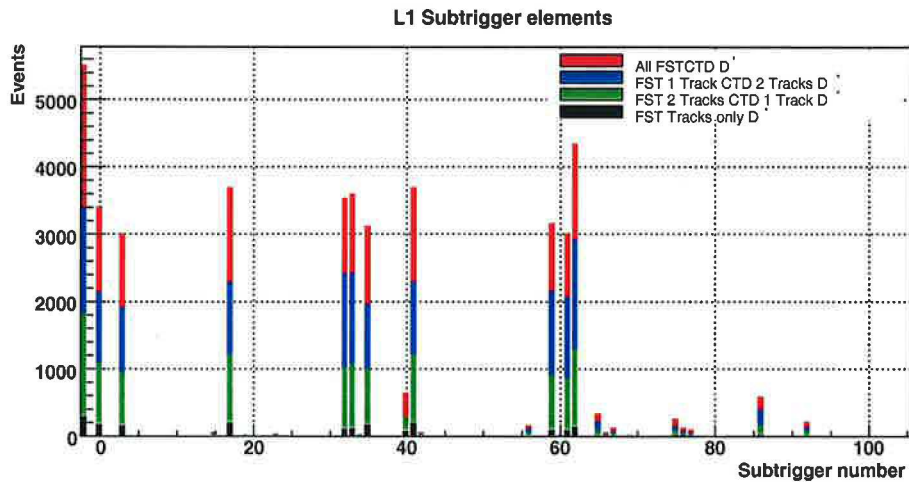


Figure 5.19: MC L1 subtrigger elements distribution. Events with reconstructed D^* meson are taken into account only.

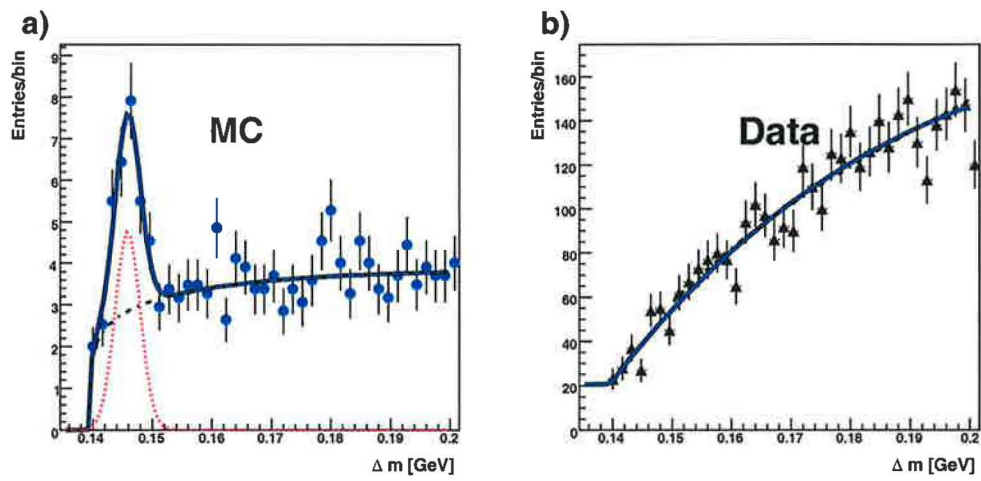


Figure 5.20: Distribution of reconstructed Δm of D^* candidates. a) MC distribution normalised to the data luminosity. b) Data 2004 distribution.

Summary

This thesis presents the design, readout system and event reconstruction of the Forward Silicon Tracker (FST), silicon strip detector of the H1 experiment at HERA. The detector response was studied with MC simulation and data taken in 2004. In addition the investigative study on D^* detection using the FST is reported.

The FST was built and installed in 2001 to provide a precise measurement of the particle tracks in the forward region of the H1 detector. The slow control system for the supply and monitoring of the detector was developed providing the user friendly interface. Necessary adjustments of the hardware preceded the data taking therefore a clock driving sequence for the APC128 and decoder chips was tuned to reach high quality of the detector response and adjusted for triggering of the digitisation of the analog signal.

The data acquisition system was implemented into the existing silicon tracker branch of the H1 DAQ chain. It was adopted from previous scheme of the CST subbranch. Since the new boards (RIO2) are used the main program (R2PowerPC routine) for handling of the data and event building had to be completely redesigned. It was successfully applied for the other subbranches of the silicon branch too. The stability and flexibility of the silicon DAQ increased significantly since that time.

The FST response was studied on the basis of the reduced hit information delivered by the online procedure. The stored hit information is then processed by the offline reconstruction code forming the clusters. The clusters are further used for spacepoint reconstruction and track fitting. The achieved precision of the spatial reconstruction reaches the average value of $15.7 \mu\text{m}$. A good spatial resolution of the sensor is ensured by rather high

signal to noise ratio 29 of the sensors, which is achieved by adjustment of the clock signals to meet specific requirements of single modules. The internal efficiency of the sensors exceeds the values of 90% with exceptions of few non-functional or problematic detector modules. Despite that the momentum reconstruction precision of the FST is worsened by the multiple scattering $dpt/pt > 25\%$, which reflects then in the reconstruction of the effective mass of the D^* meson.

The detection of the D^* mesons was examined for the RAPGAP Monte Carlo simulation. Since the angular range of the FST is rather small the probability of the registration of the D^* decay products in the FST only is negligible. Therefore FST must be combined with the CTD to determine D^* signal. It was shown that usage of the FST extends the H1 experiment acceptance for the D^* detection significantly towards the higher pseudorapidity values and higher Bjorken x values in ideal case. The geometrical acceptance range of the FST is rather narrow. Therefore the number of the D^* mesons detected by means of the FST is lower than the number of D^* mesons detected in central region. The combinatorial background is increased by the contribution of the forward jets and the imprecision of the particle momentum determined by the FST causes difficulties in the D^* signal determination. Therefore the influence of applied geometrical, kinematical and global restrictions on the purity and the efficiency of the D^* meson reconstructed by means of FST was studied showing positive results. The reasonable signal purity of the D^* signal in the MC simulation of $35.4 \pm 5.3\%$ was reached at the expenses of low efficiency of 4.7%. Insufficient amount of data taken with the FST did not allow the detection of the D^* in the data sample. The procedure of the D^* detection was tested with the central fitted tracks on the same data sample detecting the expected D^* signal.

It can be concluded that the FST is a useful tool for the measurement of the charged particles with possible detection of the D^* mesons. The combination of the FST and FTD (resp. CTD) tracks would result in the longer more precise tracks and therefore a better particle momentum resolution could be achieved. The higher amount of the data would be needed for any further physics analysis with the FST, which are nowadays being taken in running period 2006–2007.

Appendix A

APC128 and Decoder Readout Chips

A.1 Decoder

The decoder chip is an ASIC designed especially for controlling the APC128. It performs a serial to parallel conversion of the incoming signals with different functions:

- i) Providing the control signals for the APC128;
- ii) Sending a digital sequence of 32 bits as a calibration signal to the APC;
- iii) Providing the switches for slow control purposes e.g. temperature control; not used in the BST and the FST;
- iv) Regulating the analog current source for the APC preamplifier; not used in the BST and the FST;

The decoder chip is driven with two clock signals (**CLK1**, **CLK2**), **SR/OUT** signal which switch two modes of the chip and **BIN** signal feeding the serial data into the chip (see Fig. A.1).

The first mode of operation is downloading a data bit string containing up to 64 bits into the internal 64 bit shift register. The information from this register is passed to other internal registers in the second mode depending on the first four bits in the shift register. Decision whether the calibration, control or current supply register will be filled depends on the next 3 bits.

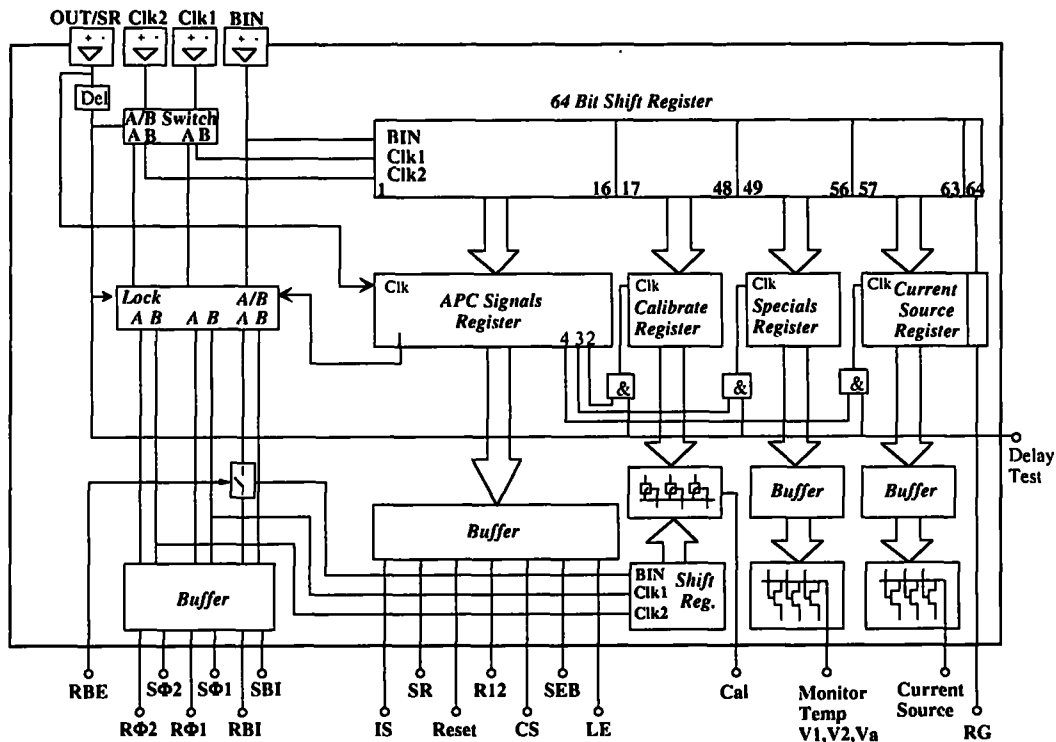


Figure A.1: Decoder chip schematic view.

The remaining bits up to the bit 16 in the shift register are reserved for the control of the switches of the APC. This information from the shift register is transferred to the APC signal register every time the decoder is in the second mode. In the second mode the clock signals are patched through as the APC clock signals. Switching between the **A/B** functions depends on the first bit of decoder shift register. It means in fact the switching between **R ϕ** and **S ϕ** clocks.

A.2 APC128

The APC128 chip contains 128 preamplifiers, followed by a 32 time slices deep pipeline for the storage of the analogue amplitudes. Its functionality is driven by 14 control signals (see Fig. A.2) delivered by the decoder. Each readout strip is connected to one input of the chip. The signal is amplified by the inverting **Analog preamplifier** and stored to one of the 32 time slices

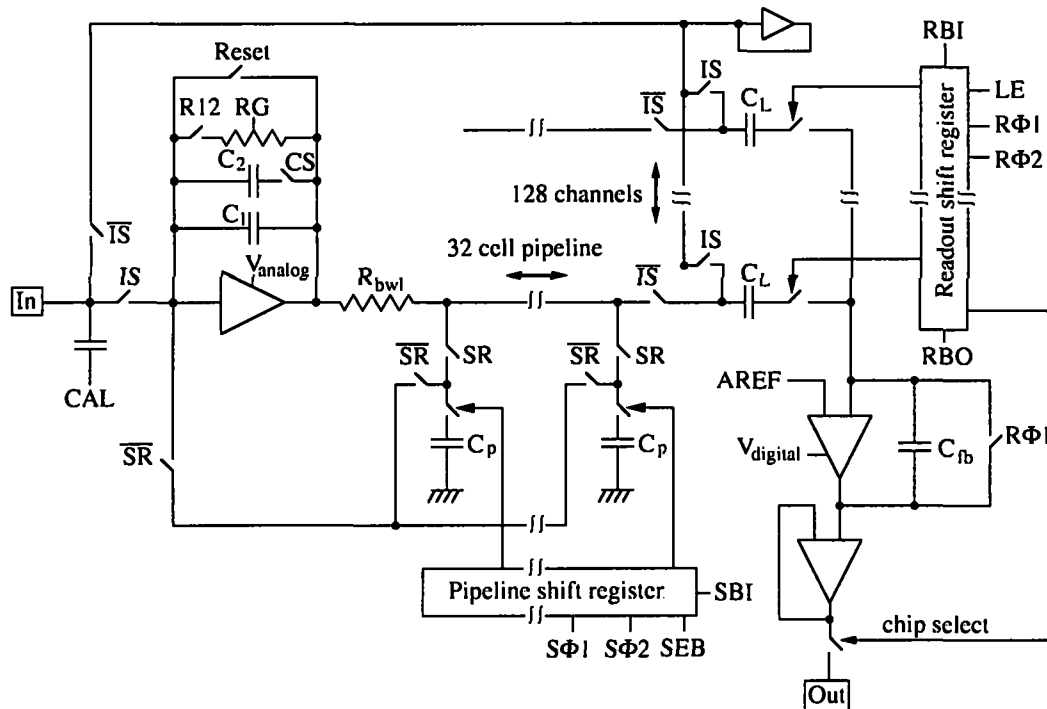


Figure A.2: Circuit diagram of one channel of APC128

of the capacitor array controlled by the **Pipeline shift register**. The signal from the addressed C_p capacitors is read out after a trigger decision and it is stored on the latch capacitor (C_L). Then after addressing by the readout shift register the signal is again amplified by the output amplifier and passed to the subrepeater board. Two detector modules i.e. ten APC128 readout shift registers are read out sequentially.

There are calibration capacitors connected parallel to the input in groups of four such that by applying the calibration voltage pulse four neighbouring strips receives four different signals. The difference between the calibration signals is the same which is ensured by using same capacitor values connected parallel in numbers 1, 2, 3, 4.

A.3 Readout Sequence

There are two main phases according to the H1 trigger signals (see 2.2.5). The signals from the detector are stored into the **Pipeline shift register** during the **Sampling** phase and after positive trigger decision the appropriate signals is read out during the **Readout** phase.

The whole APC128 readout procedure can be divided into four sequences:

Initialisation – resetting all the sample capacitors C_p and setting the latch capacitors to the initial value.

Sample sequence – sampling of the input charge and storing the corresponding voltage into the capacitor array until this cycling is stopped by the H1 trigger decision.

Re-read sequence – re-reading and amplifying the signals from the “signal” capacitor and storing the information on the latch capacitor.

Readout sequence – readout of signals stored on the latch capacitors, amplification and conversion to a digital signal.

Initialisation

Reset is switched on first and then by so called “race-through” (both clocks are active at one moment) of the $S\Phi$ clocks and **SBI** bit set to zero. **Pipeline shift register**, sample capacitors and the input preamplifier are reset.

The readout register is set in similar way. The “race-through” of the $R\Phi$ clocks with **RBI** are set to one. The latch capacitors are supplied with a stable voltage by the amplifier in the right upper part of the APC128 schematic diagram (see Fig. A.2).

The initialisation must proceed via the **Sample sequence**. Since it is time consuming because some relaxation time is needed to reset and set the shift registers, it takes place at the end of the **Readout** phase.

Sample Sequence

IS and **SR** switches are closed during the whole sample sequence to ensure the connection between the active strip, preamplifier and sample capacitors. The integrated signal (**R12** switch is closed) is stored into one sample capacitor every beam crossing.

SBI is set to logical one and shifted through the whole **Pipeline shift register** using the $S\Phi$ clocks, addressing the sample capacitors sequentially. A new **SBI** bit is generated after one cycle 32 beam crosses. The information stored in the pipeline capacitors is overwritten. It repeats in a loop until the positive trigger signal of H1 system arrives (see 2.2.5).

This sequence takes place in the **Sample phase** only.

Re-read Sequence

Opening of switches **IS** and **SR** disconnects the detector from the chip in this phase. **R12** is released too. **Pipeline shift register** is disconnected from storage capacitors (C_p) by setting **SEB** bit. The **Reset** switch is closed. The output amplifier and the **Readout shift register** are reset by the “race through” of the $R\Phi$. While the capacitors C_p are still disconnected the pipeline shift register is clocked to the intended position using the clocks with the generation of an overflow signal¹. The capacitor containing the signal from triggered event is addressed.

The **Reset** is released and using the **SEB** bit the charge stored on the addressed sample capacitor is re-read, amplified, and stored on the latch capacitor. This can be done for an arbitrary number of sample capacitors, their signal charge is then added to the already stored charge.

Re-read sequence takes place at the beginning of the **Readout phase**.

Readout Sequence

The stored charge is read out serially from the latch capacitors by clocking the readout shift register ($R\Phi$ clocks) and then amplified with the readout amplifier.

The contact to the **Readout shift register** is enabled with the bit **LE**. Then the **RBI** bit is shifted through the **Readout shift register** to connect latch capacitors sequentially. The **RBI** bit is passed to the next APC through an **RBO** after reading out the current APC until the fifth APC of the module.

¹If the end of the shift register is reached the **SBI** bit is generated

Appendix B

Slow Control Modules

In this chapter slow control components of the FST and BST will be described in details.

B.1 MacVEE Bus

The MacVEE bus connect up to 8 MacVEE cards with crate addresses set by the shift switch on the board with values 1–8 providing the address of 0–7. MacVEE card is a simple VME master which has only J1 connector, therefore it is able to provide A24 or A16 bit addressing with D16 or D8 data access to VME bus only. The connection to the Macintosh computer is provided by the Micron NuBUS card.

The VME bus is accessible through the memory window with the base address $0xNM00\ 0000$. N denotes the NuBUS slot of the Macintosh computer¹, M is the address of the MacVEE card. For A16 bit addressing the memory space of $0xNM7F\ 0000$ – $0xNM7F\ FFFF$ or $0xNMFF\ 0000$ – $0xNMFF\ FFFF$ is used.

B.2 Converter Card Module

Converter card VME registers are described in Tab. B.1. Each of them contains one byte of information with each bit reflecting the status of one

¹For Macintosh Quadra 800 and 840AV $N = 0xC - 0xE$, Macintosh Quadra 700 $N = 0x9 - 0xA$

corresponding channel number except the **Status byte**. The CC card VME circuitry acts as A24 VME slave with the base address set by the rotary switch n on the board $0x000n'0000$.

VME Add.		Description
0x00	ro	Status Byte
0x02	rw	Depletion Volt. Select
0x04	ro	Depletion Volt. Value
0x06	ro	Depletion Volt. Error
0x08	rw	Supply Channel Select
0x0a	ro	Supply Channel Error
0x0c	ro	Digital Volt. Error
0x0e	ro	Analog Current Error

Table B.1: Converter Card VME registers.

Bit Mask	Name	Description
0x04	50V	Additional 50V for HV ON/OFF
0x08	DC/DC	Any CC Channel ON/OFF
0x20	Error	Any CC channel Error
0x40	Busy	CC card reading status

Table B.2: Status byte description.

Switching ON/OFF the voltages is provided by the setting of the **Supply Channel Select** register. If the bit is set to 1 the corresponding digital voltage and analog current are switched on and the depletion voltage may be adjusted.

The sensor bias voltage is adjusted by means of **Depletion Voltage Select** and **Depletion Voltage Value** registers. If some of the **Depletion Volt. Select** bits are set to 1 the pair of modules connected to CC card channel are supplied by $0.5 \times \text{DepletionVoltageValue}$ [V] by disabling the channel, the value of the bias voltage remain.

Any deviation from the current and voltage out of the ranges is reported in the error registers **Digital Voltage Error**, **Analog Current Error** and **Depletion Voltage Error**. A bitwise OR of mentioned registers occurs then in **Supply Channel Error**.

If an error occurs all voltages of the corresponding channel are switched OFF. The error is cleaned by switching off the channel setting the bit in the **Supply Channel Select** to 0.

The **Status byte** register displays brief status of the Converter card. Its bit map is described in table B.2. **50V** bit shows the status of additional supply on the VME-J2 which is converted to the depletion voltage. If any channel of the detector is supplied by the converter card the **DC/DC** bit is 1. The bitwise OR of error register is displayed in **Error**. Until the xilinx chips on the converter card finish the reading of the internal status the **Busy** flag is set.

B.3 BBL3 Signals

The global information of the detector conditions is send from the slow-control program to H1-BBL3 system. The status of the voltage and temperature inside the detector is indicated by the open or close collector of the TTL contact on the IP Unidig. The state of slow-control program is signalised by the unit called Mac Watchdog.

There are 4 BBL3 signals provided by the slow control shown in Tab. B.3.

BBL3 Name of Signal	Meaning
FST	High Voltage status
FST_VOLTAGE_STATUS	Voltage error
Water_Temperature_FST	Water and Temperature alarm
FST_Watchdog	Slow control status

Table B.3: The BBL3 signals provided by the FST slow control System.

FST signal is set on if the depletion voltage for more than 70% of detector modules is on the nominal value i.e. the detector is sensitive. **FST_VOLTAGE_STATUS** signalises a voltage error. If the temperature or humidity in the detector exceed the alarm value set by the slow-control program the **Water_Temperature_FST** signal alerts the H1 BBL3 system.

B.3.1 IP-Unidig

The IP-Unidig [28] is the module with 24 TTL I/O plugged on the VMEbus IP carrier card [29] situated in the converter crate. It can be addressed in VME A16 addressing mode only. The VME-base address is determined by the slot position and setting of the IP carrier.

VME Add.		Register
0x0	rw	Readback lines 1-16
0x2	rw	Readback lines 17-24
0x4	ro	Direct read lines 1-16
0x6	ro	Direct read lines 17-24

Table B.4: IP Unidig registers used for BBL3 signals.

The BBL3 status is provided by setting the bits of the **Readback lines** and can be read from **Direct read lines** (see Tab. B.4). The alarms and status signals are assigned to the bits in the slow-control program according to the connection to the H1-BBL3 system.

B.3.2 Mac Watchdog

The VME base address of the Mac Watchdog module is adjusted by the jumpers on the module 0x00xy0000. It can be addressed only by VME A24 addressing with D8 data access. Its registers (see Tab. B.5) are being read by the slow control program in a loop sequentially **ROIC**, **RAFF**, **ROIC**, **RSB**. Reading of the registers resets the countdown of the module to the value adjusted by the jumpers on the front panel. If the registers are not read within the jumper adjusted period a BBL3 signal is released alarming the H1 system of malfunction of the slow control program.

VME Add.	Register
0x3	ROIC
0x5	RAFF
0x9	RSB

Table B.5: Mac Watchdog VME addresses of the registers.

B.4 Status Link

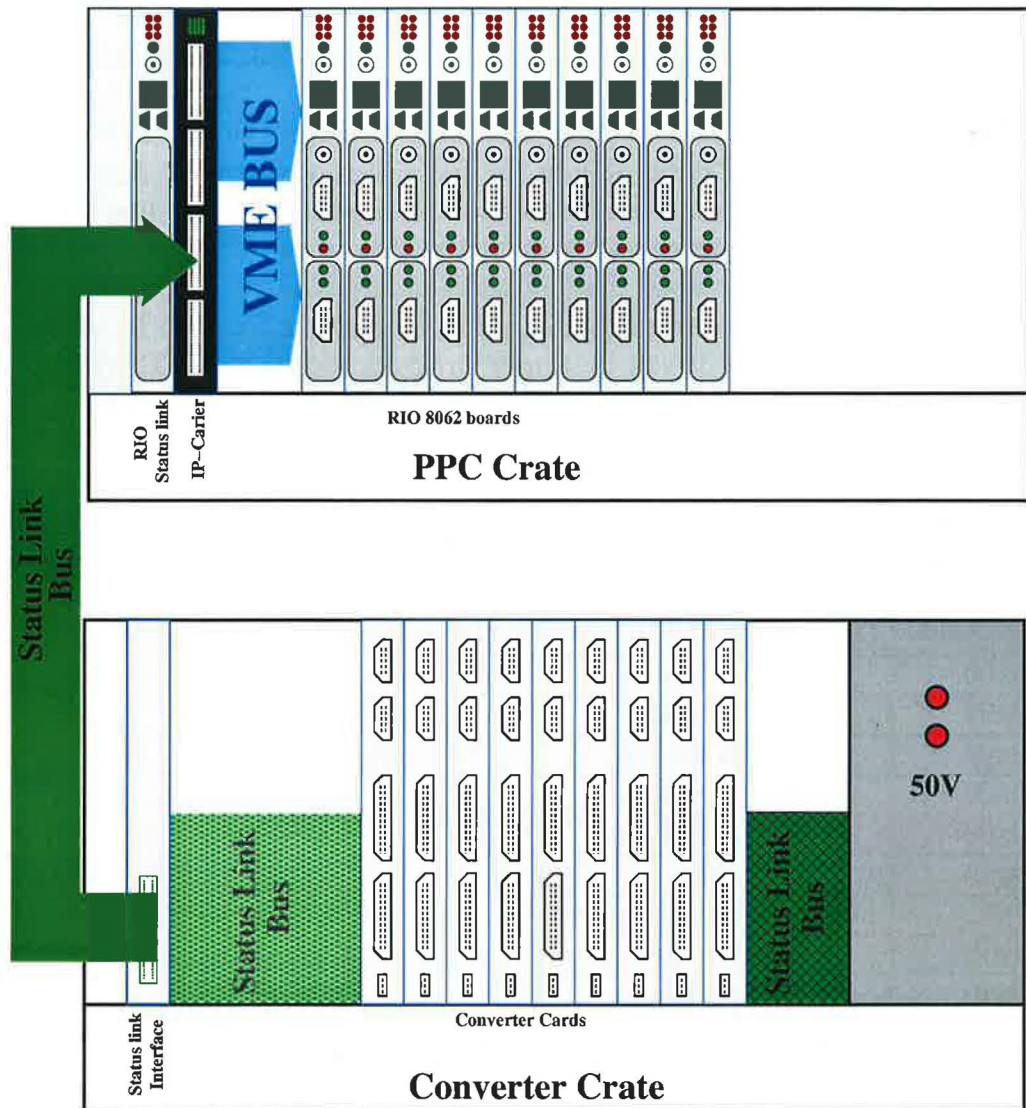


Figure B.1: Status link connection.

The so called status link has been implemented to send the voltage status

from the converter cards to the RIO boards in order to provide the voltage status of the modules for the DAQ system. It is schematically reviewed in the Fig. B. 1.

Any change of the detector supply voltage is send by corresponding converter card to the status link bus implemented on the user bus of VME-J2 connector. The address of the converter card on the status link bus is determined by its position.

The bus is extended from converter card crate through the status link interface to the VMEbus IP carier [30] in the PPC crate with the IP Xilinx module. The IP Xilinx module handles signals from the bus according to the status link protocol and provides the output visible on the VME bus (see Tab. B.6). VME base address of the module is determined by its position and setting of the VME IP-carier. It can receive the status from up to ten converter cards. Module is driven by a user program stored on EEPROM which is downloaded into the Xilinx chip during the reset.

The status link RIO board provides the status from the status link to the DAQ RIO boards. The program controls IP-Xilinx functionality and by any change updates the status of the detector for appropriate DAQ RIO board by modifying one of its mailbox registers (see Tab. C.5).

VME Add.	Register
0x00	CC 0,1 Status
0x02	CC 2,3 Status
0x04	CC 4,5 Status
0x06	CC 6,7 Status
0x08	CC 8,9 Status
0x0A	LAM
0x0C	Machine State Register
0x0E	Enable Low
0x10	Enable High

Table B.6: VME table of the IP-Xilinx module.

The status of the supply voltage of two converter cards is displayed in **CC Status** registers. Every change is marked by setting bit to one in **LAM** register. The position of bit corresponds to the converter card number. The **Machine State Register** bits (see Tab. B.7) serves for the Xilinx chip reset, loading and status link protocol control.

Bit Mask	Description
0x001	Fake Xilinx Reset
0x002	Clear Xilinx Reset
0x004	Soft Xilinx Reset
0x008	Input Multiplexer
0x010	Request bit
0x020	Acquire bit
0x040	Geographic Address Enable
0x080	Increment geographic address
0x100	Extern Reset
0x200	Read Extern Reset
0x400	Read Spare

Table B.7: Machine state register bits.

Appendix C

RIO2 8062 and FADC PMC Board for the FST

RIO2 8062 is a PowerPC based RISC I/O Board. It provides general purposes VME platforms for high speed interfaces. For other details see [31]. Every DAQ RIO2 board houses one FADC PMC board designed for the data acquisition of the H1-silicon detectors. The settings and registers important for the functionality of the boards are presented in this chapter.

C.1 RIO2 Setting

All RIO2 DAQ boards are set identically. For the basic DAQ process described in sec. 3.5.1 the board is set as VME slave. They are set for monitoring and downloading of the SiPPCUser code as VME masters.

C.1.1 Processor Setting

The RIO2 boards are equipped with either PPC 603e or PPC 604e processor. During the initialisation after the boot of the board the data and instruction caches of the processor are enabled as well as the floating point operations which speeds up the RIO2 operations significantly. Any attempt to enabling any cache again invalidates the cache memory. For details see [32].

Internal memory range	VME Address range	
0x0000 0000 – 0x0000 FFFF	0x002r 0000 – 0x002r FFFF	VME A24
0x0000 0000 – 0x00FF FFFF	0x0r00 0000 – 0x0rFF FFFF	VME A32

Table C.1: Mapping of the internal RIO2 memory to VME bus.

VME address range	AM	Internal memory range
0x00C0 0000 – 0x00DF FFFF	0x3d	0xD400 0000 – 0xD41F FFFF
0x0r00 0000 – 0x0r00 FFFF	0x09	0xEr00 0000 – 0xEr00 FFFF

Table C.2: RIO2 VME master memory mapping. The letter r=0x1–0xe denotes the rotary switch of other RIO2 DAQ boards.

C.1.2 VME Slave Setting

A part of the RIO2 internal memory which contains the communication areas and data is visible on the VME bus (see Tab. C.1) accessible in A32 and A24 addressing modes. The base address of every RIO2 board is given by the value of its rotary switch r. The DAQ master board accepts the data from the RIO2 boards with the rotary switches 0x1–0xE.

C.1.3 VME Master Setting

The direct (mapped) access to VME is implemented through two VME windows of 64 and 256 Mbytes. The smaller window is used for access to DPM board memory in A24 mode, the larger one to access the other DAQ boards for monitoring and communication purposes in A32 addressing mode. Mapping is shown in Tab. C.2.

SiPPCUser Code Download

For downloading the hitfinder code the VME block transfer is used by means of RIO2 BMA controller (see [31] sec. 5.4). Compiled SiPPCUser code in

DPM SiPPCUser VME base address	0x00C0 8000
RIO2 SiPPCUser internal base address	0x0070 8000

Table C.3: SiPPCUser code download addresses.

xcoff file format is downloaded into the DPM board from some VME master

board in PPC crate. DAQ RIO board loads the code from the DPM into the internal memory. The downloading of the SiPPCUser code by RIO2 is triggered by writing a special flag into the mailbox area (see Tabs. C.5 and C.6). The size of the hitfinder code is limited by the maximum length of the moved block to 32 kbytes. The DPM VME and the RIO2 internal base addresses of the code are shown in Tab. C.3.

C.2 Memory Map

Name	Address Space	Description
Communication area		
Mailbox	0x00000 – 0x0007F	Mailbox area
DAQSpec	0x00080 – 0x000FF	DAQ Specification area
SiDAQSpec	0x00100 – 0x001FF	Silicon DAQ Specification
SiEventIND	0x01000 – 0x010FF	Silicon Event identification
Data		
SiRawDataBase	0x010 0000 – 0x017 FFFF	Raw data
SiHitDataBase	0x018 0000 – 0x01F FFFF	Hit data
FBPedBase	0x020 0000 – 0x033 FFFF	Pedestals
FBSigmaBase	0x034 0000 – 0x047 FFFF	Sigma
FBSigSqBase	0x048 0000 – 0x05C FFFF	Sqrt Sigma

Table C.4: Memory Map of the RIO board.

Internal memory of every DAQ RIO2 board is organised in two main blocks (see Tab. C.4). First block serves mainly for the communication between the RIO2 board and other VME master boards in the crate. The **Communication area** is visible on VME A24 and A32 addressing space (see Tab. C.1). The second block (**Data**) contains stored data and hitfinding variables.

Register	Address	Description
control word	0x00	Word for VME access check
DateVersion	0x04	unused
Stage	0x08	R2PowerPC subroutine stage
ProcType	0x0A	Processor Type
hword3	0x0C	unused
Rotary	0x0E	Rotary Switch Value
DAQStat	0x10	unused
byte4	0x12	unused
FADCMask	0x13	FADC HV mask
LastEvent	0x14	unused
SiPPCUserIn	0x18	unused
DebugFlag	0x1C	unused
Special	0x20	Special actions flag
Event info	0x30	Event info area

Table C.5: Mailbox area.

0x10AD CODE	Load the SiPPCUser code
0x810B 100B	Stop R2PowerPC subroutine
0x5E8E 1510	Reset the RIO board

Table C.6: Special action flags.

C.2.1 Communication Area Format

Mailbox

Mailbox memory area contains the basic information about the board itself (**Processor type** and **Rotary Switch Value**). The DAQ master board checks the presence of the RIO2 board on the VME bus by addressing **control word** therefore it must not be touched by any internal program or external user operation. The **FADCMask** is modified by the status link RIO. Lower eight bits denote the sensitive voltage status of the modules corresponding to the data channels connected to the PMC. By writing a code word into the **Special actions flag** (see Tab. C.6) register the R2PowerPC routine can be terminated, the board can be rebooted or the SiPPCUser code downloaded. For debugging purposes last processed event information is written into **Event info area** (see Tab. C.7).

Register	Address	Description
SiMode	0x00	Silicon Mode
RawAddress	0x04	Raw Data Address
PPCUnit	0x08	PPC Unit number
PIC	0x0C	Pipeline Counter
HitAddress	0x10	Address of stored Hit Data
EventNumber	0x14	Event Number

Table C.7: Event info area 0x30

DAQ Specification Area

The DAQ specification (DAQSpec) area (see Tab. C.8) is written into the RIO2 internal memory at the base address 0x0080 by the DAQ master board. It contains run specifications and serves for RIO2 as an indicator of the run status. R2PowerPC subroutine reacts to the run start which is denoted by non zero value of **SysMode**¹, by acknowledgement of the run start writing the run number into **RunNumAck** register, cleaning the event identification area preparing the PMC for the data acquisition and starting the data taking algorithm. The run is stopped if the **SysMode** is set to 0. In the case of a warmstart **SysMode** bit 0x8 is set the R2PowerPC subroutine acknowledges the run start and loads the SiPPCUser code only. The **SiPPCMask** register denotes the bit pattern of the RIO2 board numbers which will be read out by the DAQ master board. The inactive RIO2 boards does not obtain the run start information neither the other registers of DAQSpec nor the Silicon DAQ specification area are updated. The other registers are unused for the RIO2 board their description and detailed description of the **SysMode** can be found in [33].

Silicon DAQ Specification Area

Silicon DAQ specification (SiDAQSpec) area (see Tab. C.9) written by the DAQ master contains the information specific for the silicon branch. Many registers used formerly for OnSiROCs became obsolete. Current version of R2PowerPC code handles only the **SiMode** register which denotes format of the data. The **SiMask** word contains the bit pattern of the silicon sub-branches in readout. The bit position denotes the number of the active

¹The run is not started if the 7th bit of **SysMode** is set.

Register	Address	Description
SysMode	0x00	System Mode
RunNum	0x04	Run Number
Trigger1	0x08	Trigger setting 1
Trigger2	0x0C	Trigger Setting 2
XiMask	0x10	
RunNumAck	0x14	Run Number Acknowledge
SiNBuffs	0x18	Number of buffers
SiMaxBytes	0x1C	Maximum length
SiXiDAQ	0x20	
Buffer1AS	0x28	
FebMask	0x30	
DAQMode	0x34	
SiPPCMask	0x38	PPC Mask
FebUnit	0x3C	

Table C.8: DAQ specification area.

Register	Address	Description
SiMask	0x00	Silicon Crate Mask
SiMode	0x02	Mode
SiHDTHR	0x04	obsolete
SiCDTHR	0x08	obsolete
SiVolts12	0x0C	obsolete
SiVolts34	0x0E	obsolete
SiLLRPuls	0x10	obsolete
SiSWTHR	0x12	obsolete
SiPPCMask3	0x14	PPC Mask for CST
SiPPCMask4	0x16	PPC Mask for BST
SiPPCMask2	0x18	PPC Mask for FST
SiRAWM2	0x1A	FADC Raw Mask for FST
SiRAWM3	0x1C	FADC Raw Mask for CST
SiRAWM4	0x1E	FADC Raw Mask for BST

Table C.9: Silicon DAQ specification area: base address 0x0100

Register	Address	Description
EventNumber	0x00	Event Number
SiError	0x04	Error Code
NBytes	0x08	Length of data in bytes
PIC	0x0C	Pipeline Counter

Table C.10: Event identification buffer

subbranch (see Fig. 3.11). The **SiPPCMask** shows the bit pattern of active RIO2 boards in the corresponding silicon branch and the **SiRAWM** denotes the bit pattern of the active FADCs.

Event Identification Area

The event identification area (EventInd) contains 16 buffers with the information about processed event (see Tab. C.10). The EventIND buffer address in the internal RIO2 memory is $0x10n0$, where n stands for buffer number.

C.2.2 Data Blocks

Raw Data

The space of **Raw data** is divided into 16 buffers, every 32 kByte long. The base address of the buffer number n is

$$RawAdd_n = SiRawDataBase + n \times 0x8\ 000 \quad (C.1)$$

Every **Raw data buffer** contains digitised amplitudes from PMC divided to blocks split accordingly to the FADC number. The address of the raw data buffer corresponding to the particular FADC then writes

$$RawAdd_{n,FADC} = RawAdd_n + FADC \times 0x1\ 000 \quad (C.2)$$

The digitised amplitudes are stored sequentially as lower 12 bits of 16 bit words. The values of L2Keep counter (**L2Keep**) and pipeline counter (**PIC**) are stored at the end of raw data buffer. L2Keep counter denotes the number of L2 keep trigger signals received from the start of the run. It should correspond to the event number.

C.2.3 Hit Data

The space of the **Hit data** is reserved in the same way as for the **Raw data**. Segmentation into 16 buffers and the length of the buffer remain the same. Base address of the buffer number n is given by the following relation

$$HitAdd_n = SiHitDataBase + n \times 0x8\,000 \quad (C.3)$$

Format of the hit data differs according to the **SiMode**.

C.3 PMC

The basic functionality of the PMC was outlined in section 3.5.1, in this section the memory map and treatment of the registers will be described.

C.3.1 Memory Map

The base address of the PMC memory for internal RIO memory addressing is 0xC200 0000. The PMC memory is divided into 2 data buffers and control registers (see Tab. C.11). While one data buffer is filled by the digitised amplitudes the other data buffer is emptied by the FIFO according to the FIFO register content which must have one of the raw data buffer addresses.

The control registers serve for setting, monitoring and testing of the PMC. The **Control Register 1** serves for reset of the PMC board (see Tab. C.12) whereas the **Control Register 2** can be used for monitoring and test purposes (see Tab. C.13). The delivered trigger signals and data transfer state of the PMC can be monitored in the **Status Register 1** (see Tab. C.14).

Register	Address	Description
Buffer 0		
RAM0	0x0000 0000	Data buffer 0
PIC_0	0x0000 7FF8	Pipeline counter buffer 0
L2K_0	0x0000 7FFC	L2Keep counter buffer 0
Control registers		
PICCtr	0x0000 8000	Pipeline counter number
L2KCtr	0x0000 8004	L2Keep counter
StatReg1	0x0000 8008	Status register 1
StatReg2	0x0000 800C	Status register 2
Ctrl1	0x0000 8010	Control Register 1
Ctrl2	0x0000 8014	Control Register 2
FIFO	0x0000 8018	FIFO Destination Address
FIFO_Base	0x0000 801C	FIFO Base Address
...		
Buffer 1		
RAM1	0x0001 0000	Data buffer 1
PIC_1	0x0001 7FF8	Pipeline counter buffer 1
L2K_1	0x0001 7FFC	L2Keep counter buffer 1

Table C.11: PMC memory map

Bit Mask	Name	Description
0x01	L2K_RST	L2 Keep Counter Reset
0x02	FIFO_Flush	Flush the FIFO
0x04	DMA_REQ	Request the DMA
0x08	BUFF_SWAP	Swap the buffers
0x10	RESET	PMC Reset

Table C.12: PMC Control Register 1 bits.

Bit Mask	Name	Description
0x0000 0001	FCLR_TEST	Fast Clear Test
0x0000 0002	PE_TEST	Pipeline Enable Test
0x0000 0004	L2K_TEST	L2 Keep Test
0x0000 0008	L3R_TEST	L3 Reject Test
0x0000 0010	L3K_TEST	L3 Keep Test
0x0000 0020	LINT_INHIB	
0x0000 0040	SEQDMA_INHIB	
0x0000 0080	FCLR_INHIB	
0x001F FF00	L2KCTR	L2 Keep counter
0x0300 0000	DELAY_PARAM	Delay Parameter
0x0800 0000	WAIT_MODE	Wait Mode
0x1000 0000	TEST_MODE	Test Mode
0x2000 0000	PMC_ENABLE	Enable PMC
0x3B00 0000	PMC_NONVOL	

Table C.13: PMC Control Register 2 bits.

Bit Mask	Name	Description
0x0000 0001	CTT_STAT	Clear to transfer
0x0000 0002	FER_STAT	Front End Ready Status
0x0000 007C	PIC_VAL	Pipeline Counter Value
0x0000 0080	L3R_STAT	L3 Reject Status
0x0000 0100	L3K_STAT	L3 Keep Status
0x0000 0200	L2K_STAT	L2 Keep Status
0x0000 0400	PE_STAT	Pipeline Enable Status
0x0000 0800	FIFO_FULL	FIFO Register Full
0x0000 1000	FIFO_EMPTY	FIFO Register Empty
0x0000 2000	DMA_ACTIVE	DMA Transfer Active
0x0007 0000	STATE	State Machine

Table C.14: PMC Status Register 1 bits.

Bibliography

- [1] G. Altarelli and G. Parisi, Nucl. Phys. **B126** (1977) 298;
Y. L. Dokshitzer, Sov. Phys. JETP **46** (1977) 641.
- [2] E.A. Kuraev, N.L. Lipatov and V.S. Fadin, Sov. Phys. JETP **45**, (1977) 199;
Y.Y. Balitski and N.L. Lipatov, Sov. J. Phys. **28**, (1978) 822.
- [3] M. Ciafaloni, Nucl. Phys. **B296**, (1988) 49;
S. Catani, F. Fiorani and G. Marchesini, Phys. Lett. **B234**, (1990) 339.
- [4] S. Frixione, M.L. Mangano, Heavy-Quark Production, Adv. Ser. Direct. High Energy Phys. **15** (1998) 609, hep-ph/9702287.
- [5] J.D. Bjorken, Properties of Hadron Distribution in Reactions Containing Very Heavy Quarks, Phys. Rev. **D17** (1978) 171; M. Suzuki, Fragmentation of Hadrons from Heavy Quark Partons, Phys. Lett. **B71** (1977) 139.
- [6] C.Peterson et al., Scaling violations e^+e^- annihilation spectra, Phys. Rev. **D27** (1982).
- [7] H1 Collaboration, Measurement of $D^{*\pm}$ Meson Production and F_2^c in Deep-Inelastic scattering at HERA, Phys. Lett. **B528** (2002) 199.
- [8] H1 Collaboration, Inclusive Production of D^+ , D^0 , D_s^+ and D_+^* Mesons in Deep Inelastic Scattering at HERA, Eur. Phys. J. **C38** (2005) 447.

- [9] H1 Collaboration, Measurement of D^* Meson Cross Sections at HERA and Determination of the Gluon DENSITY in the Proton using NLO QCD, Nucl. Phys. **B545** (1999) 21
- [10] Zeus Collaboration, Measurement of $D^{*\pm}$ production and the charm contribution to F_2 in deep inelastic scattering at HERA, Eur. Phys. J. **C12** (2000) 35.
- [11] B. W. Harris and K. Smith, Charm quark and $D^{*\pm}$ cross sections in deeply inelastic scattering at HERA, Phys. Rev. **D57** (1998).
- [12] H.L. Lai et. al, Global QCD analysis of parton structure of the nucleon: CTEQ5 parton distributions, Eur. Phys. J. **C12** (2000) 375.
- [13] I. Abt et al., The tracking, calorimeter and muon detectors of the H1 experiment at HERA, Nucl. Instr. and Meth. **A386** (1997) 348.
- [14] I. Abt et al., The H1 Detector at HERA, Internal Report DESY H1-96-01, Hamburg (1996).
- [15] H1 for HERA II, <https://h1-test.desy.de/idet/upgrade/>
- [16] B. List, The H1 Central Silicon Tracker, NIM **A501** (2001) 49-53.
- [17] M. Cuje et al., H1 High Luminosity Upgrade 2000 CIP and Level 1 vertex Trigger, H1 internal report H1-IN-535 (01/1998).
- [18] H1 Calorimeter group, B. Andrieu et al., NIM **A344** (1993) 460.
- [19] H1 SPACAL Group, R.-D. Appuhn et al., NIM **A386** (1997) 397.
- [20] H1 SPACAL Group, T. Nicholls et al., NIM **A374** (1996) 149.
- [21] H. Cronström et. al, The H1 Forward muon spectrometer, NIM **A340** (1994).
- [22] M. Nožička, The forward and backward silicon trackers of H1, NIM **A501** (2003) 54.
- [23] W.R.Leo, Techniques for Nuclear and Particle Physics Experiments, Springer-Verlag Berlin 1987.

-
- [24] M. Nožička, Silicon Detector for deep inelastic scattering of electrons on protons in H1 experiment, Diploma thesis, Charles University in Prague.
- [25] S. Eidelman et al, Review of Particle Physics, Phys. Lett. **B592** (2004) 1.
- [26] H. Jung, The RAPGAP Monte Carlo for Deep Inelastic Scattering, <http://www.desy.de/jung/rapgap/>
- [27] G. J. Feldman et al., Observation of the Decay $D^{*+} \rightarrow D^0\pi^+$, Phys. Rev. Lett. **38** (1977) 1313.
- [28] IP-Unidig-I, User's Manual.
- [29] VIPC616, User's Manual.
- [30] VIPC618, User Manual.
- [31] RIO2 8062, PowerPC based RISC I/O Board, User's Manual, CES.
- [32] PowerPC 603e and EM603e, RISC Microprocessor family, User's Manual.
- [33] W.J. Haynes, VMEtaxi Mark-2 System Software Package, nonpublished
- [34] U. Bassler and G. Bernardi, On the Kinematic Reconstruction of Deep Inelastic Scattering at HERA: the Σ Method, hep-ex/9412004.
- [35] U. Bassler and G. Bernardi, Structure Function Measurements and Kinematic Reconstruction at HERA, hep-ex/9801017.
- [36] J. Chýla, Quarks, partons and Quantum Chromodynamics, Lecture notes <http://www-hep.fzu.cz/Theory/notes/text.ps.gz>
- [37] Z.Rúriková, Measurement of charm fragmentation in DIS at HERA, Phd. Thesis, University Hamburg.
- [38] Markus Kausch, The Silicon Microvertex Detector of the H1 Experiment: Readout, Event Reconstruction and Studies on Heavy Quark Decays, Phd. Thesis, University Hamburg.
- [39] U. Schneekloth, The HERA Luminosity Upgrade, nonpublished DESY library.

- [40] Labview – Graphical Programming Environment, National Instruments
- [41] J.Bürger et al., Online readout and control unit for high-speed/high resolution readout of silicon tracking detectors, Nucl.Instr. and Meth. **A386** (1997) 269-279.
- [42] A Forward Silicon Tracker for H1, W. Braunschweig et. al., H1 internal note H1-02/99 563.

Acknowledgement

I would like to express my gratitude to Josef Žáček, the supervisor of this dissertation, for his stimulating interest in the preparation of the thesis especially for reading first drafts and his comments on the structure of the text. He helped me together with Petr Reimer, Institute of Physics, AVČR, to correct the embarrassment in the thesis text.

I would like to thank to Peter Kostka, the leader of the H1 Zeuthen group, for his steady interest in my work and his cooperation on the project. He helped me in many ways in my work and supported any ideas which could result in better understanding, functionality and stability of the silicon trackers.

My gratitude belongs to my colleagues Ivan Glushkov and Sergey Gorbounov. I had many discussions with them about the analysis of the Forward Silicon Tracker data. Their comments and questions put some light into the problematics of the track reconstruction.

I am indebted to other people of the H1 group who cooperated on the upgrade of the silicon trackers, namely Bill Haynes, Eberhard Wunsch, Milan Janata, Wolfgang Lange, Hans Henschel and many others.

My visits in DESY–Hamburg and DESY–Zeuthen were supported by the Ministry of Education of the Czech Republic under the projects LA116/2000, 1P05LA259, LN00A006 and LC527.

Last but not least I thank to my beloved wife who stood by me during the time I was writing this thesis. I admire her patience and understanding with the physicist who is too deeply involved in the problems she does not understand.